

SPECTROSCOPIC INVESTIGATIONS IN THE ORION NEBULA

by

Kevin Blagrove

A thesis submitted in conformity with the requirements
for the degree of Doctor of Philosophy
Graduate Department of Astronomy and Astrophysics
University of Toronto

Copyright © 2006 by Kevin Blagrove

Abstract

Spectroscopic Investigations in the Orion Nebula

Kevin Blagrove

Doctor of Philosophy

Graduate Department of Astronomy and Astrophysics

University of Toronto

2006

We are engaged in a comprehensive program to find reliable elemental abundances in and to probe the physical structure of the Orion Nebula, the brightest and best-resolved H II region. This thesis assists in the fulfillment of this goal by analysing, in detail, deep echelle spectra and HST spectra (FOS, STIS) of various lines of sight in the nebula.

All observed fluxes are affected by extinction, mostly from the foreground “veil”, and so it is essential that they be corrected accurately before further analysis and interpretation. An analytic expression for the wavelength dependence of the extinction is developed which when normalized for a given line of sight provides a solid basis for the extinction correction from the ultraviolet through to the infrared.

Applying our new analytic extinction correction to ground- and space-based spectral observations, we are able to confirm – for the first time – a number of the theoretically-expected deviations from He I case B recombination theory. Furthermore, we show that CLOUDY models that include radiative transfer effects provide a remarkable quantitative agreement between theory and observation.

Ionic abundances can be derived from permitted and forbidden lines with knowledge of the dominant line formation mechanism. However, for a given ion, the derived abundances are not consistent. Temperature fluctuations within the nebula have been invoked to reconcile these differences. From temperature measurements using long-slit STIS spectra we find that actual temperature fluctuations in the plane of the sky are minimal.

The nebula is home to a number of velocity systems, both within the nebula’s primary ionization front and elsewhere. Our high-resolution ground-based echelle spectra allow for the isolation of many of these velocity systems, including the distinctive velocity-shifted spectrum

associated with a Herbig-Haro object, HH 529. By modeling its emission lines, we determine a gas-phase abundance of Fe that is consistent with the depleted (relative to solar) abundance found in the Orion Nebula – evidence for the presence of dust. We also exploit the nebular velocity structure to show that it is necessary to modify the ground configuration energy levels of O^+ . Using planetary nebulae and our Orion Nebula observations of the $[O\ II]$ forbidden lines, we publish new laboratory wavelengths for these same lines.

Acknowledgements

The completion of a thesis is no small task, and certainly not one that can be completed alone. There have been many people who have supported me in ways both academic and personal over the course of my graduate career. I will mention some here, but all have provided a wonderful support structure. Thank you.

Specifically, I would like to thank my Ph.D. supervisor, Peter Martin, for his support – be it through informal discussion, constructive commentary, or informed advisement. Even while away for extended periods (on sabbatical and/or at a conference and/or at a meeting), Peter has always made himself available. Thank you.

I would also like to thank Norm Murray and John Lester for their support throughout the Ph.D. program, and Ernie Seaquist and Marshall McCall for their constructive criticism of this document. I acknowledge fruitful scientific collaboration with Jack Baldwin, who has assisted with the reduction of the CTIO echelle spectra, and Bob Rubin, who has assisted with all things HST-based. And to Marc Goodman and the department administrative staff, who have always been attentive to the graduate student needs, thank you.

My time spent at the University of Toronto has also been rewarding thanks to the many people I have met in the department, in the Hart House Chorus and at Massey College. These friendships have meant a lot to me and have made my time here productive and rewarding, both scientifically and socially. Thank you, all.

Finally, I would like to acknowledge my family – my parents, David and Mary Anne, and my sisters, Sarah, Vanessa and Catherine – for having helped and supported me throughout these many years of post-secondary and post-graduate education. Thank you.

This work has been funded by the Natural Sciences and Engineering Research Council of Canada, the Ontario government, the Walter C. Sumner Foundation, and the University of Toronto.

Contents

1	Introduction	1
1.1	Background	1
1.1.1	The nature of the nebula.	1
1.1.2	... and small-scale variation	2
1.2	Thesis layout	6
2	Data reduction	8
2.1	CTIO echelle spectra	8
2.2	HST STIS spectra	10
3	Extinction corrections	13
3.1	Parameterization of extinction	14
3.1.1	Determining the shape, s_λ : Stellar extinction	15
3.1.2	Setting the amplitude, a : Optimal fitting of emission lines	17
3.2	Comparison between stellar and nebular extinction curves	18
3.2.1	Infrared discrepancy	18
3.2.2	Ultraviolet	20
3.3	The stellar extinction curve: validation	21
3.3.1	Optical	21
3.3.2	Ultraviolet	23
3.3.3	Near infrared	24
4	He I decrements and more on extinction corrections	25
4.1	Observations	25
4.2	Anomalous He I decrements	27
4.2.1	Extinction-corrected data	27
4.2.2	Case B	32
4.2.3	Anomalous decrements	33

4.2.4	Photoionization models	34
4.2.5	Comparison with observations	38
4.2.6	Extinction corrections revisited	40
4.2.7	He ⁺ /H ⁺ ratio	45
4.3	Summary	45
5	O II ground configuration energy levels	47
5.1	Bowen revisited	49
5.2	Observations of the Orion Nebula	53
5.3	Constraining the energy levels with the Orion Nebula data	55
5.4	Comparison to recent work of Sharpee et al.	61
5.5	Conclusions	62
6	Temperature variations from HST spectroscopy	63
6.1	Extinction and reddening correction	65
6.2	Electron temperature determination	66
6.2.1	[O III] electron temperature	66
6.2.2	[N II] electron temperature	69
6.3	Fractional mean-square temperature variations	72
6.4	Error analysis	76
6.4.1	Method 1 – Continuum approximation	77
6.4.2	Method 2 – Line profile	77
6.4.3	Method 3 – Multiple measurements	79
6.5	Discussion and conclusions	80
7	A photoionized Herbig-Haro object in the Orion Nebula	83
7.1	Observations	84
7.1.1	Blue/red line strengths	104
7.1.2	Reddening	104
7.2	Analysis	106
7.2.1	Velocity	106
7.2.2	Temperature and density	106
7.2.3	Relative line strengths and ionization structure	110
7.2.4	Temperature fluctuations	111
7.3	Revisiting [Fe III] energy levels	113
7.4	Models	115
7.5	Discussion	117

7.5.1	Depletion	119
7.5.2	Temperature fluctuations	125
7.6	Conclusions	126
8	Summary and future directions	128
	Bibliography	131
A	CLOUDY contributions	140

List of Tables

3.1	Observed ratios of common-upper-level lines, I_{2471}/I_{7325} , and predictions from theory	24
4.1	HST STIS V2 and FOS observations prior to reddening correction ($I_{\lambda}/I_{H\beta}$) . . .	28
4.2	He I relative intensities, I_{λ}/I_{4471} , after correcting for reddening using H I Balmer (and Paschen) lines and our extinction curve	30
4.3	CLOUDY input parameters for models M and K	37
4.4	Model abundances relative to H ($12+\log(X/H)$)	38
4.5	Constraints on model parameters	39
4.6	Dereddened HST STIS V2 and FOS observations ($I_{\lambda}/I_{H\beta,predicted}$)	42
5.1	O II ground configuration energy levels (cm^{-1})	47
5.2	Determination of ${}^2D_{5/2}$ energy from planetary nebulae data	51
5.3	Best-fit line parameters for visible wavelength transitions	53
5.4	Comparison between observed and predicted line ratios as determined from transition probabilities, A_{ij}	56
5.5	Line velocities in Orion using recent wavelength tabulations	57
6.1	Values of $T_{0,A}$ and t_A^2 for STIS slits	75
6.2	Weak line uncertainties and the associated fractional mean-square temperature variation, t_e^2	78
7.1	Summary of double Gaussian fits to observed echelle spectra	92
7.2	Blue/red echelle spectra comparison.	105
7.3	Physical conditions within the nebula and the shock	108
7.4	O ⁺⁺ /H ⁺ ratios from permitted lines	113
7.5	O/H from collisionally excited lines and recombination lines with a derived t^2 parameter	114
7.6	Constraints on model parameters for models A and B	117

7.7	CLOUDY input parameters	118
7.8	Model abundances relative to H ($12+\log(X/H)$)	118
7.9	Comparison of model predictions and observations.	120
7.10	Iron abundance and depletion in the Orion Nebula and HH shock	123

List of Figures

1.1	Costero & Peimbert (1970) extinction law	4
1.2	Sketch of Orion Nebula showing Herbig-Haro flows and microjets	5
2.1	Position of four STIS slits and two CTIO slits overlaid on WFPC2 image	9
3.1	UV and IR modifications made to CCM89 formulation	16
3.2	Extension of the CP70 curve into the UV and the renormalized CP70 curve	19
3.3	Our analytic extinction curve and CP70 curve as determined from EPG04 observed data	22
4.1	STIS Slits 1 and 2 and FOS 1SW and x2 positions	26
4.2	Grotrian diagram of He I singlet and triplet lines	29
4.3	Variation in He I lines as a function of $\tau_0(\lambda 3889)$ for different amounts of turbulence	36
4.4	Variation of He I lines as a function of v_{turb} in the full nebular model	37
4.5	Observed He I decrements compared to case B and CLOUDY model predictions for four series	41
4.6	Differential extinction curve for FOS-1SW	43
4.7	Differential extinction curve for STIS-SLIT1c	44
5.1	Grotrian diagram of O II ground configuration energy level transitions	48
5.2	Gaussian profile fit of three of the six visible O II lines (1SW)	54
5.3	Gas velocity as a function of the emitting species' ionization potential	59
6.1	T_e from [O III] and [N II] for STIS Slits 1 and 2	68
6.2	T_e from [O III] and [N II] for STIS Slits 4 and 5	70
7.1	Red x2 echelle slit position	86
7.2	Flux variation of the He I $\lambda 5876$ spatially-narrow velocity-bridge component	87
7.3	H α region comparison between ground-based echelle spectroscopy and WFPC2 photometry	89

7.4	Variation of the [O III] $\lambda 5007$ and [O II] $\lambda 3726$ velocity-shifted shock component line flux across the echelle slit	90
7.5	Double Gaussian fit of the nebular and velocity-shifted shock components	91
7.6	Measured velocity of shock component from unconstrained double Gaussian fit .	107
7.7	Shock-to-nebula line ratios as a function of the ionization potential	112
7.8	Ionization fraction of Fe as a function of depth from the x2shock model and from the nebular model	124

Chapter 1

Introduction

1.1 Background

The Orion Nebula is a near-ideal candidate with which to study H II regions because of its high surface brightness and its proximity (~ 450 pc). However, despite these advantages, the nature of the nebula and its small-scale variation are still not completely understood. Using observed and modeled emission lines, the research presented here will contribute to a better understanding of both the nature of the nebula (extinction) and its small-scale variations (a photoionized Herbig-Haro object and temperature fluctuations). En route to our conclusions, the validity of some atomic data – both theoretical wavelengths and transition probabilities – has been brought into question and, where possible, has been improved upon.

1.1.1 The nature of the nebula...

A physical model of the Orion Nebula is needed in order to interpret emission line spectra and ultimately to derive reliable abundances. These models have developed over time from a spherical model (Sharpless, 1952) to the present day blister model (e.g., Zuckerman, 1973) with a champagne flow (Tenorio-Tagle, 1979). The geometry is such that the Orion Nebula resides on the surface of a molecular cloud (Orion Molecular Cloud); this cloud lies further from the observer than the ionizing star, Ori θ^1 C in the Trapezium, but is in close proximity (~ 0.25 pc, Wen & O’Dell, 1995; O’Dell, 2001a) to it. This proximity leads to the observed high surface brightness of the nebula. Gas from the molecular cloud is ionized and heated by the high-energy (UV) stellar continuum. Overpressured dense hot gas results in the “champagne flow” accelerating away from the background molecular cloud towards the observer (and the ionizing star). Such geometry results in two observable gradients: one in ionization; and one in velocity.

With this information in hand, the nature of the nebula has been probed. Temperature

and density diagnostic lines are coupled with the ionization structure and emission mechanism information to determine abundances of elements. These abundances have been found from individual line ratios directly (e.g., Esteban et al., 2004) and using CLOUDY photoionization equilibrium models (Baldwin et al., 1991). To determine a robust set of abundances, one must use as many emission lines as possible. Since these then tend to span a broad spectral range, a consistent, robust extinction correction over the entire spectral range is required. One extinction correction frequently applied to Orion Nebula data has been that developed by Costero & Peimbert (1970). These authors applied the line intensity measurements of Peimbert & Costero (1969) and the $\lambda 1.95$ cm radio map of Schraml & Mezger (1969) to determine the shape of the extinction curve (characterized here by a unitless parameter, f_λ), as reproduced in our Figure 1.1. Values of f_λ are then tabulated from this (interpolation) curve. To determine the magnitude of the reddening correction for a particular line of sight in the Orion Nebula, the total extinction at $H\beta$, $C_{H\beta}$, must first be calculated from the observed and theoretical Balmer decrement. Following this, the reddening correction at a particular wavelength is calculated from f_λ and $C_{H\beta}$.

In this thesis, we discuss and develop a new more robust method of determining the extinction correction from the infrared through to the ultraviolet. It is extremely important that this reddening is performed correctly to allow for an accurate full spectral comparison of emission lines and abundances – either via individual line ratios, or via CLOUDY models.

1.1.2 ...and small-scale variation

Despite having a good overall picture of the nature of the nebula, there exist many unknowns when it comes to the detailed physics within this (and other) nebula. Whether it be Herbig-Haro objects, or temperature fluctuations, the Orion bar or proplyds, the Orion Nebula is home to a variety of smaller-scale phenomena, whose physics are not entirely known (for a review, see O’Dell, 2001b). In this thesis, we will discuss two of these small-scale phenomena: a photoionized Herbig-Haro object and temperature fluctuations.

Herbig-Haro objects

Herbig-Haro (HH) objects, first discovered by Herbig (1950) and Haro (1952), have more recently been shown to be associated with outflows from stars that are in the early stages of formation (e.g., Dopita et al., 1982). The Orion Molecular Cloud being a home to many of these newborn stars, it is not surprising that the Orion Nebula has a number of observed small-scale features that have been identified as HH objects, some of which actually penetrate the ionized region. In their survey of the Orion Nebula, O’Dell et al. (1997b) have found that two

spatially-separated systems of HH objects exist in the nebula: those in a “North” group with associated H_2 emission are possibly shocks in the photodissociation region (PDR) and those in a “South” group with no associated H_2 emission are thought to be shocks formed in the foreground neutral lid, or “veil”. A larger survey of these objects (and disks, proplyds and windblown bubbles) was completed by Bally et al. (2000), in which a number of proper motions and radial velocities of the HH objects are published. A summary of their findings is reproduced in our Figure 1.2. Following up on this survey, Doi et al. (2002) and Doi et al. (2004) published more detailed tangential and radial velocities, respectively, for an even broader range of HH objects.

At the velocities associated with these HH objects, it is expected that the grains – whose presence usually results in the depletion of the gas-phase abundances of elements like Fe – will be destroyed. Higher gas-phase abundances of Fe are indeed seen in HH objects observed by Beck-Winchatz et al. (1996) and Böhm & Matt (2001). However, unexpectedly, these high gas-phase abundances are seen in both low- and high-excitation HH objects leading to the conclusion that the material currently associated with the low-excitation (and slow-moving) HH object must have passed through a high-excitation (and fast-moving) HH shock at an earlier time (Böhm & Matt, 2001).

Temperature fluctuations

Temperature fluctuations were initially defined/introduced by Peimbert (1967) and have been invoked since then to explain the discrepancy between abundances derived from collisionally-excited lines and abundances from recombination lines. These fluctuations are expected to be fairly small (i.e., a fractional mean-square temperature, $t^2 < 0.01$) according to nebular cooling/heating theory and models (e.g., Kingdon & Ferland, 1998). The temperature fluctuations required to explain the difference in calculated abundances are on the order of $t^2 \sim 0.02 - 0.03$ (Esteban et al., 2004) for the Orion Nebula, and as high as $t^2 \sim 0.1$ (Liu et al., 1995) in a planetary nebula, NGC7009. Such large fluctuations would require an additional, and, as yet, unknown heating source, capable of heating the nebula by roughly 10^3 K. Some alternative ideas have been developed to explain these fluctuations (e.g., shadowed regions behind high-density clumps, O’Dell et al., 2003), but to date none of these has been demonstrated theoretically to explain the large magnitude of t^2 . Regardless of the cause of these temperature fluctuations, O’Dell et al. (2003) also suggest that an unexplained extra “turbulent” line broadening (which also appears to have a temperature dependence) seen in Orion Nebula emission lines may be linked with the source of t^2 .

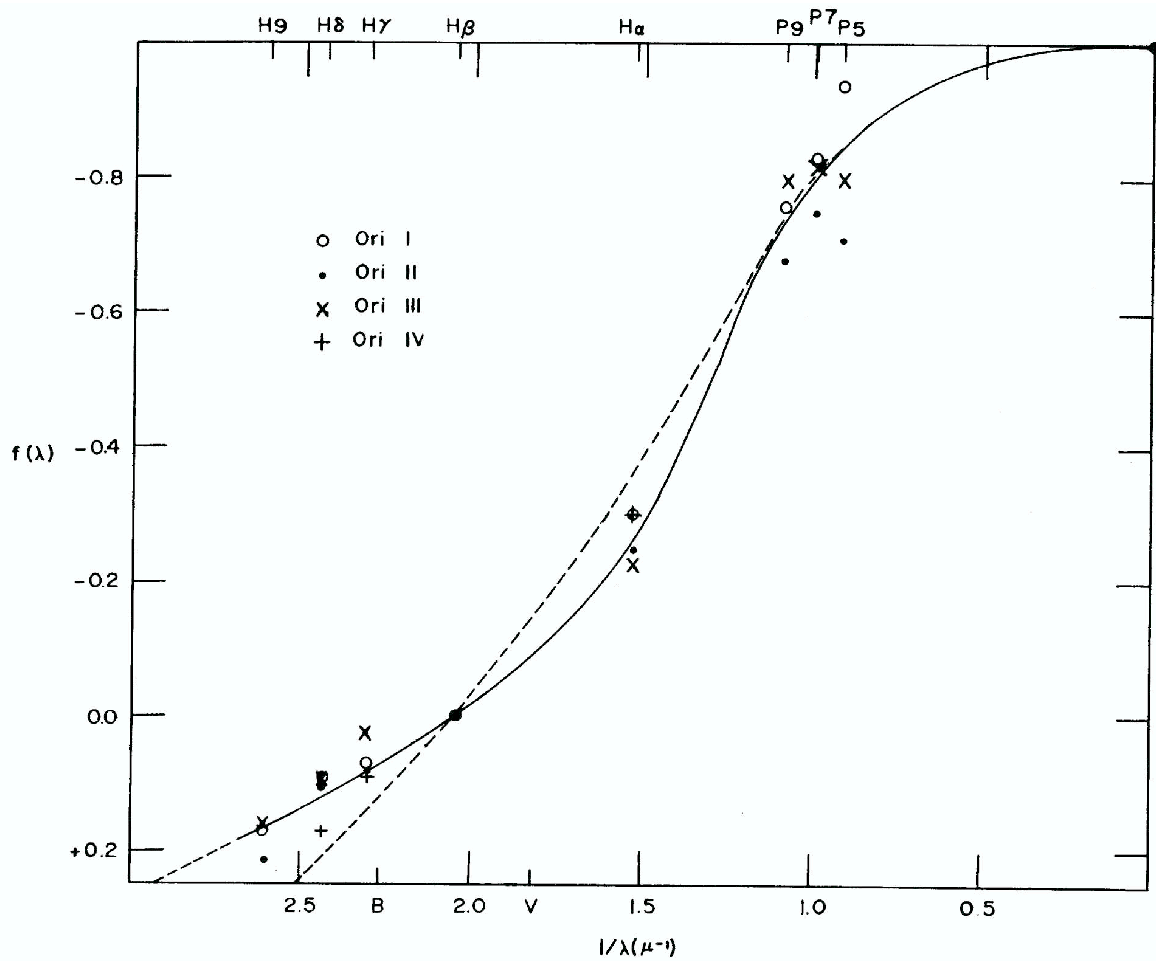


Figure 1.1 The average nebular extinction (solid line) as determined by Costero & Peimbert (1970) from four observed regions (Ori I-IV), and as represented by the unitless parameter f_λ ($[f_\lambda + 1] \propto A_\lambda/A_V$). The dashed line is the normal stellar extinction law (Seaton, 1960). Figure reproduced from Costero & Peimbert (1970).

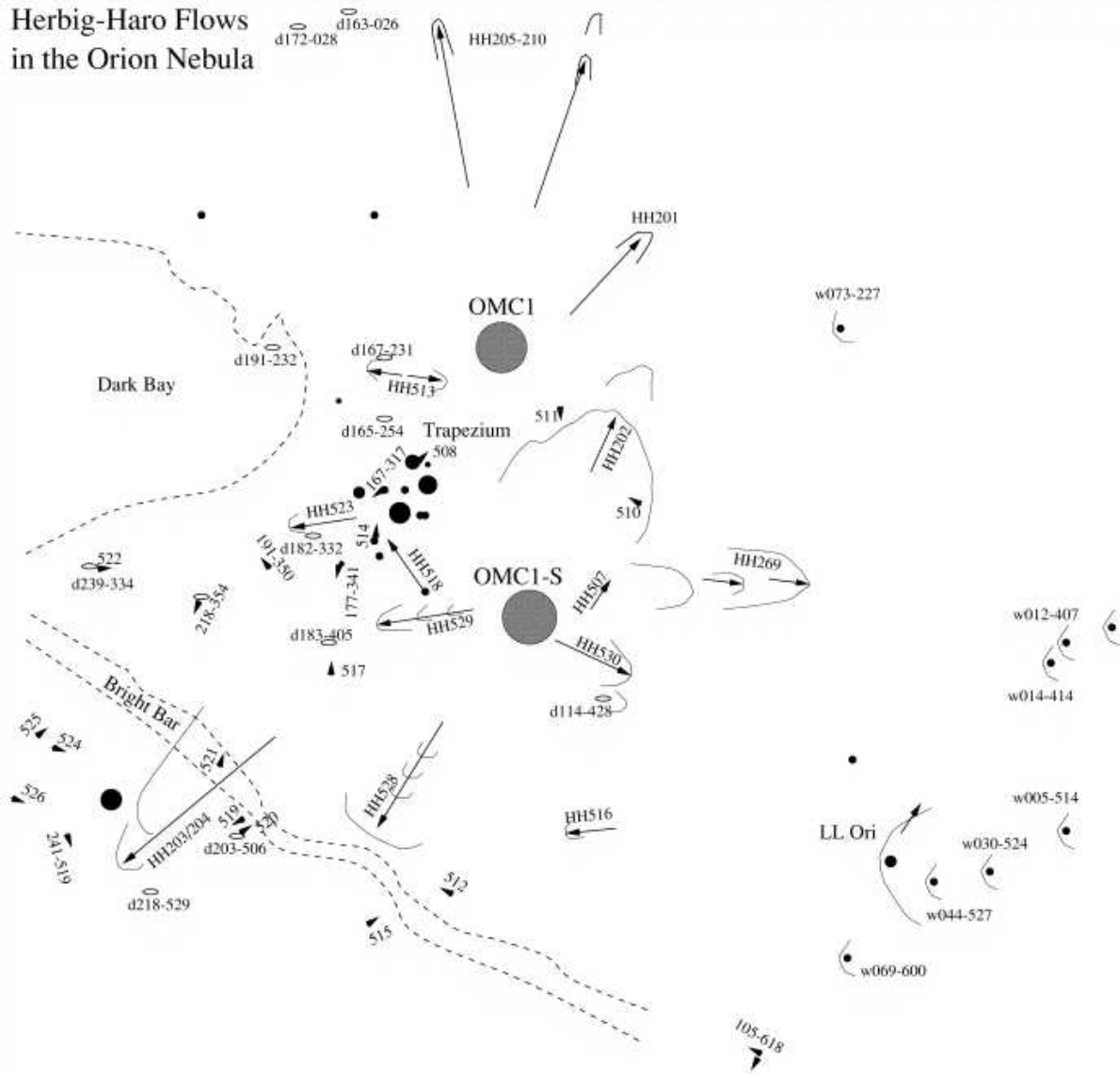


Figure 1.2 Sketch of the Orion Nebula (roughly $6' \times 6'$) showing Herbig-Haro (HH) flows with vectors indicating the flow direction. Other symbols represent microjets (arrowheads), LL Ori bow shocks (black circles surrounded by bow-shaped icons) and silhouette disks (small ellipses). N is up and E to the left. Reproduced from Bally et al. (2000) by permission of the AAS.

1.2 Thesis layout

This thesis develops and discusses an on-going project to determine a complete robust set of Orion Nebula abundances using both ground-based and HST spectra with a broad spectral coverage from the ultraviolet through to the visible (Baldwin et al., 1996; Rubin et al., 1997; Baldwin et al., 2000).

Two properties of our spectra figure prominently in this thesis: the intensities and the line velocities. The intensities are integral to determining models of the nebula and its key features, whereas the velocities can provide additional key information about where and how lines form. The observations and data reduction process are discussed in Chapter 2.

In order to determine intensities accurately over the wide spectral region covered, a new analysis of the extinction correction over the range from ultraviolet to infrared must be performed. This extinction correction is developed in Chapter 3. Following this correction, the intensities have been used to examine a suite of He I recombination lines including those in the infrared and ultraviolet portions of the spectrum. This is of interest because predictions exist as to how the population of the metastable 2^3S state will affect the $2^3S - n^3P$ and related series of lines. There has not yet been a direct comparison with observation, especially for large values of n . This comparison is made in Chapter 4.

A velocity gradient exists in the Orion Nebula, as the high-density, overpressured gas of the background molecular cloud accelerates into the low-density intercloud medium. The geometry of the Orion Nebula is such that the more highly ionized material (i.e., that material which is closer to the ionizing star and thus the observer) is moving with a larger velocity. The line velocity that we observe indicates from which ionization region the line originates. Moreover, emission lines originating from (transitions within) a common ion are expected to have the same velocity. Therefore, from accurate observed line wavelengths, conclusions can be drawn about the underlying theoretical wavelengths from which these velocities are obtained. A set of new theoretical wavelengths is determined for both O II (Chapter 5) and Fe III (Chapter 7), using velocities of nebular and HH shock lines.

The HST STIS spectra offer some unique information about the spatial variation of the nebular line emission, including a measurement of the temperature variation, t^2 , in the plane of the sky. This is discussed in Chapter 6.

A novel analysis of a Herbig Haro shock in the Orion Nebula is given in Chapter 7. This Herbig Haro object is determined to be photoionized and is modeled as such. From this model follows a discussion of the depletion of elements often associated with grains, and a brief follow-up to the temperature fluctuations discussion of Chapter 6.

In the Appendix, we briefly present some of the contributions made to CLOUDY during

the development of this thesis. These include identifying a number of significant bugs/typos and the development of a higher resolution Fe^{++} atomic model.

The following chapters have been accepted for publication: Chapters 3 and 4 accepted for publication jointly as Blagrove et al. (2006c) (©2006 The American Astronomical Society), and the following chapters have been published: Chapter 5 as Blagrove & Martin (2004) (©2004. The American Astronomical Society), Chapter 6 as Rubin et al. (2003) (©2003. Royal Astronomical Society), and Chapter 7 as Blagrove et al. (2006a) (©2006. The American Astronomical Society).

Chapter 2

Data reduction

2.1 CTIO echelle spectra

Spectra were obtained using the echelle spectrograph and a $13''.1 \times 1''$ slit on the 4 m Blanco telescope at the Cerro Tololo Inter-American Observatory (CTIO; see Baldwin et al., 2000, for details), covering the spectral range from the near-UV to the near-IR. Three sets of red (5100-7485 Å) and blue (3510-5940 Å) spectra were obtained on two dates in 1997 and 1998, respectively. The observed lines of sight are referred to as 37W (after Baldwin et al., 1991, i.e., $37''$ W of θ^1 Ori C), 1SW and x2 (labelled as such in Baldwin et al., 1996; Rubin et al., 1997). The approximate positions of slits 1SW and x2 are shown in Figure 2.1, overlaid on a composite WFPC2 image. The 37W data have been previously published by Baldwin et al. (2000), the 1SW data are referred to in Chapter 5 and will be published as Blagrove et al. (2006b), and the x2 data are presented in Chapter 7, along with a discussion of the exact x2 slit position.

To collect deep echelle spectra without losing the strong emission lines to saturation, exposures of varying lengths were collected. In the red, two 1000 s exposures and two shorter exposures of 10 s and 100 s were taken of 1SW, and one 1000 s and one 100 s of x2. In the blue, three 1000 s exposures and two 100 s exposures were taken of 1SW, and three 1000 s and two 100 s of x2.

The spectra were reduced using the IRAF echelle package, extracting only the central $10''$ of the slit. The flux calibration was performed using spectra of the standard stars η Hya, θ Crt and 108 Vir as discussed in Baldwin et al. (2000). Following this calibration, the 1000 s long-exposure spectra were combined (using the IRAF routine *imcombine*) in order to remove cosmic rays. The blue spectra required further reduction as the appearance of Rowland ghosts surrounding strong emission lines might interfere with the line measurements (and could possibly lead to erroneous line identifications). These features are a result of reflections in the blue echelle grating used in the spectrograph. An algorithm is applied to the blue spectra in order to

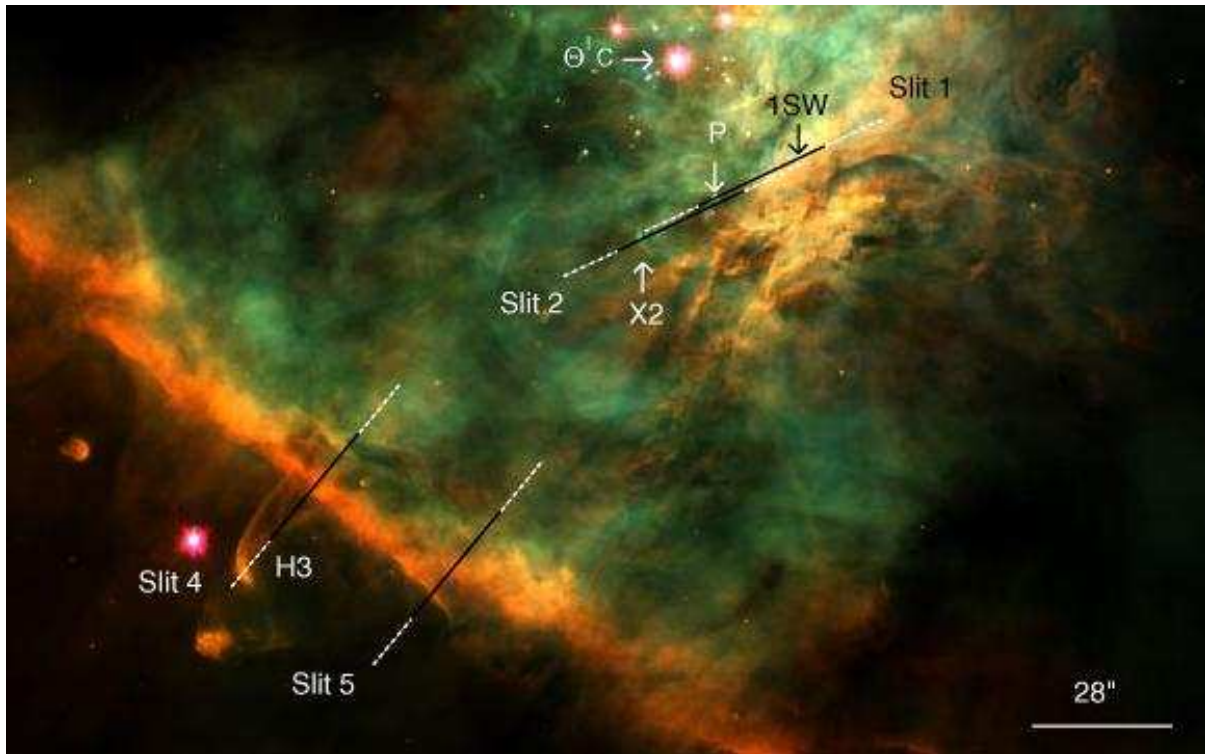


Figure 2.1 This shows the position of the four STIS slits and the rough location of the two CTIO slits overlaid on a composite WFPC2 image with [O III] ($\lambda 5007$) blue, H α green, and [N II] ($\lambda 6583$) red. The STIS-CCD observations presented here are taken with the long-slit $52'' \times 0''.5$. The middle portion of each slit, shown in black, represents the smaller length ($28''$) for which we have obtained observations using the MAMA detectors. The CTIO $13''.1 \times 1''$ slits are centred on the points labelled 1SW and x2 and are oriented roughly parallel to the STIS slits. Refer to Figure 7.1 for the exact x2 slit position. Abbreviated labels stand for positions described in Chapter 6: P for the proplyd P159-350; H3 for HH 203. Note that the star θ^2 Ori A is the unlabelled red feature just above the 4 in Slit 4. North is up and East to the left.

eliminate these ghosts from the spectra (Baldwin et al., 2000). The flux-calibrated long (1000 s) and short (100 s) exposures were compared to determine if any lines were saturated in the long exposure. The two lines $\lambda 5007$ and $\lambda 6563$ appeared to be, so these lines are always measured from the short-exposure spectra.

Since the red and blue spectra were obtained at different times of the year, a wavelength alignment between these two sets of spectra was required, in order to account for the Earth’s orbital motion (predicted to be a 10.9 km s^{-1} effect). This was done by aligning emission lines found in both spectra. For x2 the wavelength re-alignment is equivalent to a shift of $10.0 \pm 0.8 \text{ km s}^{-1}$ and for 1SW the re-alignment is $6.2 \pm 1.3 \text{ km s}^{-1}$. This latter value is inconsistent with what is predicted, most likely due to a shift in the relative positioning of the spectrograph and wavelength calibration equipment (i.e., a literal “clunk” in the system; J. A. Baldwin, private communication) during the observation run in 1998. The red spectra have been adjusted to the frame of the blue in both cases, so this anomalous shift is effectively erased. (There was no detectable wavelength dependence when comparing the red and blue 1SW lines, eliminating any worry about a relative wavelength calibration problem.)

To extract the information on individual lines, the data were modeled with a Gaussian (three parameters: central wavelength, FWHM, and area) and a linear baseline (two further parameters: continuum offset and slope). This model also provides 1σ errors for each of its parameters. The parameters of interest here (see Chapters 5 and 7) are primarily the central wavelength and the area. The area and the 1σ uncertainty which the model provides supplies a good estimate of each line’s signal-to-noise ratio. The central wavelength can provide a measure of each line’s relative velocity. For consistency with other observations of the Orion Nebula (e.g., Baldwin et al., 2000), these wavelengths were shifted to the rest-frame velocity of the H^+ gas using the velocities of the six strongest unblended H I Balmer lines. This wavelength reference frame is preferred to that used by others (e.g., Esteban et al., 2004), where they quote all observed wavelengths in the heliocentric frame ($v_{\odot}(\text{H}^+) \sim 12 - 14 \text{ km s}^{-1}$), a seemingly arbitrary velocity system for the gas in the Orion Nebula.

2.2 HST STIS spectra

The STIS data were taken as part of the HST Cycle 7 program GO-7514. We observed with 4 different STIS long-slits, labelled: Slits 1, 2, 4, and 5. These are shown in Figure 2.1. The slit positions were chosen to cross several features, including the Herbig-Haro (HH) object HH 529, a proplyd, and the Orion Bar. Slit 1 passes through the position 1SW which was observed with FOS and GHRS in Cycle 5 (see Figure 1 in Rubin et al., 1997) and from the ground (Blagrove et al., 2006b). The centre of 1SW is at $\alpha, \delta = 5^{\text{h}}35^{\text{m}}14^{\text{s}}.71, -5^{\circ}23'41''.5$ (all positions are equinox

J2000), 18.5" S and 26.2" W of θ^1 Ori C. This slit was also chosen to pass through proplyd P159-350 (O'Dell & Wen, 1994). Slit 2 passes through position x2 (HH 529) observed with FOS in Cycle 5 (see Figure 1 in Rubin et al., 1997) and from the ground (Chapter 7). The position angle (PA) = 114.555°; the distance between slit centres is 18.1". Note that the bottom of Slit 1 and the top of Slit 2 have a separation of only 0.211". The displacement between these two slits in the direction along the slit is 18.056".

Slit 4 crosses the Orion Bar and is oriented to point toward θ^1 Ori C, which also places it essentially orthogonal to the Bar. The southern tip passes through the Herbig-Haro object HH 203. Slit 5 passes through a very bright, sharply-defined "rim" of the Bar where a positional bifurcation begins. The PA = 139.068°; distance between centres of Slits 4 and 5 is $\sim 32''$.

Observations were made as follows: data for Slits 1 and 2 are from Visit 2 (1998 December 7 UT), Visit 52 (2000 December 7) and Visit 72 (2001 December 16); data for Slits 4 and 5 are from Visit 5 (1998 December 22). The data were acquired using STIS/CCD (all slits, all visits), STIS/FUV-MAMA (Slits 1 and 2, V2) and STIS/NUV-MAMA (Slit 1, V2) with a $52'' \times 0.5''$ slit of which only (the roughly central) $28''$ are recorded using the STIS UV detectors.

Each visit comprises 2 orbits. Spectra were taken with gratings G140M (with wavelength setting: 1665), G230M (settings: 1884, 2176, 2499, 2739, 2977), G430M (settings: 3680, 4451, 4961) and G750M (settings: 5734, 6581, 7283). Each exposure was done in accumulation mode and at least two spectra were taken at each setting in order to cosmic-ray (CR) clean. The data sets we processed were those obtained after sufficient time elapsed from the observation dates in order that "best reference files" would be stable/finalized. We requested On-the-Fly Calibration for science files and Best Reference Files.¹ After retrieving the data sets, we then co-added and cosmic ray cleaned images using standard packages in IRAF. Calibrations to produce 2-dimensional (2D) rectified images were then carried out.

Even after applying the standard CR rejection routine there remain many bad pixels due to CRs and/or hot pixels. There is considerable danger that including these can corrupt the flux values we seek. The interactive program developed to eliminate these remaining bad pixels is called PIXHUNTER, which has been described briefly by Rubin et al. (2002) (see their Appendix A). Once the columns containing the line have been cleaned for deviant pixels, we are ready to subtract an equivalent spectral range of continuum. We do this by using IRAF

¹According to Paul Goudfrooij (private communication), the STIS MAMA and CCD absolute flux calibration that is performed in the pipeline follows methods described in Instrument Science Report (ISR) 97-14 (Bohlin et al., 1998) available through the STIS web site, <http://www.stsci.edu/hst/stis/documents/isrs>. That report considers only the L (low-resolution) modes specifically, but the flux calibration for the M (medium-resolution) modes is done the same way, i.e., by comparing the observed spectrum of a primary standard with a pure-hydrogen white dwarf model. The calibration observations were made with the $52'' \times 2''$ slit; thus relative transmission corrections are necessary to derive the absolute fluxes for the other slits (such as the $52'' \times 0.5''$ slit we used). This procedure is documented in ISR 98-20 (Bohlin & Hartig, 1998).

functions, including *blkavg*, to operate upon the appropriate sections of cleaned continuum.

To increase the signal-to-noise of the lines, we use the IRAF routine *blkavg* to sum the spectra spatially, creating tiles of a specific size. For example, in Chapters 3 and 4 we create four $13'' \times 0''.5$ tiles, and in Chapter 6 – where we are interested in the distribution of line flux along the slit spatial direction – we create $0''.5 \times 0''.5$ tiles.

We note that there is excellent agreement with a cross check of the (untiled, single pixel) 1D results of flux versus spatial direction by comparing with 1D results of flux versus wavelength for a corresponding spatial sample. The latter were measured with the *splot* package. With this, the underlying continuum is fitted and the integrated line flux determined with the *e*-option (area under the line profile), which was preferable to fitting with a Gaussian profile. Because of the spectral impurity introduced by the relatively wide slit used, the line profiles have flatter tops and less extended bases (i.e., they are more “trapezoidal”) than the Gaussian fits. It is also apparent that the Gaussian fit is overestimating the line flux. In light of this, we developed a model of a Gaussian convolved with the slit (represented by a box function of fixed width, $0''.5$). The uncertainty obtained from the fit of this model to the tiled data is the observational error included in the tables of Chapters 3 and 4. Several other measures of uncertainty – including more detail on this convolved Gaussian – are discussed in the context of temperature fluctuations in § 6.4 of Chapter 6.

Both the [O III] $\lambda 5007$ and $\lambda 4959$ lines were observed simultaneously with the G430M/4961 grating setting. Because both transitions arise from the same upper level, the intrinsic flux ratio depends only on the transition probabilities (A-values) and wavelengths. As reported previously for similar STIS observations of the planetary nebula NGC 7009 obtained under program GO-8114 (PI RR) (Rubin et al., 2002), what we found was a surprising variation in the F_{5007}/F_{4959} ratio with position along the slit. This amounts to a variation in the ratio of roughly 3.0 ± 0.1 . Furthermore, it appears more-or-less periodic with an $\sim 3''.5$ cycle. As described in Rubin et al. (2002), according to Ted Gull (private communication), this is an instrumental effect and is a ratio of two fringe patterns. The source of the problem is a thin blocker filter that had to be matched with each grating and the best (and only) location that it could be placed was above the grating in a stable mounting.

To attempt to do anything about fringing would probably require a dedicated HST/STIS calibration program. If there were fringing in the F_{5007}/F_{4363} ratio at the same level as for the F_{5007}/F_{4959} ratio, the $\pm 3.3\%$ error would result in only a minor T_e error, e.g., ± 100 K at $T_e = 10^4$ K (see Chapter 6).

Chapter 3

Extinction corrections

Were it not for extinction, the Orion Nebula would appear much brighter. Typical optical depths reported are $\tau_V \sim 1$. From the shape of the extinction curve (e.g., see curves in Kim et al., 1994), the optical depth in the Lyman continuum (τ_{912}) would be several times this value. The relatively soft radiation from the primary ionization source (O star, θ^1 Ori C) cannot photoionize an optical depth to dust of much more than $\tau_{912} \sim 1$ indicating that a large part of the optical extinction must come from neutral material in the foreground. Further evidence for and properties of this “veil” are summarized by Abel et al. (2004).

All observed emission-line surface brightnesses or fluxes, from the infrared to ultraviolet, are affected by this wavelength-dependent extinction and must be corrected before further analysis and interpretation. Extinction is characterized by its wavelength dependence (shape) and the amount at a given wavelength (amplitude).

Stellar extinction deduced from stars in the nebula provides a useful reconnaissance of the shape of the Orion Nebula extinction curve, providing a continuous curve with which to make predictions (by interpolation) for any given line observed. We have reconsidered the wavelength dependence of the infrared, optical and ultraviolet extinction, presenting our results as a convenient analytic expression describing this shape (“normalized extinction curve”) in § 3.1.1. The amplitude by which to scale the normalized extinction curve can be determined for a given line of sight from nebular lines whose ratios of line emissivities are known from atomic theory (e.g., H I Balmer series). An optimal implementation is discussed in § 3.1.2. In § 3.2, we compare our extinction curve with the nebular extinction curve of Costero & Peimbert (1970) (hereafter CP70). In § 3.3, we discuss our extensive validation of the use of our stellar-based extinction curve for interpolating corrections to the nebular emission in the optical, the ultraviolet and the near-infrared.

3.1 Parameterization of extinction

We have already stressed how one requires a shape (s_λ) and amplitude (a) to describe the extinction:

$$\tau_\lambda = a s_\lambda. \quad (3.1)$$

For different lines of sight, grain properties like size distribution and composition are manifested in s_λ , while a scales with the column density of dust.

Let F represent the observed flux of a patch of nebula (surface brightness times solid angle) or of a star, with subscript o indicating the intrinsic flux – as it would have been had it not been affected by extinction τ . (The dependence on wavelength λ has been suppressed.) Thus $F/F_o = \exp(-\tau)$. For a uniformly bright nebular patch this is also the ratio of the specific intensities, I/I_o . Note that I_o can be predicted by atomic theory, from the emissivity j and (for most lines) the emission measure (Osterbrock, 1989). We adopt $I_o \propto j$ in the applications here, so that

$$F_\lambda = \text{constant} \times j_\lambda \exp(-a s_\lambda). \quad (3.2)$$

The logarithmic (base 10) extinction is $C = -\log(F/F_o) = -\log(\exp(-\tau)) = 0.4343\tau$. The extinction in magnitudes is $A = -2.5 \log(F/F_o) = 2.5C = 1.086\tau$. Given the linear transformations between A , C , and τ , a ratio like $A_{\lambda_1}/A_{\lambda_2}$ evaluated for two wavelengths is clearly interchangeable with the same ratio for C or τ .

In the literature there are various parameterizations of A , C , and τ that are worth distinguishing, since they imply different choices and normalizations of s_λ . Osterbrock (1989) uses $s_\lambda = 0.5\tau_\lambda/(\tau_{\text{H}\gamma} - \tau_{\text{H}\alpha})$ and comments on the utility of the differential form $s_\lambda - s_{\text{H}\beta}$. Note that he uses the notation f_λ where we use s_λ .

For nebular extinction, one often writes the logarithmic extinction as $C_\lambda = C_{\text{H}\beta}(1+f_\lambda)$, with $f_{\text{H}\beta} = 0$ (e.g., Peimbert & Torres-Peimbert, 1977). Then if we adopt $s_\lambda = (1+f_\lambda) \equiv \tau_\lambda/\tau_{\text{H}\beta}$ we have $a = C_{\text{H}\beta}/0.4343 = \tau_{\text{H}\beta}$.

For stellar extinction one often adopts the normalization $s_\lambda = A_\lambda/A_V \equiv \tau_\lambda/\tau_V$ (e.g., Cardelli et al., 1989, hereafter CCM89), in which case $a = A_V/1.086 = \tau_V$. In order to compare these differently normalized nebular and stellar extinctions, one can easily show that

$$1 + f_\lambda = \frac{A_\lambda/A_V}{A_{\text{H}\beta}/A_V}. \quad (3.3)$$

Differential extinction between two wavelengths can of course be defined in any system. For example, color excesses are differences in magnitudes, like $E_{B-V} = A_B - A_V$. These can lead to differential extinction curves with new normalizations, like $E_{\lambda-V}/E_{B-V} = (A_\lambda - A_V)/E_{B-V} = R_V(A_\lambda/A_V - 1)$, accompanied by the introduction of new parameters, like the ratio of total to selective extinction, $R_V = A_V/E_{B-V}$.

3.1.1 Determining the shape, s_λ : Stellar extinction

CCM89 defined the shape of optical stellar extinction analytically using a single parameter, R_V , to describe differences between lines of sight. The shape has been adopted in many investigations of the Orion Nebula (Baldwin et al., 1991; Osterbrock et al., 1992, hereafter OTV92; Greve et al., 1994), with $R_V = 5.5$.¹

Optical

Good optical spectrophotometry of the Orion stars (θ^1 and θ^2) is presented by Cardelli & Clayton (1988) (hereafter CC88) as $E_{\lambda-V}/E_{B-V}$. Using measurements from their graphs, we show that the optical data (and more scanty infrared data) are fit well by the CCM89 formula (dash-dotted line in our Fig. 3.1). The CC88 data (asterisks in Fig. 3.1) continue to about $3 \mu\text{m}^{-1}$ and show that there is a knee in the CCM89 curve at about $2.7 \mu\text{m}^{-1}$ ($\lambda 3700\text{\AA}$) that is perhaps a bit too high and sharp. Therefore, an analytic modification² has been made to the CCM89 formula (solid line) to round off the knee smoothly between 2.3 and $3.3 \mu\text{m}^{-1}$, fitting the CC88 data quite well.

Ultraviolet

The ultraviolet data come from IUE measurements by Bohlin & Savage (1981) (hereafter BS81) for the same Orion stars (see Fig. 3.1). The BS81 points (x) do not join on smoothly to the CC88 optical data. CC88 reanalysed the ultraviolet data, showing how it could reasonably be joined smoothly to their new accurate optical spectrophotometry (asterisks). The main effect on the BS81 data (x) is to move it up slightly (~ 0.25 mag shift), concomitantly increasing the expected ultraviolet extinction (see Fig. 3.1).

Note that in the ultraviolet, the analytic CCM89 formula does not fit either the CC88 or BS81 observations: the predicted bump is too strong. However, it is possible to adjust a few constants³ in the CCM89 formula to obtain a modified CCM89 curve (solid line) that runs smoothly through the CC88 data.

To gauge the importance of these modifications for the determination of extinction-corrected fluxes, consider the situation for the N II] $\lambda\lambda 2140\text{-}43$ pair near the peak of the extinction curve. The unmodified CCM89 curve exceeds ours by $\delta E_{\lambda-V}/E_{B-V} = 0.85$. For a typical value $E_{B-V} = 0.3$ the difference would be $\delta\tau = 0.23$; thus the N II] line would be 26% (0.1 dex)

¹ $R_V = 3.1$ in the diffuse interstellar medium (Savage & Mathis, 1979).

²CCM89's equations 3a and 3b are modified to $a(x) = 1.192528 + 0.27592(x - 2.3) - 0.15733(x - 2.3)^2$ and $b(x) = 0$, but only for $2.3 \mu\text{m}^{-1} < x < 3.3 \mu\text{m}^{-1}$.

³CCM89's equation 4b becomes: $b(x) = -2.9 + 1.825x + 0.93/[(x - 4.65)^2 + 0.263] + F_b(x)$ for $3.3 \mu\text{m}^{-1} < x < 8 \mu\text{m}^{-1}$.

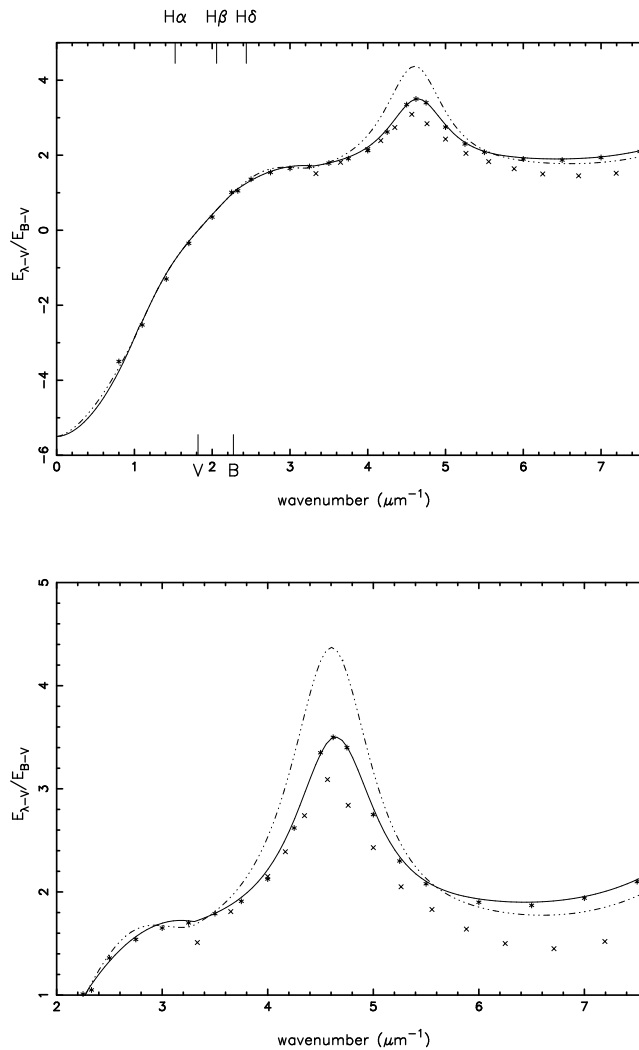


Figure 3.1 Analytic stellar-based extinction curves. (*top*) Dash-dotted line: CCM89 extinction curve presented here in differential form, $E_{\lambda-V}/E_{B-V}$ ($R_V = 5.5$) for ease of comparison with original BS81 data (\times). BS81 data should be adjusted by roughly $+0.25$ mag – the result of a calibration error pointed out by CC88, whose corrected stellar data are also plotted ($*$). Solid line: our modification of the CCM89 formulation to better fit the CC88 corrected data and shape near $2.7 \mu\text{m}^{-1}$. (*bottom*) Same as above, but the window has been scaled to accentuate the differences between CCM89 and our modified curve.

stronger if corrected according to the unmodified CCM89 curve.

Near infrared

Near $1 \mu\text{m}$ the CCM89 A_λ/A_V curve becomes a power law in λ^{-1} of index 1.6. Most stellar curves exhibit this “common power law” region of the extinction curve, independent of R_V (Martin & Whittet, 1990). The latter analysis suggests an index of 1.85, which we adopt in our extinction curve. This modification will not have an impact here, as the observations analysed do not extend much beyond $1 \mu\text{m}$.

3.1.2 Setting the amplitude, a : Optimal fitting of emission lines

Measurements of emission lines in nebulae are often used to gauge the extinction (e.g., CP70; OTV92; Greve et al., 1994; Esteban et al., 1998, hereafter EPTE98; Esteban et al., 2004, hereafter EPG04). If the shape s_λ of the extinction curve is known, then the amplitude a in equation 3.2 can be determined with even a single line pair from the same ion, assuming the relevant emissivities j_λ are known. The Balmer and Paschen lines are popular as their emissivities are well described by H I recombination theory and can be computed readily for various electron temperatures (T_e) and densities (N_e). See Storey & Hummer (1995) for detailed access to the results of their computations using an interactive data server. For the illustrations below we adopt case B emissivities with $T_e = 8000 \text{ K}$, $N_e = 2500 \text{ cm}^{-3}$ for FOS-1SW and STIS-SLIT1c (as determined from the nebular models in § 4.2.4), $T_e = 9000 \text{ K}$, $N_e = 5000 \text{ cm}^{-3}$ for the remainder of the STIS slits, and $T_e = 8300 \text{ K}$, $N_e = 8900 \text{ cm}^{-3}$ for the EPG04 observations (as determined from their temperature and density diagnostic ratios). Lines from other ions can be useful too (e.g., He I, [O II], [S II]), as further illustrated in § 4.2 (He I) and § 3.3 ([O II], [S II], He I).

Method

Sometimes the amplitude is taken from only one line ratio, like $\text{H}\alpha/\text{H}\beta$, but often other lines are available too. Past methodology has been to form various line ratios, compute the amplitude (e.g., the equivalent A_V) from each independently (sometimes with discrepant results), and then compute some average. A new approach adopted here is to fit the observed line fluxes directly to equation 3.2, not forming line ratios at all. The fit is carried out straightforwardly by non-linear least squares, with two unknowns: a and a constant multiplier (which is proportional to the ionic abundance through the emission measure.) In addition, from the goodness of fit of the data to the model, we obtain the 1σ confidence intervals on the parameters. This approach has some advantages: avoiding the inevitable bias from errors in the chosen normalizing line(s),

using a standard treatment of the measurement errors to weight the fit and hence avoiding the ambiguity associated with deciding what average amplitude to compute.

If later one wants to tabulate extinction-corrected line ratios relative to, say, $H\beta$ (or He I 4471 if He I lines are used in the extinction fitting), then the extinction model gives the best estimate of the corrected flux for this normalization, optimally consistent with all other lines in the series. When the He I recombination lines are fit simultaneously, then the optimal He^+/H^+ ratio is obtained, along with its formal error, without reference to particular He I to H I dereddened line ratios.

3.2 Comparison between stellar and nebular extinction curves

The CP70 nebular extinction curve is an alternative commonly used in the calculation of the extinction correction (EPTE98; EPG04). This curve was determined from optical and radio observations of four lines-of-sight in the Orion Nebula. The radio (1.95 cm) observations are used to determine the absolute extinction, $A_{H\beta}$, and the piecewise normalized extinction curve, $1 + f_\lambda$, is obtained for various lines:

$$f_\lambda = \frac{E_{\lambda-H\beta}}{A_{H\beta}}. \quad (3.4)$$

Calculations of $C_{H\beta}$ offer a simple means by which to compare our modified CCM89 curve with that of CP70. Performing a least-squares analysis on EPG04 data using the CP70 curve (and interpolations thereof), we get $C_{H\beta} = 0.65 \pm 0.03$, as compared to $C_{H\beta} = 0.85 \pm 0.04$ when we use our extinction curve. EPG04 had $C_{H\beta} = 0.76 \pm 0.08$ when using this same series (up to H15, $\lambda 3712$) of H I lines. However, this comparison of $C_{H\beta}$ is not enough. The shape of the CP70 curve is investigated more thoroughly in the following sections.

3.2.1 Infrared discrepancy

The zero-point is calculated by CP70 using radio data at (more or less) the same spatial position as the optical data. The remainder of CP70's f_λ is determined directly from specific Balmer or Paschen lines (as tabulated in Peimbert & Torres-Peimbert, 1977), so that most of the curve plotted in Figure 3.2 is interpolated (by CP70; Peimbert & Torres-Peimbert, 1977; Walter, 1993).

Near $1 \mu\text{m}^{-1}$, the CP70 curve is dramatically below our extinction curve (see Fig. 3.2). This is getting into the ‘‘common power law’’ region of the extinction curve mentioned in § 3.1.1. Nowhere is there evidence for the strong curvature implied in the CP70 extinction curve in the region from $1 \mu\text{m}^{-1}$ to zero wavenumber. The IR discrepancy might simply be the result of an inappropriate interpolation of the CP70 extinction curve. Looking at Figure 1 of CP70, it

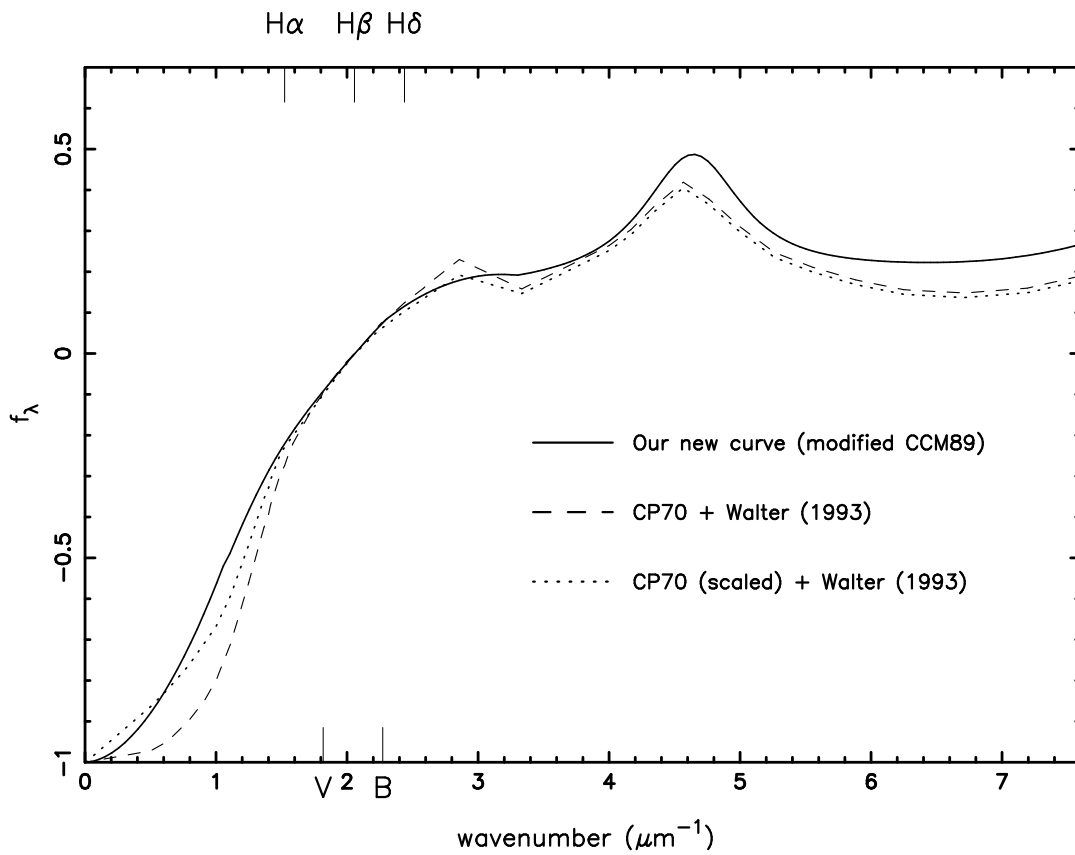


Figure 3.2 CP70 extinction curve (dashed line) including extension into the UV using uncorrected BS81 data following Walter (1993). Our extinction curve (solid curve) is overplotted, showing an unexplained discrepancy in the IR portion of the curves. The renormalized CP70 nebular extinction curve (dotted line) shows a marked improvement to the IR discrepancy. The UV portion of the scaled CP70 curve is rederived directly from the BS81 $E_{\lambda-V}/E_{B-V}$ data, using the new scaled f_V and f_B .

appears as if other interpolations to the V band are possible. If the interpolated f_V were a bit more negative (-0.12 or -0.13 instead of -0.094 would seem reasonable) and the CP70 curve (shown in our Fig. 3.2) were refit (and rescaled, see below), it would be noticeably closer to the stellar one from the optical through the near infrared.

The change in the interpolated f_V would affect R_V as derived from

$$R_V = \frac{1 + f_V}{f_B - f_V}, \quad (3.5)$$

resulting in $R_V = 4.5$ ($f_V = -0.12$) or 4.2 ($f_V = -0.13$) compared to the CCM89 and CP70 value of $R_V = 5.5$. However, the f_λ depend on comparing radio and optical data (see equation 3.4). This radio/optical comparison is almost certainly affected by a 10-20% reflection effect in the optical (see for e.g., Henney, 1998). Because of reflection, the lines like $H\beta$ are measured to be too bright relative to the radio, resulting in a low estimate of the absolute extinction, $A_{H\beta}$. In the optical where the differential extinction $E_{\lambda-H\beta}$ is not affected much by reflection, $f_\lambda = E_{\lambda-H\beta}/A_{H\beta}$ will be too high. A typical logarithmic extinction $C_{H\beta}$ ($C_{H\beta} = 0.4A_{H\beta}$) is 0.5, so that with $f_V = -0.12$, the logarithmic extinction at V is $0.5 \times (1 - 0.12) = 0.44$ or $A_V \sim 1$. A 20% reflection effect at V would cancel out real extinction at the level $\Delta A_V = 0.2$, lowering what should be 1 to 0.8 (apparent). Then 0.8×5.5 predicts $R_V(\text{apparent}) = 4.4$. Both the sign and order of magnitude of the reflection correction appear to be right. Note that there are other possibilities of systematic error as the radio/optical comparison also depends on the adopted temperature, matching the spots observed, etc.

To remedy this artificial alteration of R_V , we introduce a correction to $A_{H\beta}$ – effectively a rescaling of f_λ – to maintain $R_V = 5.5$. With $f_V = -0.12$ in our new interpolation of the CP data, one needs to divide all f_λ by a factor 1.198 to ensure that $R_V = 5.5$. This rescaled CP70 absolute extinction curve is presented in Figure 3.2.

The shape of our rescaled CP70 curve in the visible is similar to that of our modified CCM89 curve and so regardless of which of these is used, one should be able to get good differential fits to a series of optical lines. The differential extinction between $H\alpha$ ($1.52 \mu\text{m}^{-1}$) and $H\delta$ ($2.44 \mu\text{m}^{-1}$) is the same in both curves, and one obtains more or less the same $C_{H\beta}$ when fit to the Balmer lines, independent of the choice of curve (see § 3.3.1).

3.2.2 Ultraviolet

Walter (1993) extended the CP70 curve to the ultraviolet by attaching on the BS81 data assuming $R_V = 5.5$. This extended extinction curve was also described by Rubin et al. (1993). We have derived f_λ values from the original BS81 $E_{\lambda-V}/E_{B-V}$ form (as in Rubin et al., 1993) for both the CP70 and rescaled CP70 curves, generating a shape of the ultraviolet extinction for each, as seen in Figure 3.2. This extension lies below the CC88 revision of the BS81 data in

the ultraviolet and does not join smoothly to the optical portion of the CP70 curve. One of the reasons is that the CP70 curve has been extrapolated to $\lambda 3500$ (see their Table 2), incorrectly high, beyond the highest Balmer transitions that were observed (H9, $\lambda 3835$). When combined with the ultraviolet data (BS81 version) this sticks out as a kink in the curve at $\lambda 3500$; a smooth join, like all (stellar) extinction curves observed, is not possible. The reddening correction of a line like [O II] $\lambda 3727$ would be in doubt. Our modified CCM89 curve seems a more reliable alternative in this “extrapolated” region.

3.3 The stellar extinction curve: validation

It is important to address whether the shape of extinction derived from stars is appropriate for diffuse nebular emission, where the presence of scattered light might be an issue. We have therefore carried out extensive tests of this technique using consistent sets of nebular measurements of hydrogen lines in Orion, both from the literature (CP70; Peimbert & Torres-Peimbert, 1977; OTV92; EPTE98; EPG04) and from our HST and ground-based (Baldwin et al., 2000, hereafter BVV00; Blagrove et al., 2006a,b) observations.

Here we exploit our HST FOS and STIS (SLIT1c) observations for the line of sight 1SW (see Table 4.1) as, with the addition of several UV lines, they offer an extensive spectral range for the validation. As will be discussed, and is summarized in Figures 4.6 and 4.7 for FOS-1SW and STIS-SLIT1c, respectively, the data are well fit using our extinction curve.

3.3.1 Optical

In addition to our own STIS and FOS observations we have used others’ observations to examine the fit of the stellar-derived extinction curve in the optical. Using the extensive observations of EPG04, we have determined the best-fit extinction curve (see § 3.1.1) using the unblended H I Balmer lines (up to H17, $\lambda 3697$) and Paschen lines (up to P18, $\lambda 8438$), resulting in $C_{H\beta} = 0.82 \pm 0.04$. The resulting curve and residuals from this fit are shown in Figure 3.3. Over the spectral range that can be accessed by these lines, the fit is good, demonstrating that our extinction curve provides a good empirically-derived interpolation formula for differential extinction.

The EPG04 data were also fit using the scaled form of CP70 developed in § 3.2 and the same H I lines as above. The resulting curve and residuals are included in the bottom panel of Figure 3.3. We find $C_{H\beta} = 0.76 \pm 0.04$, in agreement with $C_{H\beta} = 0.76 \pm 0.08$ found by EPG04. As shown in the top and bottom panels of Figure 3.3 and discussed in § 3.2, the differential extinction is well represented by both our scaled CP70 and modified CCM89 curves.

We have also carried out fits of the various data sets using our curve and $R_V = 3.1$,

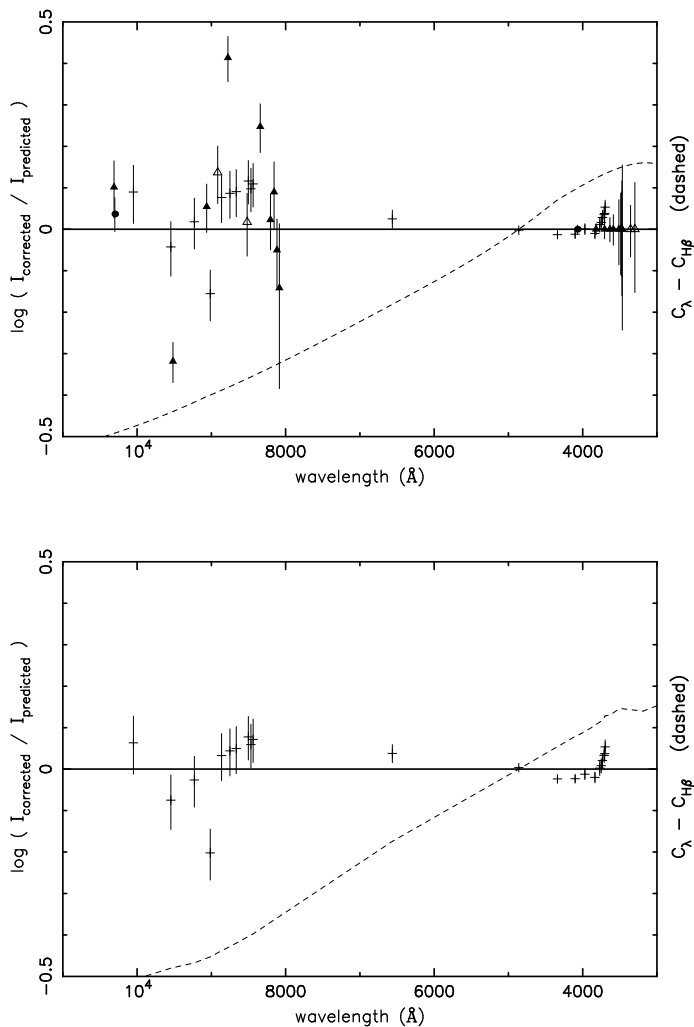


Figure 3.3 Best-fit differential extinction curves (dashed line) as determined from EPG04 H I Balmer and Paschen lines. Residuals and error bars are plotted for each H I emission line (+) used in the fit. (*top*) Our modified CCM89 extinction curve, $R_V = 5.5$, $C_{H\beta} = 0.82 \pm 0.04$. Also shown are data from common upper-level pairs of [S II] (•) and He I triplets (▲) and singlets (△) after applying this reddening correction. The optical member of the pair, usually with the lower error, has been plotted as $I_{corrected} = I_{predicted}$. (*bottom*) Scaled CP70 nebular curve, $C_{H\beta} = 0.76 \pm 0.04$. The common-upper level pairs are not included, but would result in a similar scatter about $\log(I_{corrected}/I_{predicted})=0$.

appropriate to the diffuse interstellar medium (Savage & Mathis, 1979). By comparison to the Orion curve (with $R_V = 5.5$) this curve is steeper throughout the optical, producing relatively less (more) extinction compared to $H\beta$ in the near-infrared (blue). This produces a markedly inferior fit.

3.3.2 Ultraviolet

Validation using nebular observations is especially important for the ultraviolet portion of the extinction model. The STIS and FOS spectra include the common upper level pair [O II] $\lambda\lambda 2471, 7325$ which can be used in this validation.

The [O II] $\lambda 2471$ line is actually a blend of transitions from $^2P_{1/2}$ and $^2P_{3/2}$ to $^4S_{3/2}$ (Osterbrock, 1989). Transitions from these upper levels also lead to the formation of a pair of blended near-infrared lines. Each upper level contributes a line to a blend at $\lambda 7321$ (transitions to $^2D_{5/2}$) and another line to a blend at $\lambda 7332$ (transitions to $^2D_{3/2}$); the combined near-infrared line will be denoted $\lambda 7325$. Thus the I_{2471}/I_{7325} line ratio is not quite the ideal case with a single common upper level in which the emissivities of the line pair are simply proportional to the radiative transition probabilities divided by the respective wavelengths. Instead, this line ratio depends on the collisional excitation of $^2P_{1/2}$ relative to $^2P_{3/2}$. However, calculations with a five-level atomic model show that the line ratio is not very sensitive to T_e and N_e over the range expected in the Orion Nebula. We adopt 0.75 using modern collision strengths (Pradhan et al., 2006) and older transition probabilities (Zeippen, 1982). We compare these results with a second ratio, 0.81 derived using the modern set of transition probabilities recommended by Wiese et al. (1996). These are both calculated for $T_e = 8000$ K and $N_e = 2500$ cm^{-3} (see § 4.2.4).

In Table 3.1, the observed I_{2471}/I_{7325} ratio is compared to that predicted using our extinction curve and H I lines for the two different sets of atomic data. Use of the modern transition probabilities results in a 15-20% over-prediction, whereas the older transition probabilities result in a slightly lower 10-15% over-prediction. These modern transition probabilities have been found to yield anomalous density and temperatures from [O II] lines (see EPG04; Wang et al., 2004; Blagrove et al., 2006a) and thus it is not unexpected that the older transition probabilities yield a slightly more consistent result.

As a check on the theoretical predictions, we have also examined the [O II] I_{7321}/I_{7332} line ratio which is slightly more sensitive to the relative upper level populations, but not sensitive to the applied reddening correction. The prediction is 1.25 using Zeippen (1982) transition probabilities and 1.23 using Wiese et al. (1996) transition probabilities. Our ratios are 1.21-1.24 for the STIS observations. Other observations in Orion by OTV92 give 1.134, while BVV00 find 1.25 and EPG04 find 1.30. Our ability to predict accurately (within 15%) both the I_{7321}/I_{7332}

Table 3.1. Observed ratios of common-upper-level lines, I_{2471}/I_{7325} , and predictions from theory

Dataset	Theory		Uncorrected	Corrected for reddening using H I lines
	Z82 ^a	W96 ^b		
FOS-1SW	0.75	0.81	0.35 ± 0.01	0.71 ± 0.01
STIS-SLIT1b	0.75	0.81	0.19 ± 0.01	0.61 ± 0.02
STIS-SLIT1c	0.75	0.81	0.27 ± 0.01	0.66 ± 0.01

^aUsing Zeppen (1982) transition probabilities

^bUsing Wiese et al. (1996) transition probabilities

line ratio and the common-upper-level line ratio I_{2471}/I_{7325} supports the validity of our analytic extinction curve in the UV, and therefore the discussion of the He I ultraviolet decrement in § 4.2.

3.3.3 Near infrared

Similarly, the [S II] common upper-level line pair I_{10300}/I_{4072} can be used to confirm the validity of the extinction curve in the infrared. Our data do not extend into the infrared, but those of EPG04 do. The three observed lines at $\lambda 10300$ and two at $\lambda 4072$ have been corrected for extinction using our best-fit extinction curve (see § 3.3.1). Since this is a ratio being used for validation and is not in the fit, the visible line (which tends to have the lower error) has been set to $I_{corrected}/I_{predicted} = 1$ in Figure 3.3. The agreement is good.

As pointed out in Porter et al. (2006), EPG04 have also observed a series of He I common upper-level line pairs. These line pairs have been overplotted on Figure 3.3 too. The IR pair members have $I_{corrected}/I_{predicted} = 1.2 \pm 0.5$. While there are large differences between the observed and predicted line strengths, there is no significant systematic bias, indicating that our extinction curve is also valid between the near-IR and near-UV.

Chapter 4

He I decrements and more on extinction corrections

To complete a full spectral analysis in the UV and visible, we have had to develop and test an extinction curve amended slightly from those often applied to visible Orion Nebula observations (Costero & Peimbert, 1970; Cardelli et al., 1989, hereafter CP70 and CCM89, respectively). In the course of this work we examined the decrement within various series of He I lines, planning to use these lines to constrain extinction, primarily in the ultraviolet. As reported in Martin et al. (1996) and now fully described in § 4.2, our FOS and STIS observations have revealed a decrement within the ultraviolet $2^3S - n^3P$ series that is not in accord with case B (as defined in Baker & Menzel, 1938) recombination theory (Smits, 1996; Benjamin et al., 1999; Porter et al., 2005), and cannot be explained by extinction effects. This anomalous decrement stems from the metastability of 2^3S , leading to radiative transfer effects that then affect other series (Robbins, 1968; Osterbrock, 1989). We compare the predictions of this theory with our set of HST FOS and STIS observations – the first detailed observational analysis of He I UV lines originating from high n terms. In a comprehensive examination including other datasets, we also show quantitatively how the same theory self-consistently accounts for resonance fluorescence enhancement observed in several other lines of two related series. The agreement is quite remarkable.

4.1 Observations

HST FOS and STIS spectra were obtained with spectral coverage from the UV (1600Å) through to the visible (7400Å) for two lines of sight (roughly 1SW and x2, as discussed in Chapter 2). The FOS aperture has a diameter $0''.86$ and the STIS slit is $52'' \times 0''.5$ (refer to Fig. 4.1) of which only (the roughly central) $28''$ are recorded using the STIS UV detectors (FUV-MAMA,

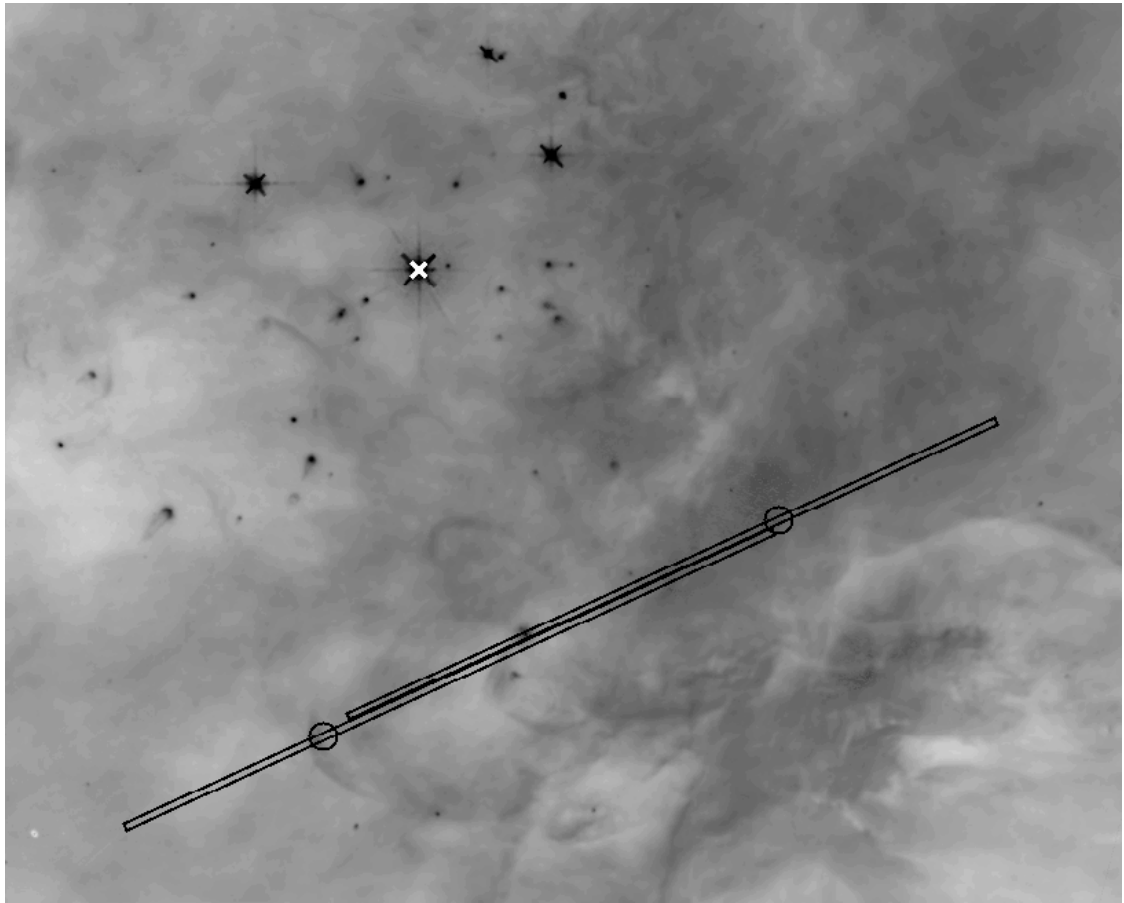


Figure 4.1 HST STIS Slit 1 ($52'' \times 0.5''$, right) and Slit 2 (left) shown overlapping with HST FOS positions 1SW (right circle) and x2 (left circle) (Baldwin et al., 1996; Rubin et al., 1997), respectively. Slit positions are overlaid on F656N ($H\alpha$) WFPC2 image. θ^1 Ori C is marked with a \times . N is up and E to the left.

NUV-MAMA). The STIS UV and optical spectra were adjusted to align spatially using a bright feature common to all spectra: proplyd 159-350 (O'Dell & Wen, 1994).

The placement of Slit 1 (see Fig. 4.1) was such that it was centred on a region of the nebula where there is an extinction gradient. Because of this, we divided the $52'' \times 0.5''$ slit into four $13'' \times 0.5''$ sections¹, labelled “a” through “d”. The different spatial coverage of the MAMA and CCD detectors means that the outer two sections (SLIT1a and SLIT1d) have reliable coverage only in the visible, but the central two sections (SLIT1b and SLIT1c) have coverage in the

¹All STIS spectra have small fiducial bar sections which interfere with the spatial coverage of the spectra. For this reason, when average surface brightnesses of tiles are being calculated along the slit, these fiducial bar sections are avoided.

visible and the UV. The same sectioning was done for Slit 2 (x2, see Fig. 4.1). However, there was little change in the extinction across Slit 2 so the two central sections (SLIT2b and SLIT2c) should be similar.

The reduction of STIS spectra was performed as in Chapter 2 and the reduction of FOS spectra as in Rubin et al. (1998). Our HST STIS (SLIT1b, SLIT1c, SLIT2b, SLIT2c) and FOS (1SW) observations are presented in Table 4.1.

A wavelength-dependent extinction correction must still be applied to the entire spectrum (UV through visible/near-IR). The development and validation of an analytic UV through IR extinction curve is discussed in Chapter 3. To ensure that any extinction curve is well constrained, we must maximize the number of lines used in its determination. In § 4.2, we discuss the basis for the inclusion of He I (especially He I UV) lines.

4.2 Anomalous He I decrements

Based on predictions from recombination theory we have used the H I Balmer and Paschen series to calibrate the reddening curve (see Chapter 3). The same should be possible using recombination theory (Smits, 1996; Benjamin et al., 1999; Porter et al., 2005) and observations of the He I lines (see energy-level diagrams in Fig. 4.2).

4.2.1 Extinction-corrected data

Table 4.2 presents the He I data from our FOS-1SW and (the section of our STIS spectrum that covers 1SW) STIS-SLIT1c observations as well as complementary data from comprehensive ground-based studies by Osterbrock et al. (1992), Esteban et al. (1998), Baldwin et al. (2000), and Esteban et al. (2004) (hereafter OTV92, EPTE98, BVV00, EPG04, respectively).

Each of the He I lines has been corrected for reddening using our best-fit curve as normalized using the observed H I Balmer (and Paschen, where available) series lines, and each line's case B prediction. Case B predictions depend on T_e and N_e (Storey & Hummer, 1995) and so are unique to each observation set: $T_e = 9000$ K, $N_e = 4000$ cm⁻³ (OTV92); $T_e = 9500$ K, $N_e = 5700$ cm⁻³ (EPTE98, position 2); $T_e = 9000$ K, $N_e = 5000$ cm⁻³ (BVV00); $T_e = 8300$ K, $N_e = 8900$ cm⁻³ (EPG04); $T_e = 8000$ K, $N_e = 2500$ cm⁻³ (FOS-1SW, STIS-SLIT1c).

As is common, the line strengths are given relative to the singlet line $\lambda 4471$.

Table 4.1. HST STIS V2 and FOS observations prior to reddening correction ($I_\lambda/I_{H\beta}$)

ID	λ (Å)	SLIT1b	SLIT1c	SLIT2b	SLIT2c	FOS-1SW
C III]	1907	0.0371 ± 0.0021	0.0534 ± 0.0012
C III]	1909	0.0316 ± 0.0020	0.0444 ± 0.0008
[O II]	2470	0.0393 ± 0.0013	0.0752 ± 0.0013	0.0323 ± 0.0014	0.0454 ± 0.0012	0.1164 ± 0.0009
He I	2697	0.0017 ± 0.0009
He I	2723	0.0023 ± 0.0049	0.0029 ± 0.0001	0.0032 ± 0.0010
He I	2764	0.0048 ± 0.0004	0.0041 ± 0.0001	0.0048 ± 0.0010
He I+[Fe IV]	2829	0.0081 ± 0.0006
He I	2945	0.0083 ± 0.0007	0.0091 ± 0.0003	0.0110 ± 0.0006
He I	3188	0.0186 ± 0.0006
H I	3697	0.0114 ± 0.0231	0.0068 ± 0.0004	0.0127 ± 0.0102	0.0044 ± 0.0088	...
H I	3704	0.0108 ± 0.0098	0.0143 ± 0.0061	0.0187 ± 0.0042	0.0140 ± 0.0017	...
H I	3712	0.0109 ± 0.0012	0.0139 ± 0.0006	0.0101 ± 0.0125	0.0101 ± 0.0031	...
H I+[S III]	3722	0.0212 ± 0.0011	0.0278 ± 0.0005	0.0223 ± 0.0008	0.0268 ± 0.0016	...
[O II]	3726	0.4797 ± 0.0142	0.6041 ± 0.0148	0.4898 ± 0.0137	0.5228 ± 0.0184	...
[O II]	3729	0.2309 ± 0.0213	0.2649 ± 0.0220	0.2456 ± 0.0184	0.2546 ± 0.0124	...
H I	3734	0.0212 ± 0.0019	0.0204 ± 0.0009	0.0147 ± 0.0005	0.0180 ± 0.0012	...
H I	3750	0.0190 ± 0.0016	0.0236 ± 0.0006	0.0243 ± 0.0021	0.0190 ± 0.0008	0.0242 ± 0.0015
H I	3771	0.0230 ± 0.0011	0.0299 ± 0.0005	0.0281 ± 0.0011	0.0276 ± 0.0007	0.0338 ± 0.0011
H I	3798	0.0308 ± 0.0008	0.0395 ± 0.0006	0.0297 ± 0.0009	0.0361 ± 0.0010	0.0444 ± 0.0011
He I	3820	0.0085 ± 0.0010
He I+H I	3889	0.1298 ± 0.0017
He I+H I+[Ne III]	3965	0.1886 ± 0.0026
He I	4026	0.0167 ± 0.0007
H I	4340	0.4004 ± 0.0048	0.4170 ± 0.0048	0.3777 ± 0.0035	0.4064 ± 0.0059	0.4444 ± 0.0021
[O III]	4363	0.0091 ± 0.0003	0.0095 ± 0.0002	0.0074 ± 0.0003	0.0115 ± 0.0003	...
He I	4388	0.0048 ± 0.0002	0.0045 ± 0.0001	0.0039 ± 0.0002	0.0048 ± 0.0001	0.0042 ± 0.0006
He I	4471	0.0397 ± 0.0005	0.0432 ± 0.0005	0.0359 ± 0.0005	0.0398 ± 0.0006	0.0416 ± 0.0008
H I	4861	1.0000 ± 0.0111	1.0000 ± 0.0110	1.0000 ± 0.0073	1.0000 ± 0.0131	1.0000 ± 0.0081
He I	4922	0.0093 ± 0.0010	0.0098 ± 0.0002	0.0142 ± 0.0010	0.0106 ± 0.0007	0.0121 ± 0.0013
[O III]	4959	1.2387 ± 0.0148	1.0750 ± 0.0115	1.2212 ± 0.0096	1.2046 ± 0.0165	...
[O III]	5007	3.7521 ± 0.0408	3.2426 ± 0.0345	3.6822 ± 0.0270	3.6453 ± 0.0473	...
He I	5016	0.0271 ± 0.0008	0.0233 ± 0.0006	0.0214 ± 0.0006	0.0206 ± 0.0005	...
[Cl III]	5518	0.0049 ± 0.0003	0.0039 ± 0.0001	0.0028 ± 0.0002	0.0036 ± 0.0003	...
[Cl III]	5538	0.0075 ± 0.0002	0.0064 ± 0.0001	0.0048 ± 0.0001	0.0063 ± 0.0001	...
[N II]	5755	0.0095 ± 0.0003	0.0148 ± 0.0002	0.0081 ± 0.0003	0.0107 ± 0.0002	...
He I	5876	0.1797 ± 0.0020	0.1703 ± 0.0018	0.1643 ± 0.0010	0.1812 ± 0.0023	0.1449 ± 0.0013
[N II]	6548	0.2341 ± 0.0031	0.2667 ± 0.0031	0.2101 ± 0.0021	0.2461 ± 0.0035	...
H I	6563	4.4094 ± 0.0510	3.9699 ± 0.0498	3.9989 ± 0.0294	4.4652 ± 0.0665	4.2067 ± 0.0336 ^a
H I	6563	3.7418 ± 0.0265 ^b
[N II]	6583	0.7209 ± 0.0102	0.8343 ± 0.0098	0.6460 ± 0.0071	0.7654 ± 0.0106	...
He I	6678	0.0549 ± 0.0008	0.0504 ± 0.0007	0.0476 ± 0.0004	0.0539 ± 0.0009	0.0439 ± 0.0031 ^a
He I	6678	0.0433 ± 0.0016 ^b
[S II]	6716	0.0344 ± 0.0007	0.0318 ± 0.0004	0.0358 ± 0.0007	0.0337 ± 0.0006	...
[S II]	6731	0.0637 ± 0.0012	0.0636 ± 0.0008	0.0660 ± 0.0009	0.0662 ± 0.0011	...
He I	7065	0.1176 ± 0.0013	0.1058 ± 0.0012	0.1036 ± 0.0008	0.1169 ± 0.0015	0.1014 ± 0.0035
[Ar III]	7136	0.2679 ± 0.0034	0.2457 ± 0.0029	0.2298 ± 0.0020	0.2742 ± 0.0040	...
C II	7236	0.0048 ± 0.0004	0.0041 ± 0.0002	0.0038 ± 0.0002	0.0041 ± 0.0004	...
O I	7254	0.0022 ± 0.0002	0.0019 ± 0.0001	0.0014 ± 0.0001	0.0022 ± 0.0001	...
He I	7281	0.0119 ± 0.0003	0.0112 ± 0.0001	0.0095 ± 0.0002	0.0113 ± 0.0002	...
[O II]	7319	0.1144 ± 0.0014	0.1547 ± 0.0019	0.0896 ± 0.0010	0.1215 ± 0.0020	0.3344 ± 0.0056
[O II]	7330	0.0936 ± 0.0012	0.1276 ± 0.0015	0.0723 ± 0.0008	0.1006 ± 0.0016	Blend

^aFOS/G780 grating^bFOS/G570 grating

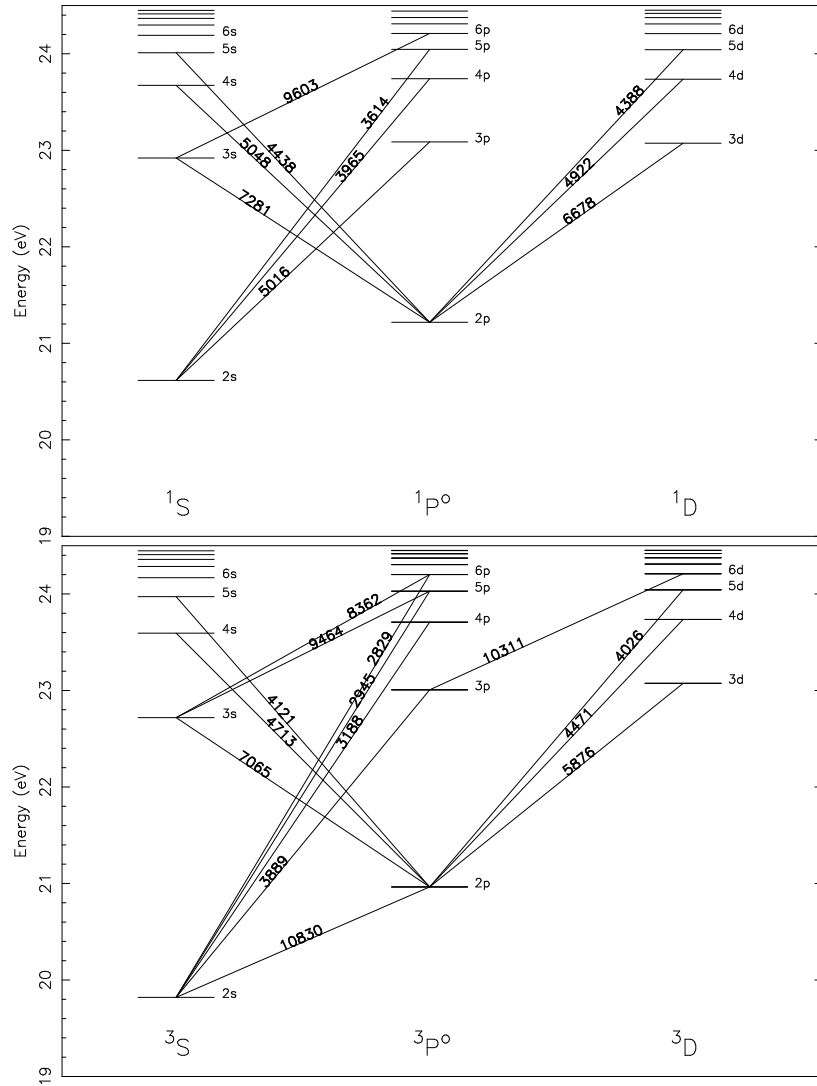


Figure 4.2 Energy-level diagram of He I, showing (*top*) singlet and (*bottom*) triplet transitions. For the sake of clarity, not all observed transitions are shown.

Table 4.2. He I relative intensities, I_λ/I_{4471} , after correcting for reddening using H I Balmer (and Paschen) lines and our extinction curve

λ (Å)	n	Predicted				Observed					
		Case B	Model M	Model K	OTV92	EPTE98	BVV00	EPG04	FOS-1SW	STIS-SLIT1c	
(1)	(2)	(3)	(4)	(5)	(6)	(7)	(8)	(9)	(10)	(11)	
$2^3S - n^3P$											
3889	3	2.315	0.780	0.580	1.019 ± 0.362	1.165 ± 0.242	1.126 ± 0.191	0.950 ± 0.152	1.005 ± 0.131	...	
+H I	...	4.575 ^a	3.389	2.651	3.112 ± 0.561	3.518 ± 0.393	3.702 ± 0.163	3.267 ± 0.103	3.425 ± 0.080	...	
3188	4	0.878	0.441	0.337	0.933 ± 0.487	0.536 ± 0.043	0.521 ± 0.018	...	
2945	5	0.414	0.290	0.229	0.310 ± 0.017	0.257 ± 0.010	
2829	6	0.228	0.200	0.162	
+ [Fe IV]	0.268	0.248	0.232 ± 0.017	...	
2764	7	0.141	0.140	0.116	0.140 ± 0.030	0.120 ± 0.004	
2723	8	0.093	0.100	0.085	0.093 ± 0.028	0.085 ± 0.003	
2696	9	0.065	0.073	0.063	0.048 ± 0.026	...	
$2^1S - n^1P$											
5016	3	0.566	0.517	0.488	...	0.496 ± 0.070	0.551 ± 0.014	0.502 ± 0.007	...	0.473 ± 0.013	
3965	4	0.221	0.206	0.193	...	0.201 ± 0.045	0.236 ± 0.006	0.209 ± 0.007	
+H I/[Ne III]	4.973	4.187	4.405 ± 0.794	4.924 ± 0.117	...	
3614	5	0.108	0.104	0.095	0.146 ± 0.037	0.085 ± 0.019	0.109 ± 0.003	0.104 ± 0.007	
3448	6	0.059	0.061	0.052	0.105 ± 0.055	0.068 ± 0.006	
3355	7	0.037	0.041	0.032	0.208 ± 0.109	0.042 ± 0.006	
3297	8	0.024	0.029	0.021	0.027 ± 0.008	
$2^3P - n^3S$											
7065	3	0.612	1.714	1.833	1.414 ± 0.255	...	1.951 ± 0.079	1.832 ± 0.130	1.617 ± 0.065	1.458 ± 0.024	
4713	4	0.103	0.153	0.157	0.150 ± 0.038	0.145 ± 0.032	0.153 ± 0.005	0.151 ± 0.002	
4121	5	0.038	0.046	0.046	0.046 ± 0.013	0.049 ± 0.011	0.044 ± 0.001	0.049 ± 0.002	
3868	6	0.018	0.020	0.020	0.019 ± 0.003	0.017 ± 0.002	
+ [Ne III]	2.846	2.846	3.382 ± 0.610	
3733	7	0.010	0.011	0.011	0.010 ± 0.001	0.011 ± 0.004	
3652	8	0.006	0.007	0.007	0.005 ± 0.002	
3599	9	0.004	0.004	0.004	
3563	10	0.003	0.003	0.003	
3537	11	0.002	0.002	0.002	0.003 ± 0.001	
$2^3P - n^3D$											
5876	3	2.789	2.815	2.820	2.736 ± 0.493	3.119 ± 0.349	3.255 ± 0.121	3.165 ± 0.100	2.731 ± 0.058	2.902 ± 0.044	
4471	4	1.000	1.000	1.000	1.000 ± 0.150	1.000 ± 0.100	1.000 ± 0.023	1.000 ± 0.010	1.000 ± 0.019	1.000 ± 0.011	
4026	5	0.472	0.466	0.466	0.484 ± 0.103	0.440 ± 0.062	0.497 ± 0.014	0.479 ± 0.015	0.431 ± 0.021	...	
3820	6	0.254	0.254	0.254	0.237 ± 0.059	0.240 ± 0.054	0.232 ± 0.006	0.262 ± 0.008	0.227 ± 0.027	...	
3705	7	0.155	0.155	0.155	Blend	...	0.176 ± 0.005	0.153 ± 0.008	
3634	8	0.102	0.102	0.102	0.129 ± 0.038	0.096 ± 0.021	0.129 ± 0.004	0.104 ± 0.007	
3587	9	0.071	0.071	0.071	0.090 ± 0.026	0.075 ± 0.017	0.083 ± 0.003	0.071 ± 0.006	
3554	10	0.052	0.051	0.051	0.071 ± 0.021	0.038 ± 0.008	0.057 ± 0.002	0.050 ± 0.005	
3531	11	0.038	0.038	0.037	0.060 ± 0.017	...	0.037 ± 0.002	0.039 ± 0.007	
3513	12	0.029	0.029	0.029	0.046 ± 0.013	...	0.034 ± 0.002	0.028 ± 0.005	
3499	13	0.023	0.023	0.023	0.042 ± 0.022	...	0.030 ± 0.002	0.023 ± 0.005	
3488	14	0.019	0.018	0.018	0.028 ± 0.014	0.018 ± 0.004	
3479	15	0.015	0.015	0.015	0.015 ± 0.008	0.013 ± 0.003	
3474	16	0.012	0.013	0.012	0.013 ± 0.004	
3468	17	0.010	0.011	0.011	0.007 ± 0.003	
$2^1P - n^1S$											
7281	3	0.151	0.155	0.145	0.129 ± 0.032	...	0.153 ± 0.004	0.152 ± 0.012	...	0.148 ± 0.002	
5048	4	0.038	0.040	0.036	...	0.042 ± 0.009	0.043 ± 0.002	0.126 ± 0.003	
4438	5	0.015	0.016	0.015	0.017 ± 0.006	0.013 ± 0.004	0.0149 ± 0.0004	0.016 ± 0.001	
4169	6	0.008	0.008	0.007	0.009 ± 0.004	0.011 ± 0.003	0.0111 ± 0.0008	0.013 ± 0.001	
4024	7	0.005	0.005	0.004	0.0055 ± 0.0005	

Table 4.2—Continued

λ (Å)	n	Predicted				Observed					
		Case B (3)	Model M (4)	Model K (5)	OTV92 (6)	EPTE98 (7)	BVV00 (8)	EPG04 (9)	FOS-1SW (10)	STIS-SLIT1c (11)	
$2^1P - n^1D$											
6678	3	0.784	0.737	0.731	0.704 ± 0.149	0.939 ± 0.133	0.955 ± 0.024	0.912 ± 0.055	0.729 ± 0.031	0.743 ± 0.013	
4922	4	0.272	0.258	0.256	0.238 ± 0.051	0.263 ± 0.037	0.289 ± 0.007	0.267 ± 0.004	0.265 ± 0.028	0.204 ± 0.005	
4388	5	0.125	0.120	0.119	0.112 ± 0.033	0.117 ± 0.026	0.121 ± 0.003	0.120 ± 0.003	0.103 ± 0.016	0.105 ± 0.003	
4144	6	0.067	0.066	0.065	0.058 ± 0.017	0.060 ± 0.013	0.067 ± 0.002	0.063 ± 0.003	
4009	7	0.040	0.040	0.040	0.042 ± 0.012	0.046 ± 0.010	0.040 ± 0.001	0.037 ± 0.002	
3927	8	0.026	0.026	0.026	
$3^3S - n^3P$											
9464	5	0.023	0.053	0.054	0.080 ± 0.020	0.027 ± 0.004	
8362	6	0.015	0.030	0.029	Blend	0.033 ± 0.004	
7816	7	0.010	0.018	0.017	0.014 ± 0.004	0.022 ± 0.002	
7500	8	0.007	0.012	0.011	0.012 ± 0.004	0.014 ± 0.001	
7298	9	0.005	0.008	0.007	0.008 ± 0.003	...	0.0090 ± 0.0003	0.0095 ± 0.0010	
7161	10	0.004	0.006	0.005	0.0067 ± 0.0002	0.0070 ± 0.0007	
7062	11	0.003	0.004	0.004	0.0046 ± 0.0002	0.0048 ± 0.0005	
6989	12	0.002	0.003	0.003	0.0030 ± 0.0001	0.0032 ± 0.0004	
6934	13	0.002	0.003	0.002	0.0025 ± 0.0002	0.0033 ± 0.0005	
6890	14	0.001	0.002	0.002	
6856	15	0.001	0.002	0.002	0.0022 ± 0.0004	
$3^1S - n^1P$											
9603	6	0.005	0.006	0.005	0.011 ± 0.003	
8915	7	0.004	0.004	0.003	0.007 ± 0.002	0.0057 ± 0.0009	
8518	8	0.003	0.003	0.002	0.004 ± 0.002	0.0029 ± 0.0005	
8266	9	0.002	0.002	0.002	Blend	
8094	10	0.001	0.002	0.001	0.005 ± 0.002	0.0015 ± 0.0003	
7972	11	0.001	0.002	0.0012 ± 0.0003	
$3^3P - n^3D$											
10311	6	0.029	0.029	0.029	0.012 ± 0.006	0.038 ± 0.006	
9517	7	0.019	0.019	0.019	0.009 ± 0.001	
9063	8	0.013	0.013	0.013	0.015 ± 0.002	
8777	9	0.009	0.009	0.009	0.010 ± 0.003	0.024 ± 0.003	
8583	10	0.007	0.007	0.007	
8445	11	0.005	0.005	0.005	
8342	12	0.004	0.004	0.004	0.0067 ± 0.0009	
8265	13	0.003	0.003	0.003	Blend	
8204	14	0.003	0.003	0.003	0.0026 ± 0.0004	
8156	15	0.002	0.002	0.002	0.0022 ± 0.0004	
8116	16	0.002	0.002	0.002	0.0016 ± 0.0003	
8084	17	0.001	0.002	0.002	0.0007 ± 0.0003	
$C_{H\beta}$ (from H I lines)					0.61 ± 0.11	0.50 ± 0.21	0.30 ± 0.12	0.82 ± 0.04	0.52 ± 0.05	0.66 ± 0.04	
$C_{H\beta}$ (from H I + He I subset)					0.57 ± 0.06	0.60 ± 0.12	0.31 ± 0.07	0.82 ± 0.07	0.52 ± 0.03	0.69 ± 0.05	
He^+/H^+ (from H I + He I subset)					0.098 ± 0.007	0.084 ± 0.007	0.081 ± 0.005	0.088 ± 0.003	0.083 ± 0.002	0.095 ± 0.003	
He^+/H^+ (from source, select He I lines)					0.089 ± 0.002	0.089 ± 0.009	...	0.087 ± 0.001	

^aCase B H I + He I blend determined using a typical He^+/H^+ (0.088) as found from these data

The quoted uncertainties for OTV92 and EPTE98 are estimated from their description of the quality of the data. Those of EPG04 are directly from the per cent errors in their Table 2. BVV00 and FOS-1SW uncertainties were determined using the signal to noise ratio, S/N , as found from fitting each emission line to a five-parameter (area, central wavelength, FWHM, continuum baseline and continuum slope) single Gaussian model (see § 2.1). This S/N is combined with the integrated line flux to produce the uncertainty. The STIS data is similarly fit with a model which takes into account the $0''.5$ STIS slit width (see § 6.4). Again, the resultant S/N from this fit is combined with the integrated flux to determine the uncertainty.

4.2.2 Case B

He I case B predictions for FOS-1SW and STIS-SLIT1c T_e and N_e ($n \leq 5$, Porter et al. 2005; $n > 5$, Smits 1996) are shown in column (3) of Table 4.2 and are quite representative for the range of nebular densities and temperatures we consider.

Most of the reddening-corrected singlet and triplet lines (cols. (6)-(11)) are well-represented by case B recombination alone (col. (3)).

In comparing their case B results with the OTV92 observations, Benjamin et al. (1999) noted (their Figs. 2a and 2b) that the lines (singlets and triplets) shortward of $\lambda 3820$ were consistently brighter than predicted, increasingly with decreasing wavelength, except surprisingly (to us) $\lambda 3188$ which, if reduction by radiative transfer effects were accounted for as discussed below, should have been overpredicted, but appears to be accurately predicted. They suggested that this discrepancy shortward of $\lambda 3820$ could be due to radiative transfer effects, though this seems very unlikely given the lines involved. If alternatively this arose from inadequate/unmodeled extinction corrections, there would have to be a very sudden (relative) decrease in the extinction in order for the extinction-corrected lines not to appear so bright. It is informative to note that the discrepancy in this instance cannot be explained by the inaccurate extrapolation of CP70 as discussed in § 3.2.2 (since CP70 is not used in the extinction correction). It seems most probable that there is a systematic problem with the absolute calibration used and/or significant measurement errors due to strong atmospheric extinction varying rapidly with wavelength for $\lambda < 3500 \text{ \AA}$ (OTV92). See also § 4.2.5, Figure 4.5.

In their discussion of nebular model predictions of the He I lines compared to the EPG04 observations, Porter et al. (2006) have noted that He I lines of the $2^1S - n^1P$ series in the same wavelength range ($\lambda\lambda 3448, 3355, 3297$) are also brighter than the expected case B predictions. Analysing the line ratios between successive members of this series (their Figs. 1 and 5) they conclude that there are problems with these observational results, possibly with the extinction (over-)correction. The same observations, corrected according to our best-fit extinction curve, are presented in Table 4.2, where it can be seen that the observations and case B (or our full

models) are in agreement within the errors.

As seen in Table 4.2, use of our extinction curve brings $\lambda 7281$ into agreement with the case B predictions (as suggested by Porter et al., 2006). Many of the other near-IR lines observed by EPG04 are still scattered about the best-fit expectation (Table 4.2 and graphically in § 3.3.3, Figure 3.3). These infrared lines are difficult to observe because of atmospheric effects (OTV92) and the errors might be underestimated (Porter et al., 2006), but the important thing to note is that there does not appear to be any systematic discrepancy – except as noted below for the infrared lines of the triplet series $3\ ^3S - n\ ^3P$.

4.2.3 Anomalous decrements

Despite the validity of case B for the prediction of most lines, there remains a systematic mismatch between observed and predicted ratios for a number of the He I lines from the series $2\ ^3S - n\ ^3P$, $2\ ^3P - n\ ^3S$, $3\ ^3S - n\ ^3P$, and $2\ ^1S - n\ ^1P$.

For the triplet lines, the underlying reason is the metastability of the $2\ ^3S$ term which can only be depopulated through photoionization, through collisional transitions to $2\ ^1S$ and $2\ ^1P$, or through the (strongly forbidden) radiative transition $1\ ^1S - 2\ ^3S$ (Osterbrock, 1989). The visible/near-UV lines of the $2\ ^3S - n\ ^3P$ series (including $\lambda\lambda 3889$, 3188, 2945, 2829, etc.) are affected by self-absorption from the metastable $2\ ^3S$ term to the corresponding $n\ ^3P$ term. This results in case B recombination theory over-predicting these lines (see Table 4.2). Note that although $\lambda 3889$ is blended with a Balmer line, it is still possible to predict the observed intensity of the He I component and use it as a valuable diagnostic. For the entries in Table 4.2 we used case B He I predictions and the He^+/H^+ derived from the other lines to deblend $\lambda 3889$; this also enables a “case B” prediction for the blend (see col. (3) in Table 4.2). The space-based observations that we report here are particularly valuable for verifying the expected diminution of this self-absorption effect in higher members of the series. This appears to be the case as discussed in the modeling below.

For self-consistency, there must also be a detectable resonance fluorescence enhancement of the $2\ ^3P - n\ ^3S$ series as some of the electrons promoted by self-absorption to $n\ ^3P$ radiatively cascade back down to $2\ ^3S$ via alternate routes. Indeed, this is quite evident in the $2\ ^3P - n\ ^3S$ series, primarily in $\lambda 7065$ ($n = 3$), but detectable in $\lambda 4713$ ($n = 4$) and $\lambda 4121$ ($n = 5$) too (see Table 4.2). Similarly, we expect to see an enhancement of other triplet series including the near-IR series, $3\ ^3S - n\ ^3P$. The data in Table 4.2 show this enhancement. We will return to analysis of these series in § 4.2.5.

The singlet lines of the series $2\ ^1S - n\ ^1P$, $\lambda 5016$ ($n = 3$) (and to a much lesser extent $\lambda 3965$, $n = 4$) are also observed to be consistently less than the case B prediction. As discussed in Porter et al. (2006), this is most probably a result of UV lines ($\lambda 537$, $1\ ^1S - 3\ ^1P$ and $\lambda 522$,

$1^1S - 4^1P$) escaping the nebula, resulting in case B being shifted slightly toward case A (as defined in Baker & Menzel, 1938).

4.2.4 Photoionization models

The CLOUDY photoionization code (Ferland et al., 1998) accounts for many radiative transfer effects, including those relating to the metastable 2^3S term. It is also possible to run CLOUDY models that exclude all line transfer in order to investigate its importance. With this in mind, a series of CLOUDY photoionization models was developed.

Self-absorption effects depend on the line width because this affects the opacity. The He I lines (among others) observed in the ground-based echelle spectra (BVV00, Blagrove et al., 2006a,b) have line widths (FWHM) in excess of the Doppler/thermal and instrumental widths. When the Doppler/thermal and instrumental widths are subtracted (in quadrature) from the measured FWHM there remains an unaccounted for contribution to the broadening which has been labelled as “turbulence”. In the case of the He I singlet lines (which do not have any fine-structure levels and therefore will not have any further FWHM contribution from a line blend) in the 1SW ground-based echelle spectra (Blagrove et al., 2006b), we find $\text{FWHM}_{turb} = 15.5 \pm 2.4 \text{ km s}^{-1}$. This is quite consistent with the “turbulence” contribution quoted in O’Dell et al. (2003) for the He I $\lambda 5876$ triplet line: $18.4 \pm 2.9 \text{ km s}^{-1}$. This latter line and other triplet lines have another broadening contribution brought on by transitions in the fine structure (J levels) and therefore are slightly less reliable in the determination of the additional “turbulence” contribution. As was mentioned in O’Dell et al. (2003) and is also found here, the magnitude of the “turbulence” contribution to the line width appears to decrease as one probes along the line of sight from cooler (associated with H I and He I) to hotter (associated with [O III], [O II], [S II], etc.) regions of the nebula. As the He I recombination lines preferentially probe the cooler region of the nebula, the “turbulence” that these lines reveal is an upper limit for the nebular model.

This turbulent contribution to the line width will affect the magnitude of the radiative transfer effect on the $2^3S - n^3P$ series of lines (and the related lines, like $\lambda 7065$), as it broadens the lines and lowers the effective optical depth and line trapping. The effects from radiative transfer should diminish as the turbulence is increased. To investigate the effects of this change in turbulence on line predictions, we developed a series of constant density (10^4 cm^{-3}) and constant temperature (10^4 K) CLOUDY models each with a different turbulence parameter, $v_{turb} = \text{FWHM}_{turb} / \sqrt{4 \ln 2}$ (as defined in CLOUDY), and excluding “induced processes” (as defined in CLOUDY, these include continuum fluorescent excitation and induced recombination). Then each of these constant-turbulence models was varied in thickness, in order to develop plots of line ratios as a function of $\tau_0(\lambda 3889)$ – the optical depth at the center of He I $\lambda 3889$

for zero turbulence velocity (see Fig. 4.3). For the normalizing line we use $\lambda 4471$ which is not significantly affected by radiative transfer. Our Figure 4.3 can be compared with Figure 4.5 of Osterbrock (1989), which shows similar variation, but in the latter case as a result of changes in the nebular expansion velocity. At $\tau_0 = 0$ all models reduce, as is expected, to their case B values.

Figure 4.4 plots the line strengths, $I_\lambda/I_{\lambda 4471}$, as a function of each model’s “turbulence” parameter for fixed $\tau_0(\lambda 3889) \sim 27$ which is appropriate to the column density of our full nebular model below. In this case to enable the best comparison between the CLOUDY model predictions and our observations, the “induced processes” are included (regardless, in our full model the relative importance of the induced processes is much diminished because the nebula becomes optically thick to the continuum radiation responsible for these excitations). From the overplotted observed $I_{\lambda 7065}/I_{\lambda 4471}$ in Figure 4.4, we would predict $v_{turb} = 20 - 30 \text{ km s}^{-1}$, whereas from $\lambda 3889$ (deblended), $\lambda 3188$ and $\lambda 2945$, $v_{turb} = 10 - 12 \text{ km s}^{-1}$. This latter prediction is consistent with the “turbulence” contribution ($\text{FWHM}_{turb} \sim 16 \text{ km s}^{-1}$; i.e., $v_{turb} \sim 10 \text{ km s}^{-1}$) which was determined from the observed He I lines’ FWHM above. The value $v_{turb} = 12 \text{ km s}^{-1}$ will be adopted in the CLOUDY models discussed hereafter. Models with this value of the turbulence should be able to roughly explain the observations of the hitherto anomalous He I lines. As expected, the results of the full nebular models to be discussed (Table 4.2) are slightly different than the results for constant N_e and T_e in Figure 4.4, in particular giving even better agreement for $\lambda 7065$.

Our full nebular models are similar to the Orion Nebula model discussed in Baldwin et al. (1991) – i.e., a closed geometry and constant pressure. Two such models (see Tables 4.3 and 4.4) were created, as was done in Chapter 7: one with a Mihalas stellar atmosphere model (Mihalas, 1972) and H II region abundances as defined in CLOUDY (Baldwin et al., 1991; Rubin et al., 1991; OTV92) (model M); and one with a Kurucz stellar atmosphere model (Kurucz, 1979) and EPG04 Orion Nebula abundances (model K). The Mihalas (non-LTE) stellar atmosphere has been shown to best represent the incident continuum radiation (BVV00), but to test the robustness of our results we also include the Kurucz (LTE, line-blanketed) stellar atmosphere in our second model. Each of these nebular models has $v_{turb} = 12 \text{ km s}^{-1}$. The other parameters (density, radius, etc.) were varied so as to best reproduce the SLIT1c H β surface brightness and the temperature- and density-sensitive lines, as summarized in Table 4.5 for both models.

The models’ predictions of the He I lines given in columns (4) and (5) in Table 4.2 include the deviation from case B introduced by the metastable 2^3S term. The effect of this metastability is reflected in the models’ (non-zero) line optical depth, $\tau(\lambda 3889)=13$. Note that He I $\lambda 3889$ ($n = 3$) appears as a blend with H I $\lambda 3889$ and He I $\lambda 2829$ ($n = 6$) appears as a blend with [Fe IV] $\lambda 2829$. Neither of these blends is included in our quantitative analysis, but the predicted

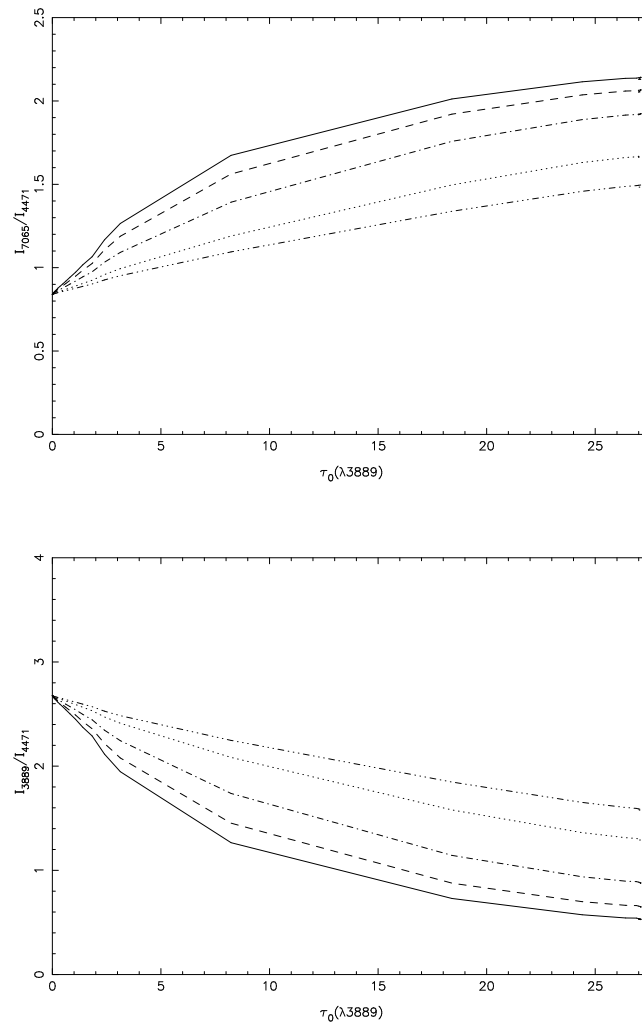


Figure 4.3 Variation in line flux (I_λ/I_{4471}) as a function of $\tau_0(\lambda 3889)$, the optical depth at the center of $\lambda 3889$ for $v_{turb} = 0$ (solid line). (top) I_{7065}/I_{4471} ; (bottom) I_{3889}/I_{4471} . For the same physical models, the changes when $v_{turb} = 5, 10, 20,$ and 30 km s^{-1} are also shown.

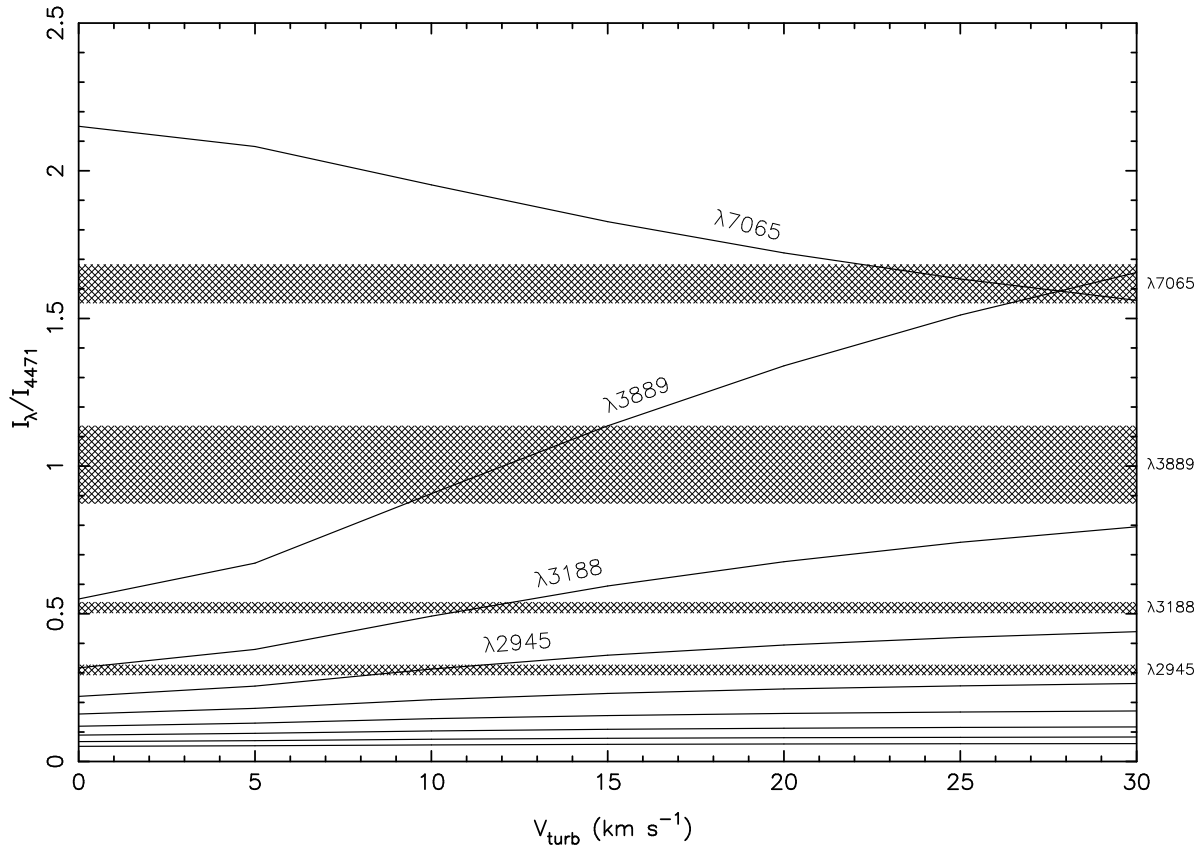


Figure 4.4 Variation of He I lines as a function of v_{turb} in the full nebular model. The hatched boxes represent the dereddened FOS-1SW observations (and uncertainties) of $\lambda\lambda 7065, 3889$ (deblended), 3188, and 2945 (from Table 4.2).

Table 4.3. CLOUDY input parameters for models M and K

Quantity	Model M ^a	Model K ^b
T_{eff} (K)	35200	41200
$\log\phi(\text{H})$	13.05	13.10
radius (pc)	0.27	0.27
$\log n_{\text{H}}(\text{inner})$ (cm^{-3})	3.4	3.4
Turbulence (km s^{-1})	12	12

^aMihalas (1972) stellar atmosphere

^bKurucz (1979) stellar atmosphere

Table 4.4. Model abundances relative to H ($12+\log(X/H)$)

Element	Model M ^a	Model K ^b
(1)	(2)	(3)
He	10.98	10.98
C	8.48	8.42
N	7.85	7.73
O	8.60	8.65
Ne	7.78	8.05
S	7.00	7.22
Ar	6.48	6.62
Cl	5.00	5.46
Fe	6.48	6.48

^aCLOUDY H II region abundances from Baldwin et al. (1991); Rubin et al. (1991) and OTV92

^bEPG04 abundances

value for each is shown in a separate row in Table 4.2.

Models M and K were modified to exclude radiative transfer in the nebula in order to investigate further the validity of the CLOUDY models. This exclusion has the expected effect on the lines: returning the triplet line predictions to roughly their case B values and those singlets connected radiatively to the ground state are reduced to their case A values.

4.2.5 Comparison with observations

We have modeled the extinction correction for OTV92, EPTE98, BVV00, EPG04 and our FOS-1SW and STIS-SLIT1c observations using our extinction curve and the H I Balmer (and Paschen, where available) lines and a subset of He I lines, excluding lines from the triplet series $2^3S - n^3P$ ($\lambda\lambda 3889, 3188, 2945, 2829$), $2^3P - n^3S$ ($\lambda\lambda 7065, 4713, 4121$) and $3^3S - n^3P$ (all lines) and the singlet line, $\lambda 5016$. Our $C_{H\beta}$ from the fit of H I and the subset of He I lines is consistent with that found using H I lines alone (see end of Table 4.2), suggesting that both H I and this subset of He I lines are reliable determinants of the extinction correction.

For comparison with these extinction-corrected observations, $I_{corrected}$, we adopt separately predictions, $I_{predicted}$, from case B and CLOUDY model M. Values of $\log(I_{corrected}/I_{predicted})$ are plotted in Figure 4.5 for all observed members of four series for both case B and model M predictions. Many data sets are shown, but EPTE98 is excluded simply to avoid visual clutter.

Table 4.5. Constraints on model parameters

Quantity	Orion Nebula (1SW)		
	SLIT1c	Model M	Model K
SB(H β) ^a	66.8 \pm 0.7	64.1	63.2
λ 5007/H β	3.13 \pm 0.05	3.5	4.3
λ 5007/ λ 3726 ^b	4.0 \pm 0.1	5.9	6.6
(λ 4959 + λ 5007)/ λ 4363 ^c	389 \pm 7	421.0	392.1
(λ 6548 + λ 6583)/ λ 5755 ^c	64 \pm 1	61.6	65.0
λ 6731/ λ 6716 ^d	2.00 \pm 0.04	2.1	2.0
λ 3726/ λ 3729 ^d	2.3 \pm 0.2	2.5	2.4
λ 1907/ λ 1909 ^d	1.20 \pm 0.04	1.1	1.2
(λ 3726 + λ 3729)/ λ 7325 ^d	6.4 \pm 0.6	4.7	6.0

^aSurface brightness in units of 10^{-13} ergs cm⁻² s⁻¹ arcsec⁻²

^bIonization indicator

^cTemperature indicator

^dDensity indicator

For the $2^3P - n^3D$ series, which includes $\lambda 4471$ ($n = 4$), case B and model M are in close agreement. This triplet series is not significantly affected by radiative transfer effects and the theory and observations are in close agreement. The other triplet series are clearly affected, by self-absorption ($2^3S - n^3P$) or by resonance fluorescence enhancement ($2^3P - n^3S$, $3^3S - n^3P$). Case B is a poor approximation, but the agreement between theory and observations improves dramatically as we switch from case B to model M.

Two features deserve further discussion. The OTV92 data shortward of 3700 \AA (including $\lambda 3188$) most likely suffer from systematic errors (§ 4.2.2). This can be seen graphically in the $2^3P - n^3D$ series of Figure 4.5 when comparing OTV92 (circles, no uncertainty bars) and others' datasets; the OTV92 data points (with one exception, $\lambda 3479$) all lie significantly apart from the other data. Second, $\lambda 9464$ measured by EPG04 appears to be too faint. This line has a number of neighbouring near-IR H I Paschen lines and He I lines which appear to be well-fit by our extinction correction. There would have to be a large sudden increase in the amount of extinction for the extinction correction to be able to account for this anomaly. This suggests that $\lambda 9464$ may have a larger than reported measurement uncertainty (see also § 4.2.2 and Porter et al., 2006).

4.2.6 Extinction corrections revisited

The STIS and FOS data are corrected for extinction using our extinction curve, the unblended H I lines, the subset of He I lines and the common-upper-level pair of [O II] lines (refer to § 4.2.5 and § 3.3.2). These are presented in Table 4.6 relative to the $H\beta$ predicted from the fit, along with the derived $C_{H\beta}$.

In Figure 4.6, we show the extinction-corrected FOS-1SW line intensities compared to the case B theory (the residuals of the fit) as well as the extinction correction applied (here expressed differentially with respect to $C_{H\beta}$). The He I lines $\lambda\lambda 7065$, 3188, and 2945 are excluded from the fit, but their values relative to case B and model M predictions are overplotted. Model M provides a better prediction for the lines affected by radiative transfer.

The analysis for the SLIT1c data is shown in a similar way in Figure 4.7. The He I lines $\lambda\lambda 7065$, 5016 and 2945 (and H I line $\lambda 3704$, because of large uncertainty) are excluded from the fit, but their values relative to case B and model M are overplotted. Again, model M provides a better prediction for the lines affected by radiative transfer.

In fitting the UV extinction curve, we conclude that $\lambda 3889$ (a blend in any case), $\lambda 3188$, $\lambda 2945$, and $\lambda 2829$ (also a blend) should be excluded – pending correction for radiative transfer effects – but that lines associated with higher n (i.e., $n > 6$) can be included to ensure a more robust determination. The visible/IR extinction correction can be strengthened by including case B predictions for He I triplet and singlet lines, but as discussed above, we conclude that

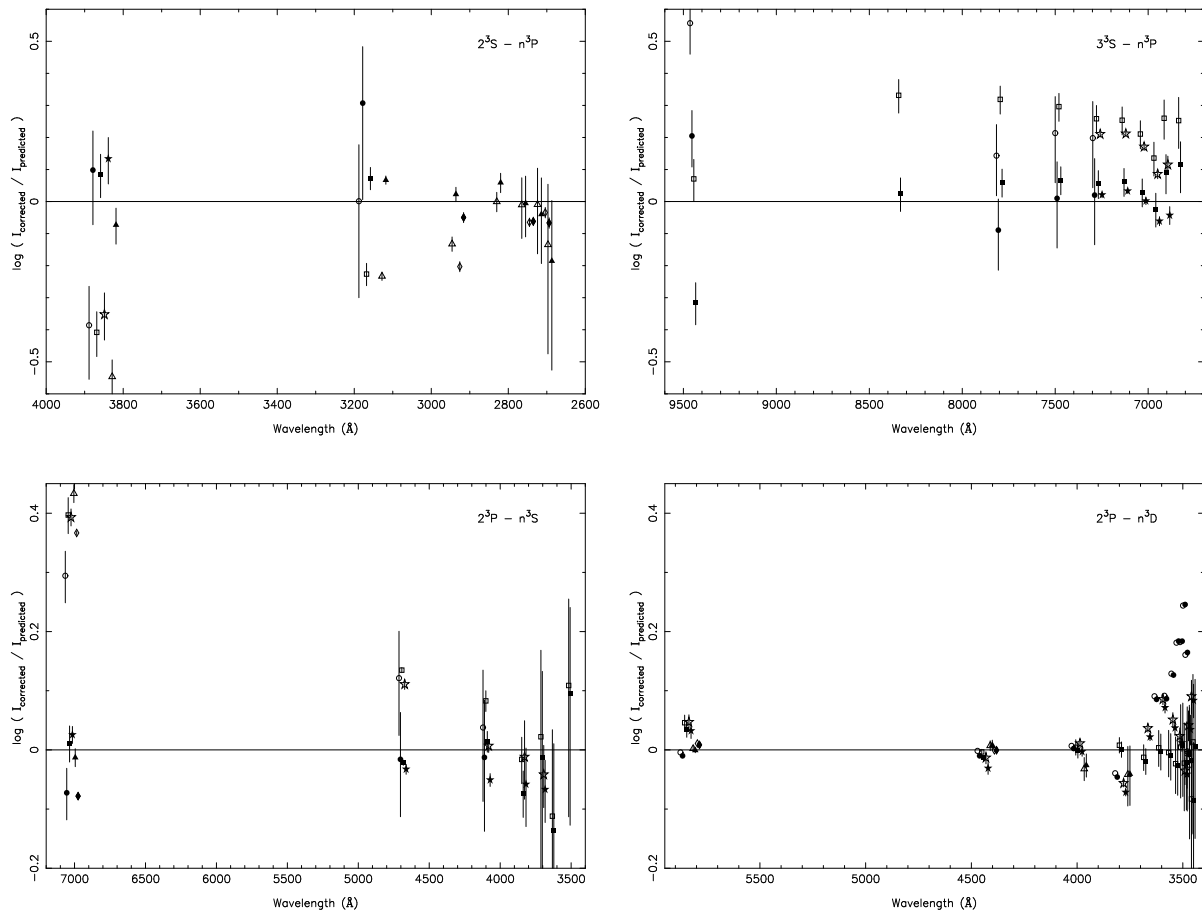


Figure 4.5 Observed He I decrements (OTV92, \bullet ; BVV00, \star ; EPG04, \blacksquare ; FOS-1SW, \blacktriangle ; STIS-SLIT1c, \blacklozenge) compared to case B (open symbols) and CLOUDY model M (filled symbols) predictions for four series. The corrected values, $I_{corrected}$, are determined from our extinction curve, which is calibrated for each dataset using H I and a subset of He I lines (see § 4.2.5). The 68.3% confidence intervals are shown for each member, n , of the series. For visual clarity, each set of observed data has been offset by 10\AA , and the uncertainties have been excluded for the OTV92 data in the $2^3P - n^3D$ series (in the UV, these uncertainties are close to ± 0.2 dex). Note the change in scale between the top and bottom figures.

Table 4.6. Dereddened HST STIS V2 and FOS observations ($I_\lambda/I_{H\beta, predicted}$)

ID	λ (Å)	SLIT1b	SLIT1c	SLIT2b	SLIT2c	FOS-1SW
C III]	1907	0.0691 ± 0.0038	0.0872 ± 0.0029
C III]	1909	0.0591 ± 0.0038	0.0726 ± 0.0022
[O II]	2470 ^c	0.0718 ± 0.0023	0.1208 ± 0.0035	0.0550 ± 0.0024	0.0807 ± 0.0032	0.1613 ± 0.0024
He I	2697 ^c	0.0021 ± 0.0012
He I	2723 ^c	0.0036 ± 0.0078	0.0042 ± 0.0002	0.0041 ± 0.0012
He I	2764 ^c	0.0075 ± 0.0007	0.0059 ± 0.0002	0.0061 ± 0.0013
He I+[Fe IV]	2829	0.0102 ± 0.0007
He I	2945	0.0126 ± 0.0011	0.0126 ± 0.0006	0.0136 ± 0.0007
He I	3188	0.0229 ± 0.0007
H I	3697 ^c	0.0161 ± 0.0326	0.0089 ± 0.0006	0.0175 ± 0.0140	0.0061 ± 0.0123	...
H I	3704 ^c	0.0152 ± 0.0137	0.0187 ± 0.0080	0.0256 ± 0.0057	0.0194 ± 0.0025	...
H I	3712 ^c	0.0153 ± 0.0017	0.0182 ± 0.0009	0.0138 ± 0.0171	0.0139 ± 0.0042	...
H I+[S III]	3722	0.0298 ± 0.0015	0.0363 ± 0.0011	0.0305 ± 0.0010	0.0370 ± 0.0025	...
[O II]	3726	0.6725 ± 0.0199	0.7875 ± 0.0267	0.6690 ± 0.0187	0.7199 ± 0.0330	...
[O II]	3729	0.3234 ± 0.0298	0.3451 ± 0.0298	0.3353 ± 0.0252	0.3503 ± 0.0199	...
H I	3734 ^c	0.0297 ± 0.0027	0.0266 ± 0.0013	0.0201 ± 0.0007	0.0247 ± 0.0018	...
H I	3750 ^c	0.0265 ± 0.0022	0.0306 ± 0.0011	0.0330 ± 0.0028	0.0260 ± 0.0013	0.0285 ± 0.0018
H I	3771 ^c	0.0319 ± 0.0015	0.0387 ± 0.0011	0.0380 ± 0.0014	0.0377 ± 0.0015	0.0397 ± 0.0014
H I	3798 ^c	0.0425 ± 0.0011	0.0509 ± 0.0014	0.0400 ± 0.0012	0.0490 ± 0.0019	0.0520 ± 0.0015
He I	3820 ^c	0.0099 ± 0.0012
He I+H I	3889	0.1499 ± 0.0027
He I+H I+[Ne III]	3965	0.2155 ± 0.0041
He I	4026 ^c	0.0188 ± 0.0009
H I	4340 ^c	0.4817 ± 0.0058	0.4817 ± 0.0126	0.4542 ± 0.0042	0.4822 ± 0.0158	0.4784 ± 0.0065
[O III]	4363	0.0109 ± 0.0003	0.0109 ± 0.0003	0.0088 ± 0.0003	0.0136 ± 0.0005	...
He I	4388 ^c	0.0057 ± 0.0002	0.0051 ± 0.0002	0.0046 ± 0.0002	0.0057 ± 0.0002	0.0045 ± 0.0007
He I	4471 ^c	0.0457 ± 0.0006	0.0481 ± 0.0013	0.0415 ± 0.0005	0.0452 ± 0.0015	0.0436 ± 0.0010
H I	4861 ^c	1.0085 ± 0.0112	1.0044 ± 0.0260	1.0382 ± 0.0076	0.9990 ± 0.0323	0.9671 ± 0.0146
He I	4922 ^c	0.0092 ± 0.0010	0.0097 ± 0.0003	0.0145 ± 0.0010	0.0104 ± 0.0007	0.0115 ± 0.0012
[O III]	4959	1.2109 ± 0.0145	1.0535 ± 0.0272	1.2355 ± 0.0097	1.1675 ± 0.0380	...
[O III]	5007	3.6142 ± 0.0393	3.1408 ± 0.0809	3.6795 ± 0.0269	3.4824 ± 0.1124	...
He I	5016	0.0260 ± 0.0007	0.0226 ± 0.0008	0.0213 ± 0.0006	0.0196 ± 0.0007	...
[Cl III]	5518	0.0040 ± 0.0002	0.0033 ± 0.0001	0.0025 ± 0.0002	0.0030 ± 0.0002	...
[Cl III]	5538	0.0062 ± 0.0002	0.0055 ± 0.0001	0.0043 ± 0.0001	0.0052 ± 0.0002	...
[N II]	5755	0.0074 ± 0.0002	0.0122 ± 0.0003	0.0068 ± 0.0002	0.0084 ± 0.0003	...
He I	5876 ^c	0.1363 ± 0.0015	0.1365 ± 0.0035	0.1345 ± 0.0008	0.1371 ± 0.0044	0.1179 ± 0.0019
[N II]	6548	0.1507 ± 0.0020	0.1877 ± 0.0049	0.1501 ± 0.0015	0.1587 ± 0.0052	...
H I	6563 ^c	2.8274 ± 0.0327	2.7863 ± 0.0741	2.8477 ± 0.0209	2.8694 ± 0.0949	3.0933 ± 0.0466 ^a
H I	6563 ^c	2.7514 ± 0.0402 ^b
[N II]	6583	0.4601 ± 0.0065	0.5834 ± 0.0153	0.4582 ± 0.0050	0.4896 ± 0.0160	...
He I	6678 ^c	0.0343 ± 0.0005	0.0346 ± 0.0009	0.0332 ± 0.0003	0.0337 ± 0.0012	0.0317 ± 0.0023 ^a
He I	6678 ^c	0.0313 ± 0.0012 ^b
[S II]	6716	0.0213 ± 0.0005	0.0217 ± 0.0006	0.0247 ± 0.0005	0.0209 ± 0.0007	...
[S II]	6731	0.0392 ± 0.0007	0.0432 ± 0.0012	0.0455 ± 0.0006	0.0409 ± 0.0014	...
He I	7065	0.0669 ± 0.0008	0.0675 ± 0.0018	0.0668 ± 0.0005	0.0668 ± 0.0022	0.0694 ± 0.0026
[Ar III]	7136	0.1499 ± 0.0019	0.1547 ± 0.0041	0.1460 ± 0.0013	0.1542 ± 0.0051	...
C II	7236	0.0026 ± 0.0002	0.0026 ± 0.0002	0.0024 ± 0.0001	0.0023 ± 0.0002	...
O I	7254	0.0012 ± 0.0001	0.0011 ± 0.0000	0.0009 ± 0.0001	0.0012 ± 0.0001	...
He I	7281 ^c	0.0065 ± 0.0001	0.0068 ± 0.0002	0.0058 ± 0.0001	0.0061 ± 0.0002	...
[O II]	7319 ^c	0.0613 ± 0.0008	0.0942 ± 0.0025	0.0549 ± 0.0006	0.0655 ± 0.0022	0.2203 ± 0.0047
[O II]	7330 ^c	0.0500 ± 0.0006	0.0775 ± 0.0020	0.0442 ± 0.0005	0.0541 ± 0.0018	Blend
$C_{H\beta}$		0.89 ± 0.05	0.71 ± 0.04	0.74 ± 0.08	0.87 ± 0.06	0.54 ± 0.02
He^+/H^+		0.090 ± 0.003	0.094 ± 0.003	0.089 ± 0.004	0.089 ± 0.003	0.083 ± 0.002

^aFOS/G780 grating^bFOS/G570 grating^cLines used to determine reddening curve.

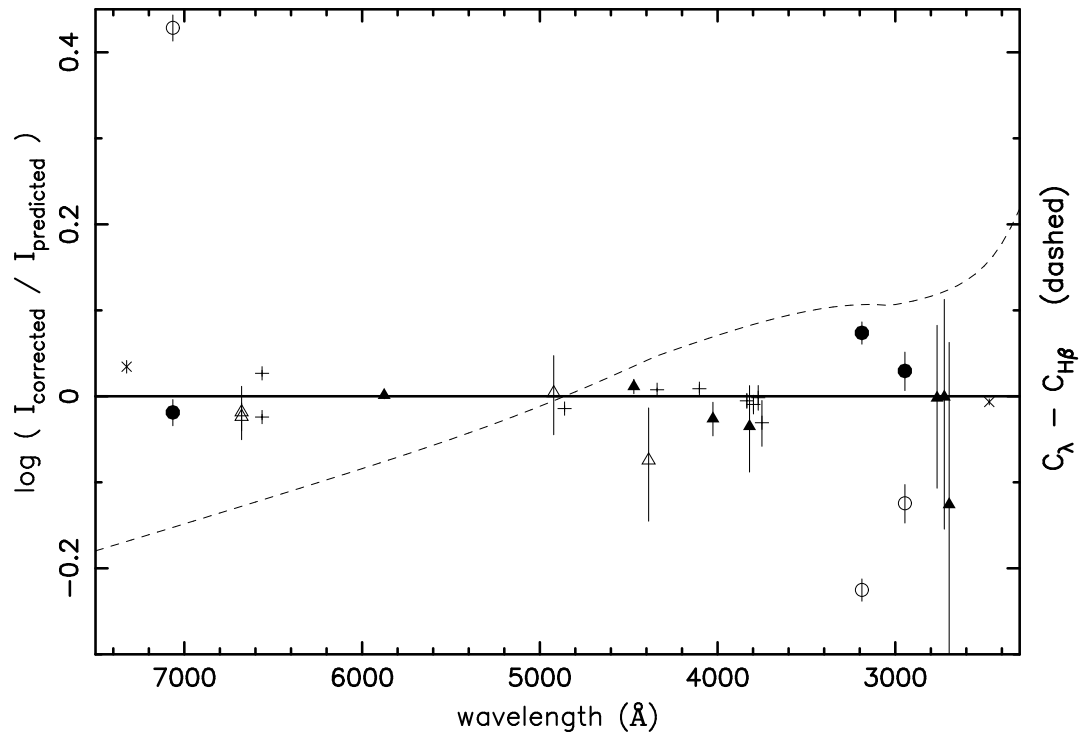


Figure 4.6 Differential extinction curve for FOS-1SW (dashed line) presented as $C_\lambda - C_{H\beta}$. Residuals, $\log(I_{corrected}/I_{predicted})$ (relative to case B), and 1σ errors are plotted for each emission line used in the fit: H I (+), He I (triplets, \blacktriangle ; singlets, \triangle) and [O II] (\times). The three He I lines most affected by radiative transfer ($\lambda\lambda 7065$, 3188 , and 2945) are not included in the fit, but are plotted relative to case B values (\circ) and model M predictions (\bullet).

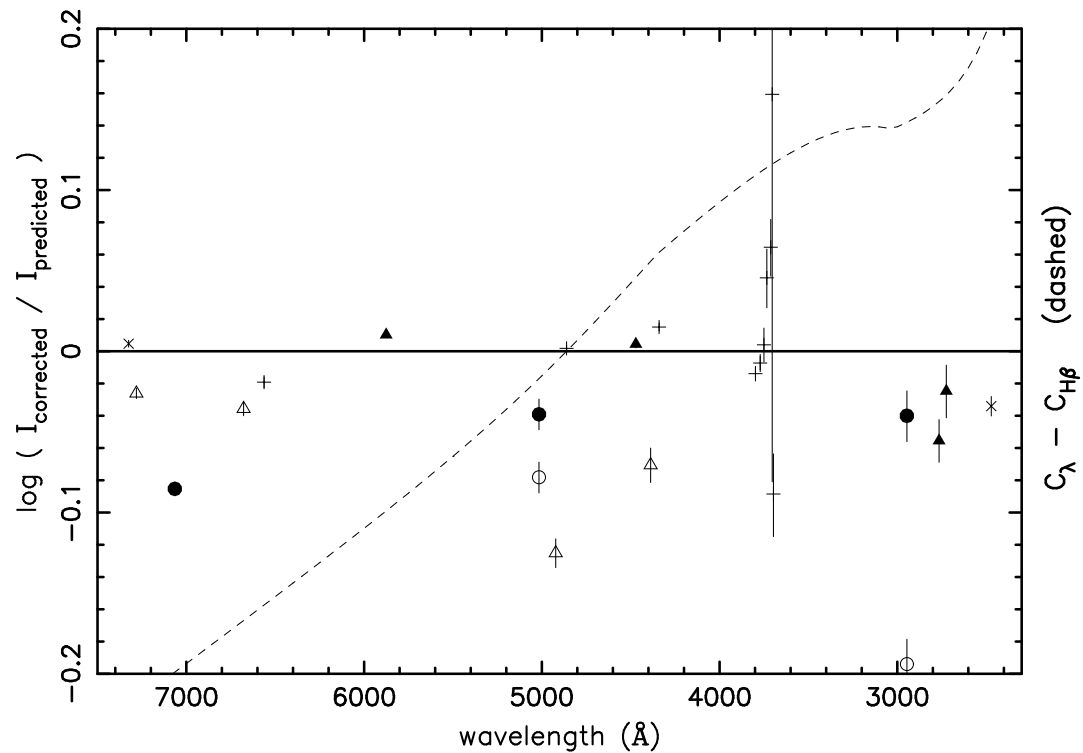


Figure 4.7 Like Fig. 4.6, but for STIS-SLIT1c and a different scale. The two He I lines most affected by radiative transfer ($\lambda\lambda 7065$ and 2945) are not included in the fit, but are plotted relative to case B values (\circ) and model M predictions (\bullet). For case B, $\lambda 7065$ has $\log(I_{corrected}/I_{predicted}) = 0.4$. Similarly shown is singlet $\lambda 5016$ which was also not included in the fit.

lines from the series $3^3S - n^3P$ (all lines), $2^3P - n^3S$ ($\lambda\lambda 7065, 4713, 4121$) and $2^1P - n^1S$ ($\lambda 5016$) should be excluded – again pending correction for radiative transfer effects.

4.2.7 He⁺/H⁺ ratio

In fitting the H I and He I lines simultaneously, we are also able to calculate the He⁺/H⁺ abundance directly from the parameterization used in the fitting (see § 3.1). These abundances are included at the bottom of Tables 4.2 and 4.6. Table 4.2 also shows the abundances from the original reference (when published). Our new analysis agrees with these within the errors. Our confidence intervals reflect implicitly the consistency of the extinction correction as well as the match to theory and observational errors and so are somewhat larger.

The He⁺/H⁺ ratio could in principle vary with position in the nebula if the ionization structure (hence the ionization correction factor, ICF, used to convert He⁺/H⁺ to He/H) differs on account of nebular structure. However, this is likely to be a small effect. It is the case that the He⁺/H⁺ values for the different positions agree with one another within their errors. The unweighted mean and its standard deviation is 0.0883 ± 0.0019 . If weighted, the ratio is 0.0882 ± 0.0004 . Neither accounts for any systematic error.

Extensive discussion of the ICF required to determine the atomic He/H ratio would take us beyond the scope of this chapter. However, our CLOUDY model M gives 1.14 and model K gives 1.00, which are within the range given by other authors; 1.1 is a typical value with an uncertainty of roughly ± 0.05 . Adopting this we obtain $\text{He}/\text{H} = 0.097 \pm 0.002 \pm 0.005$. The latter uncertainty from the ICF is probably the major source of uncertainty, greater than that in measuring the ionic abundance.

4.3 Summary

Using slight modifications to the valuable stellar extinction curve developed by CCM89, we have been able to develop an accurate new analytic method of determining the nebular extinction curve over an extensive wavelength range in the Orion Nebula. This curve has been rigorously tested with currently available near-IR, optical, and ultraviolet ground-based and space-based data, standing up as a robust measure of the extinction. We have also compared this new curve with the CP70 nebular extinction curve. We have confirmed that the discrepancy, with respect to theoretical expectations, in some near-IR and near-UV He I lines measured by EPG04 is a result of inaccurate extinction correction, but that the UV discrepancy in observations by OTV92 is a result of calibration and/or measurement uncertainty and not an extinction (or radiative transfer) effect.

On the foundation of this new extinction analysis, we have measured systematic anomalous

He I decrements, compared to case B, associated with the $2\ ^3S - n\ ^3P$, $2\ ^3P - n\ ^3S$ and $3\ ^3S - n\ ^3P$ series, and to a lesser extent with the $2\ ^1S - n\ ^1P$ series, none of which can be explained by any adjustment to the extinction curve. Qualitatively, these anomalies are as expected from radiative transfer effects, for the triplets arising from the metastability of $2\ ^3S$ (Osterbrock, 1989). Furthermore, modeling of the radiative transfer effects using CLOUDY produces a remarkable quantitative agreement between theory and observation.

Because He I case B recombination theory is not reliable for a subset of He I permitted lines associated with these aforementioned series, those lines most affected ($\lambda 3889$, $\lambda 3188$, $\lambda 2945$, $\lambda 2829$, $\lambda 7065$, $\lambda 4713$, $\lambda 4121$, $\lambda 5016$ and those of the triplet series $3\ ^3S - n\ ^3P$) must be excluded in the determination of the amplitude of the extinction curve, or in the calculation of He^+/H^+ abundance. Alternatively, they could be included after adjustment from their case B predictions by modeling radiative transfer effects.

Chapter 5

O II ground configuration energy levels

In this chapter we determine the four energies that describe the separation of the five ground configuration energy levels of O II shown in Figure 5.1 through analysis of observations of the visible forbidden transitions. Being forbidden transitions, these are weak and not accessible in the laboratory. The ground configuration levels can be determined from laboratory data on permitted ultraviolet transitions from higher states, but in practice the uncertainties in the derived energy levels are larger than those obtained from the nebular visible transitions. Thus, the published compilations of data on these energy levels (Eriksson, 1987; Martin et al., 1993) rely heavily on the pioneering work of Bowen (1960) and de Robertis et al. (1985) on planetary nebulae (see Table 5.1). Our analysis of new data improves on these energies and provides a discussion of the uncertainties.

Bowen (1960) observed the two blue [O II] lines in seven bright planetary nebulae (a total of 16 photographic plates) and the four red [O II] lines (blended into two lines) in one nebula

Table 5.1. O II ground configuration energy levels (cm^{-1})

Designation	Bowen (1955)	De Robertis et al. (1985)	Level Difference	Eriksson (1987)	Martin et al. (1993)	This Work	Level Difference
$^4\text{S}_{3/2}$	0.0	0.0	26810.5	0.00	0.00	0.00	$26810.77 \pm 0.03 \pm 0.03$
$^2\text{D}_{5/2}$	26810.7	26810.5	20.1 ± 0.1	26810.52	26810.55	$26810.77 \pm 0.03 \pm 0.03$	$19.80 \pm 0.01 \pm 0.00$
$^2\text{D}_{3/2}$	26830.5	26830.6	13637.5	26830.57	26830.57	$26830.57 \pm 0.01 \pm 0.03$	$13637.34 \pm 0.01 \pm 0.03$
$^2\text{P}_{3/2}$	40468.3	40468.1	2.00 ± 0.03	40467.69	40468.01	$40467.91 \pm 0.02 \pm 0.05$	$2.02 \pm 0.01 \pm 0.01$
$^2\text{P}_{1/2}$		40470.1		40469.69	40470.00	$40469.93 \pm 0.02 \pm 0.05$	

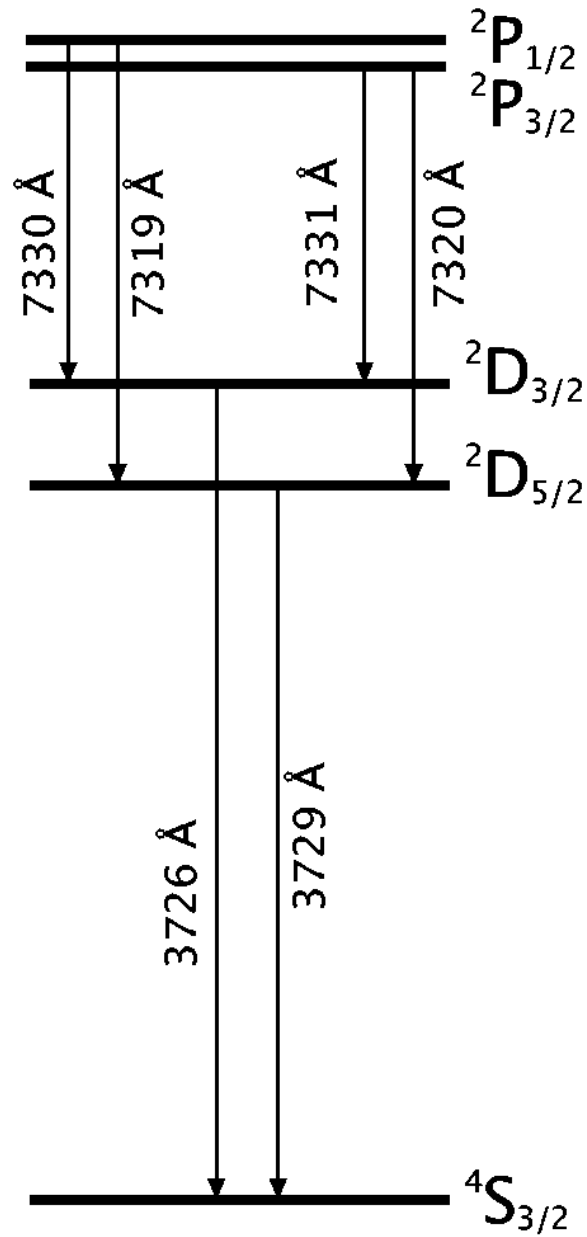


Figure 5.1 Grotrian diagram of O II ground configuration energy level transitions (not to scale). Wavelengths are approximate air values.

(three separate plates). The O^+ gas of the planetary nebulae was assumed to have an average bulk velocity identical to the measured velocity of the H^+ gas (the H^+ energy levels being well known). The observed [O II] wavelengths adjusted to this velocity give absolute wavenumbers for the energy level differences for the transitions. These early data resolved the 2D term into its two J components, but were not able to determine the splitting of the 2P term. The latter splitting was determined in de Robertis et al. (1985) using high-resolution digital spectra of the four red lines in one bright planetary nebula (NGC 7027). As can be appreciated from Figure 5.1, the red transitions ending on a common lower level constrain the splitting of the 2P term while the transitions from a common upper level constrain the splitting of the 2D term, independently of the blue data. De Robertis et al. (1985) found a value for the latter splitting somewhat different than that found by Bowen. Since absolute velocities or wavenumbers were not measured, de Robertis et al. (1985) calculated the 2D - 2P separation by assuming that the $\lambda 7319/\lambda 7320$ line blend measured by Bowen (1960) was actually a measure of the stronger $\lambda 7320$ line and that Bowen (1960)'s roughly symmetric $\lambda 7330/\lambda 7331$ blend was a measure of this line pair's average.

We show that H II regions can also be used to determine the energy levels of O II. With high-resolution echelle spectroscopy of the Orion Nebula (resolving all red and blue lines), we are able to measure not only the splitting of both the 2P and 2D terms but also the separation between these two split terms. The observations are described in § 5.2, and the full analysis, including uncertainties is described in § 5.3. But first we update Bowen's (1960) work by analysis of more recent digital data on 23 planetary nebulae (§ 5.1). This provides important insight into the method of analysis of the full Orion data and also provides improved values of the two energies constrained by the blue lines à la Bowen.

We conclude by comparing our results with recent work by Sharpee et al. (2004).

5.1 Bowen revisited

Using a coude spectrograph on the Hale telescope, Bowen (1955) observed the blue spectra of seven planetary nebulae photographically. Since the introduction of the Hamilton Echelle Spectrograph on the 3-m Shane telescope at the Lick Observatory in 1987 (Vogt, 1987), high-resolution spectra of (at least) 24 planetary nebulae spectra have been published, the relevant data for our purposes being the line lists with accurately tabulated wavelengths. (One nebula, NGC 6818, had to be discarded because of a grossly discrepant wavelength – we suspect a typographical error.) These new spectra resolve the blue lines, but due to internal nebular motions, the red pairs of lines are not resolved.

Following Bowen (1955), we therefore have two lines to constrain two energies. But there is

an important additional requirement: we need to know the velocity of the line-producing gas, and any uncertainty (δv_{O^+}) will have predictable consequences. For example, if one uses the $\lambda 3729$ line to find the energy difference for this transition, $E_{4S_{3/2}-2D_{5/2}}$ (note the convention of an “upward” transition), because of this degeneracy the Doppler effect gives an *uncertainty*

$$\delta E_{4S_{3/2}-2D_{5/2}} = 0.0895\delta v_{O^+}, \quad (5.1)$$

where throughout this chapter energies are in units of cm^{-1} and velocities in units of km s^{-1} . Looking ahead to the red data,

$$\delta E_{2D_{3/2}-2P_{3/2}} = 0.0455\delta v_{O^+} = 0.50865\delta E_{4S_{3/2}-2D_{5/2}}, \quad (5.2)$$

but note that the smaller splittings $E_{2D_{5/2}-2D_{3/2}}$ and $E_{2P_{3/2}-2P_{1/2}}$ are much less susceptible to any uncertainty in the velocity.

In Bowen’s work (1955), permitted lines of H^+ and He^+ gas set the rest-frame velocity, and similarly here all wavelengths for all 23 planetary nebulae are first put into such a reference frame with H^+ at rest. As tabulated by the authors, the planetary nebulae wavelengths have in fact already been corrected for the previously known systemic velocity of the whole nebula, but nevertheless we find from the data that the H^+ is apparently not quite at rest. This is either because the systemic velocity used was only approximate, or because for the slit positions observed, the mean velocity of the H^+ gas is not identical to that averaged over the nebula, which would not be surprising given incomplete coverage of an expanding nebula. To define the H^+ frame for each nebula, we used the eight or nine unblended H I lines (H16–H δ) near the blue [O II] lines, these all being contained in the same echelle spectrum. The corresponding blue wavelengths are given in Table 5.2.

The measured velocity of O^+ is not necessarily the same as that of H^+ because of the ionization structure and expansion that exist in the nebula and the fact that the slit does not usually cover the entire nebula. Bowen’s approach (1955) was to average results over several nebulae, since on average the two velocities should be equal. Given data on 23 nebulae, we can improve on this iteratively as explained below.

Our analysis involves developing a parameterized model and then optimizing the parameters by non-linear least squares to match predicted wavelengths, in air, with the wavelengths tabulated. The parameters of the model are the energies and any velocity offsets (v_{O^+}) deemed necessary. (Toward this end, deviations of observed wavelengths from the model predictions are expressed in terms of velocity.) The energies can be taken as the successive energy differences, four independent values in the full model, or simply the energies of the four upper levels. Even with the first of these two options there is covariance in the resulting solution, since four of the six energy transitions (corresponding to four of the six available wavelengths) couple the

Table 5.2. Determination of ${}^2D_{5/2}$ energy from planetary nebulae data

Nebula	${}^4S_{3/2}$ - ${}^2D_{3/2}$ (Å)	${}^4S_{3/2}$ - ${}^2D_{5/2}$ (Å)	Weight	Reference
NGC 2440	3726.00	3728.69	0.25	Hyung & Aller (1998)
NGC 6543	3726.06	3728.81	1.0	Hyung et al. (2000)
NGC 6567	3726.25	3728.97	0.5	Hyung et al. (1993)
NGC 6572	3726.01	3728.76	1.0	Hyung et al. (1994b)
NGC 6741	3726.15	3728.90	1.0	Hyung & Aller (1997a)
NGC 6790	3726.00	3728.74	1.0	Aller et al. (1996)
NGC 6818	3726.32	3728.79	0.0	Hyung et al. (1999b)
NGC 6884	3726.02	3728.80	0.5	Hyung et al. (1997)
NGC 6886	3726.05	3728.78	1.0	Hyung et al. (1995)
NGC 7009major	3725.97	3728.71	1.0	Hyung & Aller (1995b)
NGC 7009minor	3726.14	3728.95	0.25	Hyung & Aller (1995a)
NGC 7662	3725.94	3728.69	1.0	Hyung & Aller (1997b)
IC 351	3726.04	3728.81	1.0	Feibelman et al. (1996)
IC 418	3726.04	3728.80	1.0	Hyung et al. (1994a)
IC 2149	3725.99	3728.76	1.0	Feibelman et al. (1994)
IC 2165	3726.18	3728.96	0.5	Hyung (1994)
IC 4634	3726.27	3729.02	1.0	Hyung et al. (1999a)
IC 4846	3726.17	3728.93	1.0	Hyung et al. (2001c)
IC 4997	3725.97	3728.71	1.0	Hyung et al. (1994c)
IC 5117	3726.03	3728.75	0.5	Hyung et al. (2001a)
IC 5217	3726.04	3728.77	1.0	Hyung et al. (2001b)
BD +30 3639	3726.01	3728.77	1.0	Aller & Hyung (1995)
Hubble 12	3726.04	3728.80	1.0	Hyung & Aller (1996)
Hu 1-2	3726.07	3728.83	1.0	Pottasch et al. (2003)

independent successive energy differences. The “model uncertainties” from the goodness of fit to the model are the 68.3% confidence intervals for one-dimensional marginal distributions for each of the parameters.

Let us return to the blue lines, for which we have 46 measured wavelengths for 23 planetary nebulae. As energy parameters, we used $E_{4S_{3/2}-2D_{5/2}}$ and $E_{2D_{5/2}-2D_{3/2}}$. In the initial model we went to the extreme of introducing 23 velocity offsets. This precludes determining $E_{4S_{3/2}-2D_{5/2}}$, and we find $E_{2D_{5/2}-2D_{3/2}} = 19.79 \pm 0.05$. For each nebula the two velocity residuals (from the two wavelength residuals) are of equal magnitude (denoted σ_{int}) with opposite signs, indicating that relative to the model the two lines are too close together or too widely separated. Overall the rms velocity residual was 0.96 km s^{-1} . Those nebulae with considerably larger rms values can be judged to have data of lower quality; i.e., even with the luxury of the maximal number of parameters, the data are still not going to be well matched by the model. Two nebulae with residuals greater than 2.4 km s^{-1} have been assigned weight 0.25 (in the calculation of χ^2), while another four with residuals greater than 1.2 km s^{-1} have been assigned weight 0.5. No bias is introduced in subsequent calculations of the splitting $E_{2D_{5/2}-2D_{3/2}}$ since equal numbers of “too close” and “too separated” cases are involved; now $E_{2D_{5/2}-2D_{3/2}} = 19.79 \pm 0.04$. The weighted rms residual is 0.71 km s^{-1} and no subsequent model, with fewer parameters, can improve on this.

The next model goes to the other extreme, fitting only the two energy differences, finding $E_{4S_{3/2}-2D_{5/2}} = 26810.68 \pm 0.13$ and $E_{2D_{5/2}-2D_{3/2}} = 19.79 \pm 0.18$. The latter energy difference is still close to that in the initial model, but is determined with less confidence because the two-parameter model fits the data less well. The rms velocity residual is 6.7 km s^{-1} , much larger than suggested by our assessment of the data quality, and so clearly indicating a less than optimal model.

Thus our goal was to improve the model iteratively by adding a minimal number of parameters v_{O+} , for a subset of the nebulae, expecting a significant reduction in χ^2 per degree of freedom. We identified seven nebulae for which the residuals exceeded 6.7 km s^{-1} and also $3\sigma_{int} < 6.7 \text{ km s}^{-1}$ and for these included a velocity offset parameter. This produced a markedly improved model with an rms residual of 1.9 km s^{-1} and $E_{4S_{3/2}-2D_{5/2}} = 26810.77 \pm 0.04$ and $E_{2D_{5/2}-2D_{3/2}} = 19.79 \pm 0.06$. Repeating this process with the new rms identifies eight more nebulae that would benefit from velocity offsets, for a total of 15 of the 23 nebulae. This iteration reduces the rms velocity residual to 0.82 km s^{-1} ; this is now comparable to the above estimate of the quality of the data, indicating that adding further parameters would not be justified; $E_{4S_{3/2}-2D_{5/2}} = 26810.77 \pm 0.03$ and $E_{2D_{5/2}-2D_{3/2}} = 19.79 \pm 0.03$ – the only difference with respect to the previous iteration being a lowering of the error (confidence interval). It is important to acknowledge that there is a systematic error in $E_{4S_{3/2}-2D_{5/2}}$ of order 0.03

Table 5.3. Best-fit line parameters for visible wavelength transitions

Transition	Position	Measured Wavelength (\AA)	FWHM (km s^{-1})	Reddening corrected line strength ($10^{-13} \text{ erg s}^{-1} \text{ cm}^{-2}$)
$^4\text{S}_{3/2} - ^2\text{D}_{3/2}$	1SW	3726.072 ± 0.001	16.8 ± 0.2	426 ± 6
	x2	3726.078 ± 0.001	18.0 ± 0.3	273 ± 4
	37W	3726.060 ± 0.002	15.3 ± 0.3	466 ± 9
$^4\text{S}_{3/2} - ^2\text{D}_{5/2}$	1SW	3728.824 ± 0.001	17.3 ± 0.2	188 ± 2
	x2	3728.829 ± 0.002	19.1 ± 0.2	138 ± 2
	37W	3728.811 ± 0.002	15.7 ± 0.3	213 ± 4
$^2\text{D}_{5/2} - ^2\text{P}_{1/2}$	1SW	7319.173 ± 0.006	18.0 ± 0.6	14.7 ± 0.5
	x2	7319.178 ± 0.008	21.3 ± 0.8	6.9 ± 0.2
	37W	7319.099 ± 0.011	16.9 ± 1.1	10.8 ± 0.6
$^2\text{D}_{5/2} - ^2\text{P}_{3/2}$	1SW	7320.253 ± 0.002	17.5 ± 0.2	42.6 ± 0.5
	x2	7320.250 ± 0.003	19.3 ± 0.3	17.1 ± 0.2
	37W	7320.181 ± 0.004	16.9 ± 0.4	32.0 ± 0.6
$^2\text{D}_{3/2} - ^2\text{P}_{1/2}$	1SW	7329.787 ± 0.004	17.9 ± 0.4	21.1 ± 0.4
	x2	7329.798 ± 0.006	23.4 ± 0.6	8.6 ± 0.2
	37W	7329.725 ± 0.005	16.0 ± 0.5	16.6 ± 0.4
$^2\text{D}_{3/2} - ^2\text{P}_{3/2}$	1SW	7330.886 ± 0.003	18.1 ± 0.3	24.0 ± 0.4
	x2	7330.885 ± 0.004	19.8 ± 0.4	9.5 ± 0.2
	37W	7330.818 ± 0.005	17.7 ± 0.5	18.2 ± 0.5

cm^{-1} because the introduction of parameters v_{O^+} , while hopefully unbiased, is still subjective. Such systematic errors are recorded separately in Table 5.1 to distinguish them from confidence intervals.

The energies determined are close to those given by Bowen, but significantly different than those derived by de Robertis et al. (1985) – refer to our Table 5.1.

5.2 Observations of the Orion Nebula

All six [O II] forbidden lines are seen (with good signal-to-noise ratios) in the CTIO echelle spectra data (37W, 1SW and x2, see Chapters 2 and 7). Data for 1SW are shown in Figure 5.2. The pairs of [O II] red lines were slightly blended and so were analysed using a double Gaussian fit. The results of our line fitting are summarized in Table 5.3. All line profiles are similar as seen in the matching FWHM and directly from the spectra in Figure 5.2.

For the common upper level line pairs $\lambda 7320/\lambda 7331$ and $\lambda 7319/\lambda 7330$ the line strength ratios can be predicted directly from the transition probabilities (Zeippen, 1987; Wiese et al., 1996), offering an independent check of one aspect of the fits. Results are presented in Table 5.4. There is reasonable agreement between the theory and the observations. The sole anomaly, seen

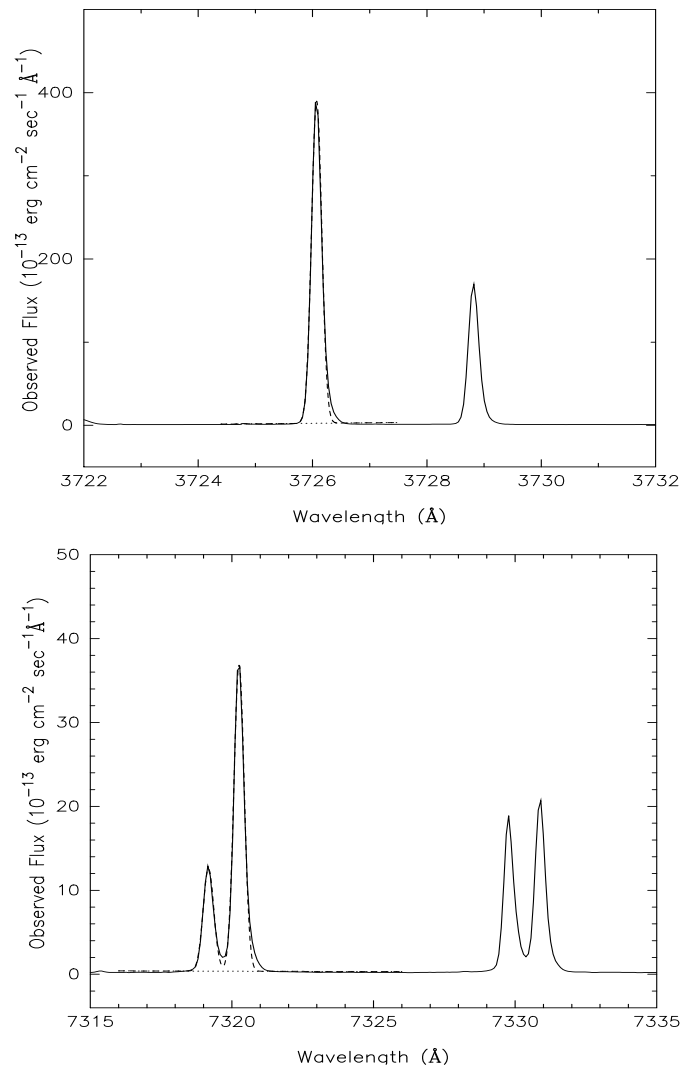


Figure 5.2 Gaussian profile fit of three of the six visible O II lines (1SW). The dark solid line represents the observed line profile, and the lighter dashed line represents the Gaussian fit. The wavelength has been adjusted to the rest-frame velocity of the H^+ gas. Refer to Table 5.3 for reddening-corrected fluxes and the results of the line fitting.

in the $\lambda 7319/\lambda 7330$ ratio in the x2 line of sight, arises because of a velocity-shifted component from a photoionized Herbig-Haro shock (Chapter 7) which has 2%-4% of the nebular [O II] flux. The nebular $\lambda 7330$ and $\lambda 7319$ lines are contaminated by the velocity-shifted components of $\lambda 7331$ and $\lambda 7320$, respectively. A higher relative contamination from the stronger of these two lines, $\lambda 7320$, results in a higher $\lambda 7319/\lambda 7330$ ratio.

All four [O II] red lines are found in the same echelle order of a single exposure, unlike in the data of de Robertis et al. (1985), where the $\lambda 7319/\lambda 7320$ and $\lambda 7330/\lambda 7331$ line pairs were obtained in two separate spectra. Measuring the 2P energy splitting $E_{2P_{3/2}-2P_{1/2}}$ depends on the wavelength difference *within* each of the line pairs, and so the results in de Robertis et al. (1985) should be accurate. On the other hand, the splitting of the 2D term $E_{2D_{5/2}-2D_{3/2}}$ depends on the wavelength difference *between* the pairs, and so our single spectrum containing both line pairs, with only a single wavelength calibration in the same echelle order, should yield a more accurate result.

All lines produced by the same ionized species should have the same velocity. However, using the current published energy levels and derived rest wavelengths in air (Eriksson, 1987; Martin et al., 1993) together with our observed wavelengths, we obtain O^+ velocities that are grossly inconsistent, well beyond the uncertainties propagated from the measurement errors of the observed wavelengths (see Table 5.5). In particular, there is no explanation why lines in the same wavelength region and originating from a common upper level ($^2P_{1/2}$ or $^2P_{3/2}$) should yield significantly different velocities, as is observed to be the case in columns (7) and (8) of Table 5.5; at the very least, there is a problem with the splitting $E_{2D_{5/2}-2D_{3/2}}$. The consistency of the data for the three lines of sights, and the lack of agreement of the velocities from all of the lines, points to inaccurate [O II] rest wavelengths arising from poorly determined ground configuration energy levels, including the separations $E_{4S_{3/2}-2D_{5/2}}$ and $E_{2D_{3/2}-2P_{3/2}}$. This was the original motivation for the work discussed in this chapter.

5.3 Constraining the energy levels with the Orion Nebula data

With a set of six accurate wavelengths, for each of three lines-of-sight (1SW, x2, and 37W), it is possible to obtain the energies of the four excited levels in the ground configuration of O II (Fig. 5.1); the problem is over-constrained. However, as encountered in the analysis of planetary nebula spectra in § 5.1, there is the possibility of an unknown velocity offset of the O^+ gas for each position observed. But even with an extra velocity offset parameter v_{O^+} for each position, the problem is still over-constrained (even for a single position) and thus amenable to modeling and least-squares optimization.

As with the planetary nebulae, there is a Doppler-related degeneracy to be resolved as well,

Table 5.4. Comparison between observed and predicted line ratios as determined from transition probabilities, A_{ij}

Transition	1SW		x2		37W		Zeippen ^a		Wiese et al. ^b	
	Flux	Ratio	Flux	Ratio	Flux	Ratio	A_{ij}	Ratio	A_{ij}	Ratio
$^2D_{5/2}-^2P_{1/2}$ ($\lambda 7319$)	14.7 ± 0.5	0.70 ± 0.03	6.9 ± 0.2	0.80 ± 0.03	10.8 ± 0.6	0.65 ± 0.04	0.0563	0.598	0.0519 ± 0.0052	0.599 ± 0.085
$^2D_{3/2}-^2P_{1/2}$ ($\lambda 7330$)	21.1 ± 0.4		8.6 ± 0.2		16.6 ± 0.4		0.0941		0.0867 ± 0.0087	
$^2D_{5/2}-^2P_{3/2}$ ($\lambda 7320$)	42.6 ± 0.5	1.77 ± 0.04	17.1 ± 0.2	1.80 ± 0.04	32.0 ± 0.6	1.76 ± 0.06	0.1067	1.84	0.0991 ± 0.0099	1.86 ± 0.26
$^2D_{3/2}-^2P_{3/2}$ ($\lambda 7331$)	24.0 ± 0.4		9.5 ± 0.2		18.2 ± 0.5		0.0580		0.0534 ± 0.0053	

^aZeippen (1987).

^bWiese et al. (1996).

Table 5.5. Line velocities in Orion using recent wavelength tabulations

Transition	Air λ (\AA)			Position	Observed λ (\AA)	Velocity ^d (km s^{-1})		
	Martin ^a	Eriksson ^b	This work ^c			Martin	Eriksson	This work
$^4\text{S}_{3/2}-^2\text{D}_{3/2}$	3726.032	3726.032	3726.032	1SW	3726.072	3.2 ± 0.1	3.2 ± 0.1	3.2 ± 0.1
			± 0.001	x2	3726.078	3.7 ± 0.1	3.7 ± 0.1	3.7 ± 0.1
			± 0.004	37W	3726.060	2.3 ± 0.2	2.3 ± 0.2	2.3 ± 0.2
$^4\text{S}_{3/2}-^2\text{D}_{5/2}$	3728.815	3728.819	3728.784	1SW	3728.824	0.7 ± 0.1	0.4 ± 0.1	3.2 ± 0.1
			± 0.004	x2	3728.829	1.1 ± 0.2	0.8 ± 0.2	3.6 ± 0.2
			± 0.004	37W	3728.811	-0.3 ± 0.2	-0.6 ± 0.2	2.2 ± 0.2
$^2\text{D}_{5/2}-^2\text{P}_{1/2}$	7318.92	7319.07	7319.073	1SW	7319.173	10.4 ± 0.2	4.2 ± 0.2	4.1 ± 0.2
			± 0.009	x2	7319.178	10.6 ± 0.3	4.4 ± 0.3	4.3 ± 0.3
			± 0.012	37W	7319.099	7.3 ± 0.5	1.2 ± 0.5	1.1 ± 0.5
$^2\text{D}_{5/2}-^2\text{P}_{3/2}$	7319.99	7320.14	7320.157	1SW	7320.253	10.8 ± 0.1	4.6 ± 0.1	3.9 ± 0.1
			± 0.009	x2	7320.250	10.6 ± 0.1	4.5 ± 0.1	3.8 ± 0.1
			± 0.012	37W	7320.181	7.8 ± 0.2	1.7 ± 0.2	1.0 ± 0.2
$^2\text{D}_{3/2}-^2\text{P}_{1/2}$	7329.67	7329.83	7329.699	1SW	7329.787	4.8 ± 0.1	-1.8 ± 0.1	3.6 ± 0.1
			± 0.005	x2	7329.798	5.2 ± 0.2	-1.3 ± 0.2	4.0 ± 0.2
			± 0.012	37W	7329.725	2.2 ± 0.2	-4.3 ± 0.2	1.1 ± 0.2
$^2\text{D}_{3/2}-^2\text{P}_{3/2}$	7330.73	7330.91	7330.786	1SW	7330.886	6.4 ± 0.1	-1.0 ± 0.1	4.1 ± 0.1
			± 0.005	x2	7330.885	6.3 ± 0.2	-1.0 ± 0.2	4.0 ± 0.2
			± 0.012	37W	7330.818	3.6 ± 0.2	-3.8 ± 0.2	1.3 ± 0.2

^aMartin et al. (1993)^bEriksson (1987)^cuncertainties are model-fitting and systematic, respectively, from energy level differences (see Table 5.1)^duncertainties are simply from the least-squares Gaussian fit for each line.

through independent constraints on v_{O^+} . We show how this is possible in Orion, it not being sufficient to assume that on average, over many positions, the velocities of the O^+ gas and H^+ gas are identical (in which case $\langle v_{O^+} \rangle = 0$).

The Orion Nebula can be represented by a blister model where gas is accelerating toward the ionizing star and the observer away from the background molecular cloud (Balick et al., 1974). Because of ionization stratification in this accelerating flow, the velocity is correlated with the ionization potential (IP): gas that is more highly ionized is more blue shifted (has more negative velocity). This is observed; see, e.g., Baldwin et al. (2000). Figure 5.3, plotting velocity against the emitting species' IP, summarizes this effect for our observations of many lines of many different ions for the three lines of sight. Models of the nebula (Baldwin et al., 2000) show that the O^+ zone is relatively narrow (see their Figure 4) and so there should be a well defined velocity. From the trend seen in Figure 5.3, the expected value for v_{O^+} , at IP 35 eV for O^+ lies between 0 and 5 km s^{-1} , set in part by the [S III] (IP = 34.79 eV) velocities at similar ionization potential. Plotting the results in columns (7) and (8) of Table 5.5 in Figure 5.3 would clearly reveal their discrepancy, again pointing to a problem with the energy levels. The velocities from our new O^+ model clearly satisfy the general constraint set by the surrounding lines.

As in the analysis of the planetary nebula data, our examination of the Orion Nebula data is rooted in a model of the energy levels, used to predict the air wavelengths. In this case we set $E_{4S_{3/2}-2D_{5/2}} = 26810.77$, the result already found in § 5.1. The remaining analysis is then a non-linear least squares fit (unweighted), using six parameters in the model: the other three energy differences, and the three velocities v_{O^+} . This model produces rms energy-difference residuals of only 0.4 km s^{-1} . Line by line and position by position, this model gives the velocities listed in column (9) of Table 5.5; these are clearly now quite consistent with one another.

This choice of $E_{4S_{3/2}-2D_{5/2}}$ produces v_{O^+} equal to 4.0 ± 0.3 , 4.1 ± 0.3 , and 1.4 ± 0.3 km s^{-1} for 1SW, x2, and 37W, respectively (because of changes in geometry from one line of sight to the next, these velocities need not be identical). It turns out that these fall in line with the trend in Figure 5.3, and so no optimization was carried out on this energy difference.

Recall, however, that if a slight change were made in this energy, v_{O^+} would respond according to equation 5.1. Thus, the model uncertainty $\delta E_{4S_{3/2}-2D_{5/2}}$ from the planetary nebula analysis, ± 0.03 cm^{-1} , results in $\delta v_{O^+} = 0.34$ km s^{-1} . This is of the same order as the model-fitting uncertainties for the Orion data. In principle, one might start by determining v_{O^+} and its uncertainty from interpolation in Figure 5.3 and work backwards to $E_{4S_{3/2}-2D_{5/2}}$ and its uncertainty. Given the consistency, we adopt the tighter constraint found independently in § 5.1. This will propagate as a systematic uncertainty through to the other energies (see equation 5.2).

Uncertainties in v_{O^+} have the same effect as uncertainties in the wavelength calibration,

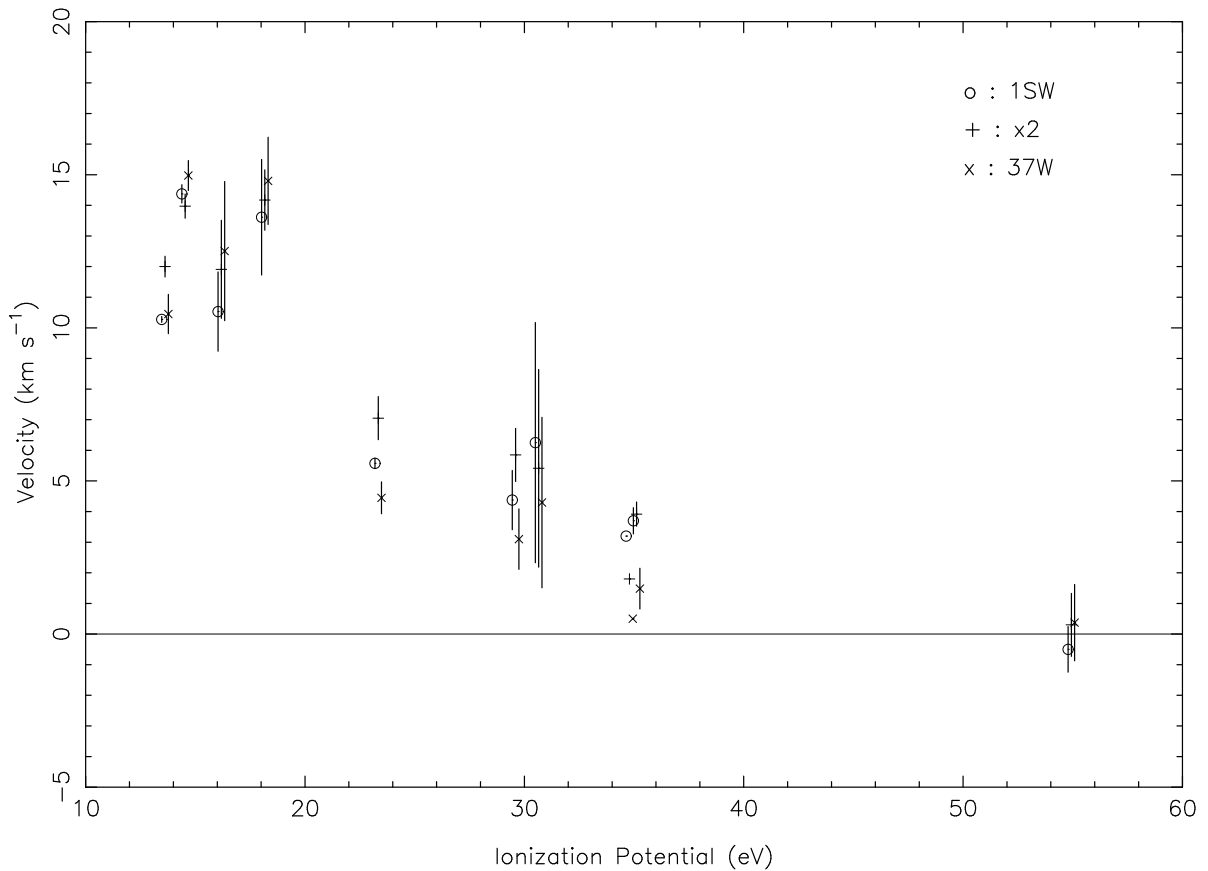


Figure 5.3 Gas velocity (relative to H I lines – i.e., H⁺ gas) as a function of the emitting species' ionization potential. The three lines of sight have been offset in the x direction to properly show the standard deviations about the mean velocities for each line of sight. The ionization potentials of O⁰ and O⁺⁺ are 13.6181 and 54.934 eV, respectively. O⁺ ionization potential is 35 eV.

which we deduce is accurate to 0.5 km s^{-1} , consistent with the scatter of individual blue H^+ line velocities about the mean. Thus, for the remainder of the Orion analysis, we adopt $\delta v_{\text{O}^+} = 0.5 \text{ km s}^{-1}$, noting that this subsumes errors in the wavelength calibration of the blue lines. For the red lines, there is an additional systematic error of order 0.15 km s^{-1} relating to the alignment of the separate red and blue echelle spectra into the same velocity/wavelength system. The next issue is the accuracy of the wavelength calibration for individual lines. To assess this, we note that there are numerous lines that are duplicated in neighbouring echelle orders of the same spectrum. By comparing the duplicate measurements of these lines' wavelengths, we find a residual characteristic order-to-order difference of 0.65 km s^{-1} , independent of measurement uncertainty. In practice, we feel that measurements of the red [O II] lines, which all appear in the centre of an order, have a systematic uncertainty of less than half this, $\sim 0.3 \text{ km s}^{-1}$. Taken all together, the combined systematic error is of order 0.7 km s^{-1} , which corresponds to $\delta E_{2D_{3/2-2}P_{3/2}} = 0.03$. Therefore, the separation $E_{2D_{3/2-2}P_{3/2}}$ is properly quoted as $13637.34 \pm 0.01 \pm 0.03$. This is significantly different from what has been previously adopted (see Table 5.1).

On the other hand, for the small splittings, the systematic effects are tiny compared to the model uncertainties, and so are listed below as 0.00. As anticipated, we find that the value of the splitting $E_{2P_{3/2-2}P_{1/2}}$ of the ^2P term, $2.02 \pm 0.01 \pm 0.00$, is in close agreement with that found by de Robertis et al. (1985), 2.00 ± 0.03 (largely adopted by Eriksson, 1987; Martin et al., 1993).

The splitting $E_{2D_{5/2-2}D_{3/2}}$ of the ^2D term is $19.80 \pm 0.01 \pm 0.00$, closely consistent with the value $19.79 \pm 0.03 \pm 0.03$ obtained in § 5.1 from only the blue lines of planetary nebulae. We conclude that the splitting of the ^2D term should be revised from the value 20.1 ± 0.1 found by de Robertis et al. (1985) and (largely) adopted by Eriksson (1987) and Martin et al. (1993).

These energy differences allow us to calculate the energies of all four energy levels (see Table 5.1). The model was rewritten with these energies as the parameters in order to track the effects of covariant changes in this non-linear model of the air wavelengths and thus provide the appropriate one-dimensional marginal confidence intervals reported in Table 5.1. The errors reported are again the model-fitting uncertainty and the systematic error. The latter reflects the propagation of the error in $E_{4S_{3/2-2}D_{5/2}}$ plus the systematic error in $E_{2D_{3/2-2}P_{3/2}}$ for the highest two energies

These energy levels allow for the calculation of the air wavelengths of lines in the UV in addition to those in Table 5.5. From $E_{4S_{3/2-2}P_{3/2}}$ and $E_{4S_{3/2-2}P_{1/2}}$, we calculate $\lambda 2470.347 \pm 0.001 \pm 0.003$ and $\lambda 2470.223 \pm 0.001 \pm 0.003$, respectively.

Because of the presence of systematic errors, the above analysis was carried out with equal weights for all lines. However, we have repeated the analysis using a weighted fit based on the uncertainties found in measuring each line; $E_{2D_{5/2-2}D_{3/2}}$ increased by only 0.001, $E_{2D_{3/2-2}P_{3/2}}$

decreased by 0.015 (well within the systematic uncertainty), and $E_{2P_{3/2}-2P_{1/2}}$ increased by 0.007 (recorded in Table 5.1 as 0.01 systematic uncertainty).

5.4 Comparison to recent work of Sharpee et al.

Sharpee et al. (2004) have observed the four red lines ($\lambda\lambda 7319, 7320, 7330,$ and 7331) in sky spectra using the High-Resolution Echelle Spectrograph (HIRES) on Keck I. In their determination of the O II $2p^3$ energy levels, they also make use of data sets from nebulae (Bowen, 1960; de Robertis et al., 1985; Baldwin et al., 2000; Sharpee et al., 2003). The nebular data are given lesser weights (0.018, 0.16, 1.00, and 1.00, respectively) than the HIRES data set (10.00). Velocity corrections for data sets of three nebulae (de Robertis et al., 1985; Baldwin et al., 2000; Sharpee et al., 2003) were found using a weighted least-squares analysis similar to that done in § 5.1; Bowen (1960) is an average of multiple nebulae and was assumed to have $\langle v_{O+} \rangle = 0$. From these five data sets, they obtain splittings of 19.810 ± 0.006 and 2.010 ± 0.005 for the 2D and 2P terms, respectively – both in excellent agreement with our results.

The $^2D_{3/2}-^2P_{3/2}$ separation, 13637.403 ± 0.004 , is quoted here with their 1σ model-fitting uncertainty. Even though for the HIRES data one knows $v_{O+} = 0$, there is still a systematic uncertainty because of the wavelength calibration that was accomplished through the OH Meinel band. From their stated “statistical scatter” of 0.5 km s^{-1} we judge that the systematic error in $E_{2D_{3/2}-2P_{3/2}}$ is no larger than 0.023 cm^{-1} (see equation 5.2), and 0.012 \AA in the wavelengths of the red lines. Based on the model-fitting uncertainties alone, our value of $13637.34 \pm 0.01 \pm 0.03$ might seem significantly different, but the values are in fact consistent when one accounts for the systematic uncertainties. If we adopted the Sharpee et al. (2004) value of $E_{2D_{3/2}-2P_{3/2}}$, the velocities in Table 5.5 would be more consistent for 37W but correspondingly less consistent for the other two positions.

To complete their set of O II $2p^3$ energy levels, the blue lines from three nebulae (Bowen, 1960; Baldwin et al., 2000; Sharpee et al., 2004) were used to deduce $E_{4S_{3/2}-2D_{5/2}} = 26810.76 \pm 0.08$ (no systematic error was estimated). This energy difference compares well with our result using 23 planetary nebulae, $26810.77 \pm 0.03 \pm 0.03$.

The UV wavelengths depend on both $E_{4S_{3/2}-2D_{5/2}}$ and $E_{2D_{3/2}-2P_{3/2}}$, and so the Sharpee et al. (2004) values $\lambda 2470.343 \pm 0.005$ and $\lambda 2470.220 \pm 0.005$ are consistent with ours, although slightly less accurate.

5.5 Conclusions

From a detailed analysis of Orion Nebula and planetary nebulae data, we find new energies for the ground configuration. Both model-fitting uncertainties and systematic uncertainties are presented. This work confirms the utility of astrophysical measurements in determining accurate energies for the O II $2p^3$ ground configuration. As a by-product, we determine a revised set of air wavelengths of the [O II] visible lines (see Table 5.5) and the UV lines (see § 5.3). As Sharpee et al. (2004) point out, there are revisions required in the standard NIST values.

Using these revised wavelengths, it is now possible to constrain the velocities of all three oxygen zones (O^0 , O^+ , and O^{++}), and in turn, the spatial and physical origin of oxygen permitted lines can be inferred (Blagrove et al., 2006b).

Chapter 6

Temperature variations from HST spectroscopy

There is a fundamental issue that continues to be problematic in the analysis of not only the Orion Nebula, but gaseous nebulae in general – the discrepancy between heavy element abundances inferred from emission lines that are collisionally excited (CELs) and abundances inferred from recombination lines (RLs). Studies of PNs contrasting recombination and collisional abundances (Liu et al., 1995; Kwitter & Henry, 1998) often find differences exceeding a factor of two. For NGC 7009, Liu et al. (1995) found that the recombination C, N, and O abundances are a factor of ~ 5 larger than the corresponding collisional abundances, which was found to be the case also for neon (Luo et al., 2001) The discrepancy is even larger, a factor of ~ 20 , for the Galactic bulge PN M 1-42 (Liu et al., 2001) and Hf 2-2, which has the most extreme abundance difference to date, a factor of 84 (Liu, 2003).

Studies of H II regions find similar behavior although the differences are generally smaller than is the case for PNs. Tsamis et al. (2003) presented observations of 5 H II regions – M 17 and NGC 3576 as well as the Magellanic Cloud H II regions 30 Doradus, LMC N11B and SMC N66. They found that the disparity was always in the same direction. For four of their objects, the O^{++}/H^+ abundance from O II RLs exceeded the corresponding value inferred from the nebular [O III] CELs by factors ranging from 1.8 – 2.7, while the factor was ~ 5 for LMC N11B. Recently, for the Orion Nebula, Esteban et al. (2004) derived a factor of 1.4 larger for O^{++}/H^+ from RLs than from CELs. According to the limited statistics, apparently H II regions exhibit less of an abundance dichotomy than some of the PNs.

Most of the efforts to explain the abundance puzzle between collisional and recombination values have attempted to do so by examining electron temperature (T_e) variations in the plasma. Because T_e is not expected to vary dramatically within the (hydrogen) ionized region of a given nebula (e.g., Harrington et al., 1982; Baldwin et al., 1991; Rubin et al., 1991), a method

developed by Peimbert (1967) has been extensively used. He developed a useful formalism by expressing the volume emissivity for a given spectral line in a Taylor series expansion around an average temperature defined such that the first order term vanishes. Since the fractional mean-square T_e variation (called t^2 , see equ. 6.7) is expected to be small, only terms to second order need be retained. The resulting influence on elemental abundance determinations began with the work of Peimbert (1967), Rubin (1969) and Peimbert & Costero (1969). There is a vast literature now that measures the discrepancy between collisional and recombination abundances in terms of t^2 .

The studies of H II regions mentioned above also derived the value of t^2 that forces the two abundance techniques to yield the same result. Tsamis et al. (2003) found for 30 Doradus a value of $t^2 \sim 0.03$. For the Orion Nebula, Esteban et al. (2004) required $t^2 = 0.022 \pm 0.002$ to reconcile the difference between abundances derived from CELs vs. RLs. For the drastically different O^{++}/H^+ abundances found for NGC 7009, Liu et al. (1995) discussed that it would be necessary to invoke $t^2 \sim 0.1$, which would then force agreement close to the higher recombination value – a value more than 3.5 times larger than the solar O/H of 4.90×10^{-4} (Allende Prieto et al., 2001). Such a large t^2 is not at all predicted by current theory/models (e.g., Kingdon & Ferland, 1998).

The current unsettled situation has led to efforts to broaden the study to include other variables besides T_e to analyse the effects upon abundance determinations. One promising avenue is to examine abundance derivation considering density variations, abundance variations, and T_e variations in combination. Liu et al. (2000) took this approach in their investigation of the PN NGC 6153 with a two-phase empirical model. Péquignot et al. (2002) continued the study using photoionization models including two components with different heavy element abundances.

HST STIS and WFPC2 observations have previously been used to study the variation of T_e in NGC 7009, as determined from the [O III] $\lambda 4363/\lambda 5007$ flux ratio (Rubin et al., 2002). Very low values for t^2 in the plane of the sky (t_A^2) were found (always ≤ 0.01). In this chapter, we focus solely on T_e variations with the purpose to determine from the observational data the magnitude of t_A^2 for the Orion Nebula.

The data used in this chapter are those of HST-STIS Slits 1, 2, 4 and 5 for V2, V52 and V72. The STIS data are reduced as in Chapter 2 and the resultant tiles are $0''.5 \times 0''.5$. The tiles overlapping the STIS fiducial bars are excluded. § 6.1 includes a brief discussion and analysis of the extinction correction, as applied to each of these tiles. We determine the electron temperature distributions in § 6.2, and in § 6.3, we analyse the T_e distributions in terms of average temperatures and fractional mean-square temperature variations in the plane of the sky. In § 6.4, we introduce three novel methods for determining the errors in the lines, and

ultimately in t_A^2 (among these is the convolved Gaussian method mentioned briefly in § 2.2). § 6.5 provides a discussion and conclusions.

6.1 Extinction and reddening correction

Before deriving the T_e distribution from the STIS data, we first correct for extinction. This was done simply by comparing the observed $F_{H\alpha}/F_{H\beta}$ ratio with the theoretical ratio $I_{H\alpha}/I_{H\beta}$. (For the analysis in this chapter, this was deemed to be adequate, not needing to resort to the full list of H I and He I lines as discussed in Chapters 3 and 4.) We use a value of 2.88 assuming $T_e = 8500$ K and $N_e = 5000$ cm⁻³, case B (Storey & Hummer, 1995). The extinction correction is done in terms of $C_{H\beta}$, given by the relationship

$$\log[F_\lambda/F_{H\beta}] = \log[I_\lambda/I_{H\beta}] - f_\lambda C_{H\beta}, \quad (6.1)$$

where f_λ is the extinction curve. For the H γ ($\lambda 4341$), $\lambda 4363$, $\lambda 4861$, $\lambda 4959$, $\lambda 5007$, $\lambda 5755$, $\lambda 6548$, $\lambda 6563$, and $\lambda 6583$ lines, the respective values for f_λ are 0.0856, 0.082, 0, -0.0153 , -0.0225 , -0.1237 , -0.2185 , -0.2202 , and -0.2226 (see Chapter 3). This leads to,

$$C_{H\beta} = 4.541 \log[F_{H\alpha}/F_{H\beta}] - 2.086. \quad (6.2)$$

The correction for extinction/reddening from observed to intrinsic flux for the 4363 and 5007 lines is then given by,

$$I_{4363} = F_{4363} 10^{1.082 C_{H\beta}} \quad ; \quad I_{5007} = F_{5007} 10^{0.9775 C_{H\beta}} \quad , \quad (6.3)$$

and for the $\lambda 5755$ and $\lambda 6583$ lines by,

$$I_{5755} = F_{5755} 10^{0.8763 C_{H\beta}} \quad ; \quad I_{6583} = F_{6583} 10^{0.7774 C_{H\beta}} \quad . \quad (6.4)$$

Excluding the tiles that overlapped the STIS fiducial bars, this produced $C_{H\beta}$ results for from 79 to 96 tiles, depending on the slit/visit observed, which are the same set used later for the T_e analysis. The distributions of $C_{H\beta}$ along the two slits (Slit 1 and Slit 2) observed in 3 separate visits (V2, V52, and V72) are remarkably similar. Furthermore, the distributions match well for the regions of Slit 1 and Slit 2 that are adjacent to each other. Recall that the separation between the bottom of Slit 1 and the top of Slit 2 is a mere 0''.211 and that Slit 2 is shifted 18''.056 relative to Slit 1 along the slit spatial direction. The average $C_{H\beta}$ values without regard to any weighting for brightness are: for Slit 1: 0.680, 0.699, and 0.701 respectively for the three visits; for Slit 2: 0.762, 0.798, and 0.766. For Slit 4, it is 0.566 and for Slit 5, it is 0.611. We comment further on Slit 1, which covers the proplyd P159-350 and 1SW. Starting at the SE end of Slit 1, the values are roughly flat at ~ 0.85 . There is a spike to 1.43 in V2 at

the tile containing most of the proplyd. The behavior is similar for V72 with a spike to 1.33 at the tile containing most of the proplyd. The adjacent nebula has for both visits a $C_{H\beta}$ value of ~ 0.9 . Unfortunately, because P159-350 was centred in the East fiducial bar on V52, we cannot reliably measure $C_{H\beta}$ there. Where Slit 1 crosses 1SW, $C_{H\beta}$ is ~ 0.6 , which agrees well with our previous spectroscopic value 0.605 at our position observed with the Faint Object Spectrograph (FOS-1SW, Rubin et al., 1998). At the end of Slit 1 toward the NW, $C_{H\beta}$ has decreased to ~ 0.4 .

We examined the vicinity of P159-350 in more detail using the original resolution of 1 pixel ($0''.05$) for Slit 1 in the spatial direction. The increase in flux and thus signal-to-noise (S/N) in the vicinity of the proplyd permits meaningful analysis here. For V2, we find that the peak observed flux occurs in pixel 311 for the $H\alpha$ (5.64×10^{-11} erg cm $^{-2}$ s $^{-1}$ arcsec $^{-2}$) $H\beta$ (6.83×10^{-12}), and $\lambda 4363$ (3.18×10^{-13}) lines, while the $\lambda 5007$ line reaches the highest peak (6.71×10^{-12}) at pixel 317 and a second relative maximum (5.14×10^{-12}) at pixel 305 with a clear trough between these, having a relative minimum (3.58×10^{-12}) occurring at pixel 310. The $F_{H\alpha}/F_{H\beta}$ ratio peaks at 8.269 also at pixel 311 and hence the derived $C_{H\beta}$ reaches a peak value there of 2.08.

Repeating the analysis for V72, we find that the peak observed flux occurs in pixel 343 for the $H\alpha$ (2.19×10^{-11}) and $\lambda 4363$ (8.11×10^{-14}) lines. The $H\beta$ peaks in pixel 344 (3.19×10^{-12}) and is lower at pixel 343 (2.74×10^{-12}). The $\lambda 5007$ line reaches the highest peak (5.77×10^{-12}) at pixel 350 and a second relative maximum (4.58×10^{-12}) at pixel 336, again with a distinct trough between these, having a relative minimum (2.85×10^{-12}) occurring at pixel 344. The $F_{H\alpha}/F_{H\beta}$ ratio peaks at 7.994 at pixel 343 where the derived $C_{H\beta}$ reaches a peak value of 2.01. The fact that the peak surface brightnesses are much higher for P159-350 in V2 compared with V72 is most likely because the brightest part of the proplyd was better sampled and/or aligned with the 1 pixel \times 10 pixel ($0''.05$ by $0''.5$) “smallest rectangular aperture” in the former visit than the latter.

6.2 Electron temperature determination

6.2.1 [O III] electron temperature

The electron temperature, T_e , is derived from the intrinsic ratio I_{5007}/I_{4363} using the following relation,

$$T_e = 32966 / [\ln(I_{5007}/I_{4363}) - 1.701] \quad . \quad (6.5)$$

Effective collision strengths are from Burke et al. (1989) for $T_e = 10^4$ K. Transition probabilities (A-values) are from Froese Fischer & Saha (1985). Note that this holds in the low- N_e limit,

which should be valid for Orion where N_e values are less than the critical densities (N_{crit}) for these lines. The lowest $N_{crit} \sim 6.4 \times 10^5 \text{ cm}^{-3}$ for the 5007 line, which is well above N_e values determined (e.g., Peimbert & Torres-Peimbert, 1977; Osterbrock et al., 1992; Esteban et al., 1998).

We continue with the analysis using the tiles along the slit described above; the number of usable tiles varies with the slit/visit and ranges from 79 to 96. Equations 6.2, 6.3, and 6.5 are applied to the four emission lines to derive T_e . Figure 6.1(a) shows the distribution of T_e versus position along Slit 1. For Slit 1, position along the slit is relative to the location of peak surface brightness (SB) in the $H\alpha$ line, which occurs at P159-350. We set our zero corresponding to coordinates, $\alpha, \delta = 5^{\text{h}}35^{\text{m}}15^{\text{s}}.94, -5^{\circ}23'50''.04$ (C. R. O'Dell, private communication). As mentioned in the last section, there is actually a relative minimum in the $[\text{O III}] \lambda 5007$ SB close to that position. The lower curve in Figure 6.1(a) shows the observed $\lambda 5007$ SB ($\text{erg cm}^{-2} \text{ s}^{-1} \text{ arcsec}^{-2}$), which is displayed (unsmoothed) at the pixel level providing $0''.05$ spatial resolution along the slit. The feature at the very left (SE) end of this slit is associated with the prominent arc of HH 529, part of which we used to define our position x2 and which was better observed in Slit 2. The open circles on the top (T_e) curve represent the individual tiles plotted at their midpoint. The dashed lines are a linear interpolation across the tiles that were deemed to have unreliable measurements because of proximity to the fiducial bars. There is a remarkably flat T_e distribution with the notable exception of an upward spike to 13600 K at the tile containing the bulk of the proplyd $H\alpha$ emission. For Slit 1 and V2, the behavior is similar with a sharp upward spike to 15050 K at the tile containing the bulk of the proplyd $H\alpha$ emission. It is most unlikely that these high temperatures are realistic (these tiles are omitted in the statistical analysis to follow) and are the result of equation 6.5 not accounting for the higher electron densities, probably in excess of 10^6 cm^{-3} , in P159-350. Because the $\lambda 5007$ line will then suffer considerable collisional deexcitation, T_e derived using equation 6.5 will be overestimated (e.g., Viegas & Clegg, 1994). In the next section, we will evaluate the distribution of T_e along Slit 1, as well as along the other slits, in terms of T_e variations.

Figure 6.1(b) shows the distribution of T_e versus position along Slit 2, where position along the slit is relative to the location of the local peak SB in the $\lambda 5007$ line that occurs at x2. Using the position of P159-350 and the specified offset from Slit 1 to Slit 2 of +1.08s in RA and $-8''.15$ in Dec., we find x2 coordinates: $\alpha, \delta = 5^{\text{h}}35^{\text{m}}16^{\text{s}}.96, -5^{\circ}23'57''.73$. The lower relative maximum near offset +14'' is where Slit 2 passes through the “downstream” tail of P159-350. Again there is a remarkably flat T_e distribution.

Figure 6.2(a) plots the distribution of T_e versus position along Slit 4, where position along the slit is relative to the location of a feature in the bar seen in the $\lambda 6583$ SB distribution (Fig. 6.2(c)) discussed in the next section. Recall that this slit is aligned to point toward

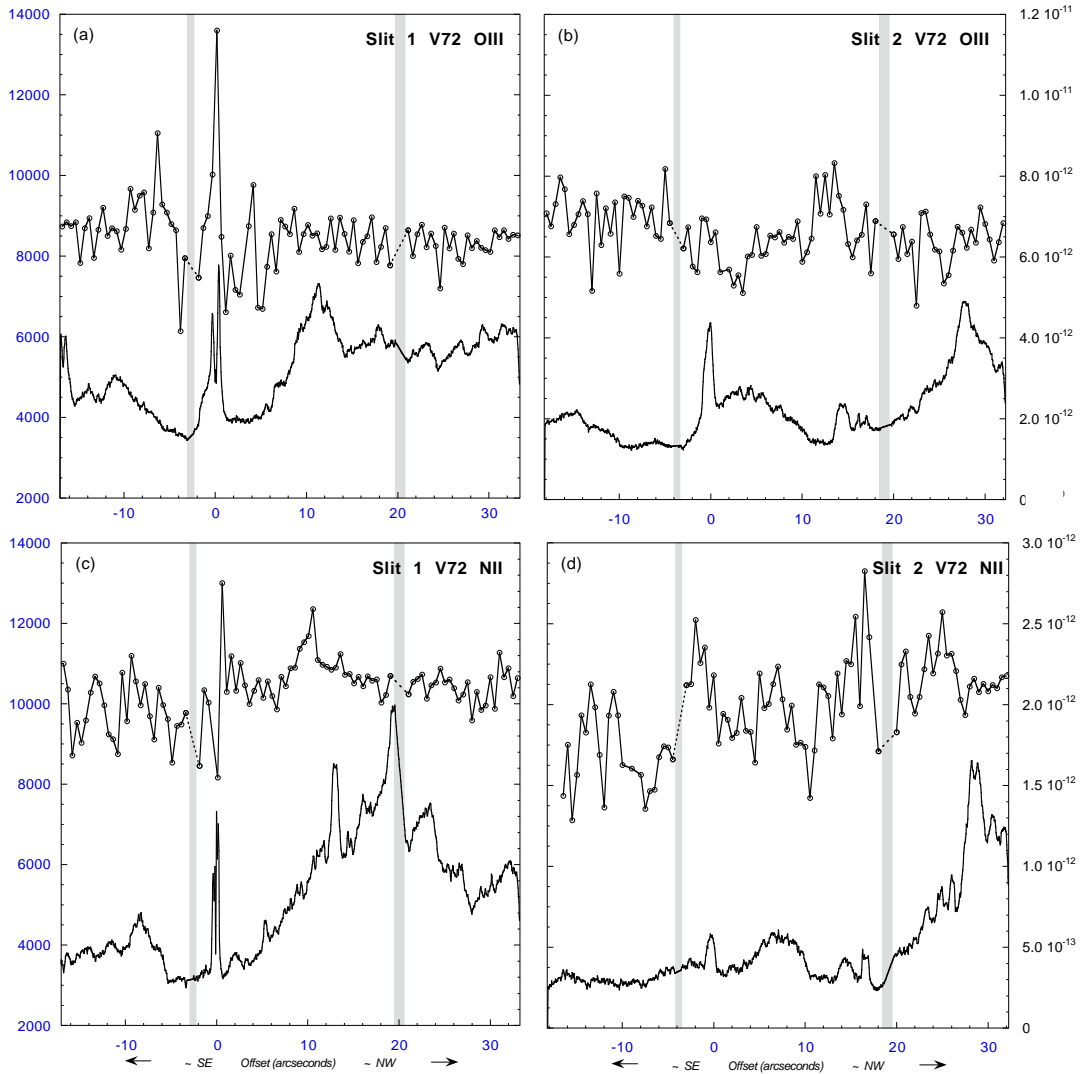


Figure 6.1 **(a)** Slit 1, V72: Plot of T_e determined from the $[\text{O III}] \lambda 4363/\lambda 5007$ flux ratio versus position along the STIS long-slit. The analysis is in terms of tiles that are $0''.5$ square (matching the slit width). The open circles represent the individual tiles plotted at their midpoint. The dashed straight lines are interpolations across the two fiducial bars, indicated by the gray area, where data are unreliable. Positional measurement along the slit is from $\sim\text{SE}$ to $\sim\text{NW}$ (see Figure 2.1). The zero point is described in the text. Typical errors are $\pm 300 - 500$ K and have been excluded in the interest of clarity. See § 6.4 for a discussion. The bottom curve shows the observed $[\text{O III}] \lambda 5007$ surface brightness in units of $\text{erg cm}^{-2} \text{s}^{-1} \text{arcsec}^{-2}$ displayed unsmoothed at the pixel level. **(b)** same as (a) for Slit 2, V72. **(c)** same as (a) except the upper curve is a plot of T_e determined from the $[\text{N II}] \lambda 5755/\lambda 6583$ flux ratio assuming $N_e = 5000 \text{ cm}^{-3}$; the lower curve shows the observed $[\text{N II}] \lambda 6583$ surface brightness. **(d)** same as (c) for Slit 2, V72.

θ^1 Ori C. While there is an underlying decrease in the $\lambda 5007$ SB with increasing distance from θ^1 Ori C, there is a leveling off (plateau) at the SE end of Slit 4 of $\lambda 5007$ emission that remains substantial well beyond the bar. This is consistent with the WFPC2 images of the region; the composite “drizzled” image by Walsh (1998) that includes filter F502N (which covers the $\lambda 5007$ line) depicted in green, shows a green hue in a parabolic shape that appears to be a wake emanating from HH 203 and HH 204. Walsh’s image is available at stecf.org/newsletter/webnews1/orion/m42col_drizzle.jpg. The point was also made in an earlier discussion of HH 203 and HH 204 (O’Dell et al., 1997b). Along this slit, the T_e distribution is also fairly flat, especially in the region of higher S/N (see §4.2). There is a clear increase in the amplitude of the T_e fluctuations for the tiles SE of the bar due to poorer S/N in the $\lambda 4363$ line.

In Figure 6.2(b), we plot the distribution of T_e versus position along Slit 5. Here, the position along the slit is relative to the location of a feature seen in the $\lambda 6583$ SB distribution (Fig. 6.2(d)) discussed below. There is roughly a linear decrease in $\lambda 5007$ emission from the NW to the SE end of Slit 5 with a “jump” occurring between 18–22'' offset position. As was the case for Slit 4, here too there remains substantial $\lambda 5007$ emission beyond the bar that is evident in the green hue at this location in the Walsh image. The T_e distribution here is flat similar to that for Slit 4; the increase in the T_e amplitude range at the SE end of the slit is again due to poorer S/N in the $\lambda 4363$ line.

6.2.2 [N II] electron temperature

The T_e in the N^+ zone is derived from the intrinsic ratio I_{6583}/I_{5755} (see equations 6.2 and 6.4). Because the critical density for the $\lambda 6583$ line, $\sim 7.7 \times 10^4 \text{ cm}^{-3}$ (at 10⁴ K), is substantially less than N_{crit} for the [O III] 5007 line ($\sim 6.4 \times 10^5 \text{ cm}^{-3}$), we do consider various N_e values when deriving T_e . We also derive temperatures utilizing two different sets of N^+ effective collision strengths – those calculated by Lennon & Burke (1994) and by Stafford et al. (1994). We use the effective collision strengths for 10000 K; these do not vary much with the T_e range of interest in Orion. The A-values used are discussed in Rubin et al. (1998), Appendix A with original references therein.

For non-zero densities, our derivation of T_e is done in an iterative fashion, starting with an initial estimate in the low- N_e limit. Then the volume emissivities (j_λ values) for both the $\lambda 5755$ and $\lambda 6583$ lines are calculated solving the statistical equilibrium equations for the six lowest energy levels. The T_e value is then recomputed using the intrinsic ratio I_{6583}/I_{5755} , j_{6583} , and j_{5755} . The rapidly converging iteration is halted when T_e changes by less than 1 K.

In this chapter, we are interested in assessing the amount of t^2 that can occur. Thus, we limit our analysis here by not including a detailed study of density variations. Nevertheless, it

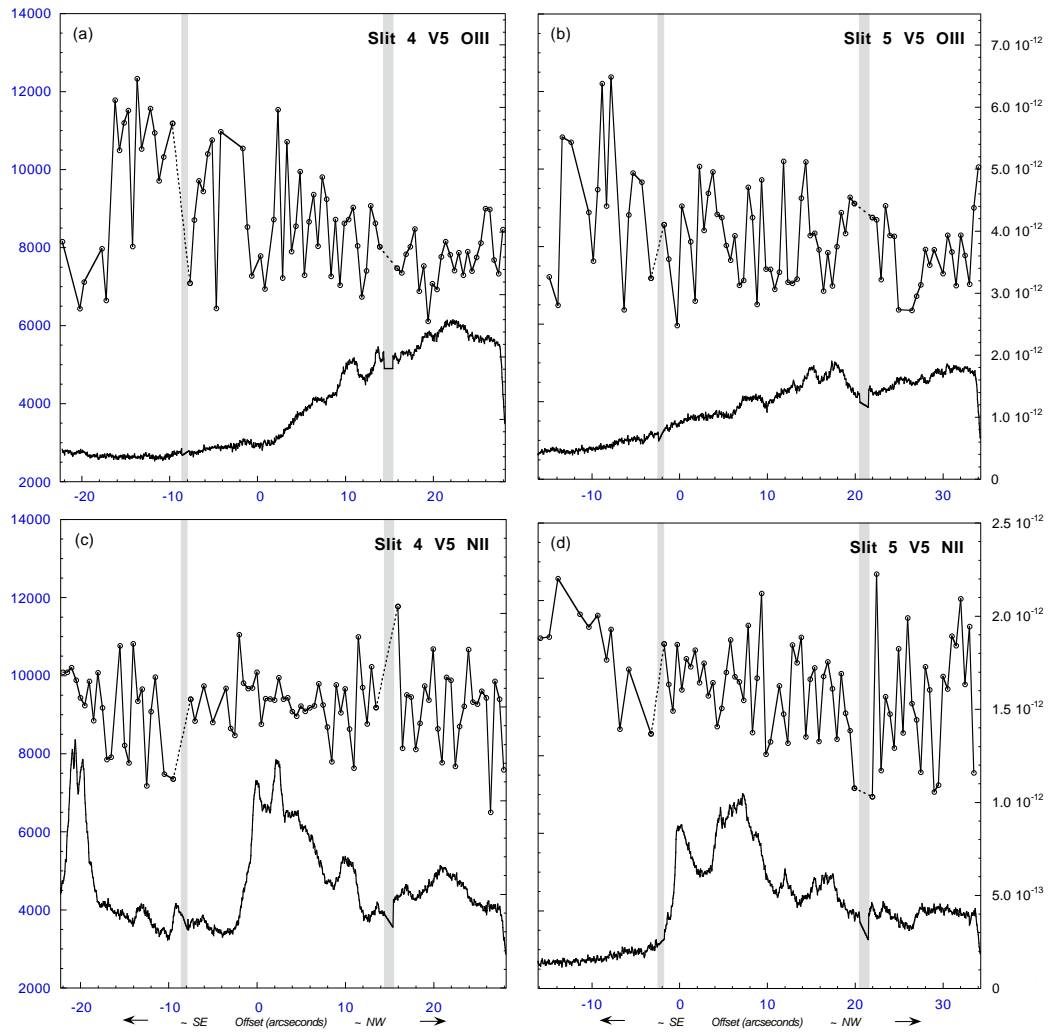


Figure 6.2 (a) Slit 4, V5: Same as Fig. 6.1 (a) (b) same as (a) for Slit 5, V5. (c) Slit 4, V5: Same as Fig. 6.1 (c) except that $N_e = 2000 \text{ cm}^{-3}$ is assumed. (d) same as (c) for Slit 5, V5.

is necessary to include some discussion of N_e with regard to deriving the [N II] T_e . As is well known, there is an inverse scaling of [N II] T_e with N_e . First we perform the calculations for T_e in the low- N_e limit. This provides a firm upper limit to the T_e distributions evaluated for the various slit/visit data. We also repeat the full computations for 4 other N_e 's: 1000, 2000, 5000, and 10000 cm^{-3} . The last value is more than high enough to bracket expectations for Orion, with the exception of objects like the proplyds as will be discussed below for P159-350. The value of 5000 cm^{-3} is our best single N_e to cover the region of slits 1 and 2 (e.g., Pogge et al., 1992). Their map of the electron density in the S⁺ zone indicates that N_e is lower in the regions of our Slit 4 and Slit 5; for these, we adopt a best single $N_e = 2000$. It is these respective densities that are used to depict the distribution along slits 1, 2, 4, and 5 of [N II] T_e in Figure 6.1(c), 6.1(d), 6.2(c), and 6.2(d) respectively. For the Figures, we have used the N⁺ collision strengths of Lennon & Burke (1994) while results from both this set and Stafford et al. (1994) will be tabulated later. The lower curve in each of these panels shows the 6583 surface brightness distribution along the slit.

Figure 6.1(c) shows the tiled [N II] T_e distribution versus position along Slit 1 and is a positional match to Figure 6.1(a). The lower curve here shows the observed $\lambda 6583$ SB at the unsmoothed pixel level. There again appears to be a relative minimum in the [N II] $\lambda 6583$ SB at the centre pixel for P159-350 although it is not as well defined as the dip in the $\lambda 5007$ SB there. As with the $\lambda 5007$ curve, the peak SB on the NW side of the proplyd exceeds that on the SE side. However, the overall 6583 emission is much narrower in P159-350 than is the $\lambda 5007$ emission. In totality, the structural behavior in the $\lambda 6583$ emission compared with that in $\lambda 5007$ is consistent with the N⁺ region being more tightly confined than is the O⁺⁺ region to the low-mass star of P159-350, which is expected if the proplyd is externally ionized by θ^1 Ori C. The prominent absolute maximum of the $\lambda 6583$ SB is very close to the 1SW position, 20'26 from P159-350, which is somewhat blocked by the NW-side fiducial bar. The narrow secondary peak at $\sim 13''$ offset appears to be associated with the much broader secondary maximum near offset $\sim 12''$ in the $\lambda 5007$ SB of Figure 6.1(a). There is perhaps an ionization boundary being observed here, although the slit orientation is far from ideal to test this. A slit pointing toward θ^1 Ori C would be better suited. Once again, there is a notably flat T_e distribution with the exception of the proplyd. In Figure 6.1(c), we have omitted the tile with the highest derived T_e of 20815 K. The highest T_e in the plot is at 13000 K. Both these tiles are omitted from the subsequent statistical analysis. These high derived T_e 's are undoubtedly pointing more to high N_e values associated with the proplyd than high temperatures. The N_e assumed for the calculation of T_e in Figure 6.2(c) is 5000 cm^{-3} , while N_e for P159-350 may exceed 10⁶ cm^{-3} . Because the $\lambda 6583$ line emission will suffer enormously from collisional deexcitation at more realistic densities, the derived T_e would be much lower. For Slit 1, V2, there are two tiles at

the proplyd that have an enormous upward spike in T_e to 29800 and 35850 K; both tiles are omitted from the statistical analysis in following sections.

Figure 6.1(d) has the distribution of [N II] T_e versus position along Slit 2. There is a fairly flat T_e distribution with some indication of a drop in T_e SE of the lower fiducial bar. The maximum $\lambda 6583$ SB in the lower curve occurs near offset $28''$. This location is immediately adjacent to the narrow peak at $\sim 13''$ offset in Figure 6.1(c), just mentioned. The relatively small peak at x2 (offset 0) further supports the finding in the WFPC2 composite image that the emission arc which includes the position x2 is mainly an [O III] feature (see Figure 2.1). We note that x2 is part of the HH 529 complex and more specifically, the easternmost feature called 170-358 (see Fig. 20 in Bally et al., 2000). According to their study, including the kinematics, 170-358 is an expanding bow shock seen from the side. This feature is analysed in more detail in Chapter 7.

Figure 6.2(c) plots the distribution of [N II] T_e versus position along Slit 4. Position along this slit is relative to the location of the SE-most peak in SB in the $\lambda 6583$ line. We set our zero corresponding to coordinates: $\alpha, \delta = 5^{\text{h}}35^{\text{m}}21^{\text{s}}.34, -5^{\circ}24'48''.21$ determined from the position of our offset star θ^2 Ori A (HD37041) with $\alpha, \delta = 5^{\text{h}}35^{\text{m}}22^{\text{s}}.9, -5^{\circ}24'57''.9$. There is a brighter feature that occurs where the slit crosses HH 203 at offset near $-20''$. Comparison with Figure 6.2(a) shows no enhancement in $\lambda 5007$. This is consistent with the WFPC2 images of the region; the composite image in Figure 2.1 that includes filter F658N (isolating the $\lambda 6583$ line) shows HH 203 as a reddish-orange object. There is a very flat T_e distribution even over the wide range of SB and ionization structure along Slit 4.

In Figure 6.2(d), we plot the distribution of T_e versus position along Slit 5. Here, the zero position along the slit is the SE-most $\lambda 6583$ SB peak of where there is a bifurcation in the bar (see Figure 2.1). This feature appears to mark the boundary between the ionized region and the photodissociation region (PDR). Using the position of θ^2 Ori A and the specified offset from Slit 4 to Slit 5 of -1.87s in RA and $-15''.32$ in Dec., we find: $\alpha, \delta = 5^{\text{h}}35^{\text{m}}19^{\text{s}}.74, -5^{\circ}25'08''.14$. Beyond this position, the T_e distribution becomes less reliable because of poorer S/N in the $\lambda 5755$ line. Overall, the T_e is flat as has been the case throughout.

6.3 Fractional mean-square temperature variations

Our STIS analysis above presents results spatially across the plane of the sky. The observations here do not address temperature fluctuation along the line of sight, which may be characterized in terms of the average temperature T_0 and fractional mean-square T_e variation (t^2) as defined by Peimbert (1967).

$$T_0 \equiv \frac{\int T_e N_e N_i dV}{\int N_e N_i dV}, \quad (6.6)$$

$$t^2 \equiv \frac{\int (T_e - T_0)^2 N_e N_i dV}{T_0^2 \int N_e N_i dV} , \quad (6.7)$$

where N_i is the ion density N_{N^+} or $N_{O^{++}}$. The integration in equations 6.6 and 6.7 is over the column defined by each tile, and along the line of sight. We are unable to measure the t^2 along the line of sight for any column (cross section 1 tile). If there are t^2 along the line of sight, we can say that $T(4363/5007) > T_0$ or $T(5755/6583) > T_0$ (e.g., Peimbert, 1967; Rubin et al., 1998).

In the case of [O III], for each tile, we have calculated $T(4363/5007)$. Then the intrinsic flux I_{5007} , fully correcting F_{5007} for extinction (see equ. 6.3), in each tile is used in conjunction with $T_e = T(4363/5007)$ for that tile, and assumed constant along the line of sight, to derive the following:

$$I_{5007} = K_{5007} \int N_e N_i T_e^{-0.5} \exp(-\chi/k T_e) dl = K_{5007}(T_e) \int N_e N_i dl . \quad (6.8)$$

Here χ is the excitation energy above the ground state for the upper level of the $\lambda 5007$ transition, k is the Boltzmann constant, K_{5007} is known from atomic data, and finally $K_{5007}(T_e)$ has incorporated the known T_e factor with the atomic constants. This leaves us with $\int N_e N_i dl$ for each tile, to be used in the derivations below. Here we again make the safe assumption of the low- N_e limit (negligible collisional deexcitation) discussed earlier.

For the case of [N II], for each tile, we have calculated $T(5755/6583)$. Then the intrinsic flux I_{6583} , fully correcting F_{6583} for extinction (see equ. 6.4), in each tile is used in conjunction with $T_e = T(5755/6583)$ for that tile and the chosen value for N_e , and assumed constant along the line of sight, in the following relation:

$$\int N_e N_i dl \propto \frac{I_{6583}}{\epsilon_{6583}} . \quad (6.9)$$

Here ϵ_{6583} is the normalized volume emissivity which is related to the usual volume emissivity j_{6583} by $\epsilon_{6583} \equiv j_{6583}/(N_e N_i)$. The emissivity, ϵ_{6583} , depends on the (fractional) population in a given level obtained by solving the 6-level atom for the specific T_e and N_e . It is not necessary to deal with the constant of proportionality for our purposes.

Following Rubin et al. (2002), we define the average T_e ($T_{0,A}$) and fractional mean-square T_e variation (t_A^2) in the *plane of the sky*.

$$T_{0,A} \equiv \frac{\int \int T_e N_e N_i dl dA}{\int \int N_e N_i dl dA} , \quad (6.10)$$

$$t_A^2 \equiv \frac{\int \int (T_e - T_{0,A})^2 N_e N_i dl dA}{T_{0,A}^2 \int \int N_e N_i dl dA} = \frac{\int \int T_e^2 N_e N_i dl dA}{T_{0,A}^2 \int \int N_e N_i dl dA} - 1 , \quad (6.11)$$

where dA represents an element of surface area in the plane of the sky and the integration over dl is for each tile along the line of sight. The proper weighting for each tile is provided by

either equation 6.8 or equation 6.9 depending on whether we are performing an [O III] or [N II] analysis.

The results using the STIS data for the various slits and visits to determine $T_{0,A}$ and t_A^2 are summarized in Table 6.1. These quantities for [O III] are entered in the first column. For Slit 1, Visit 72 (see Figure 6.1(a)), $T_{0,A} = 8258$ K and $t_A^2 = 0.00925$. We have excluded the spike in T_e at the proplyd. The value for t_A^2 is remarkably low, although not as low as the value of 0.0035 found for NGC 7009 (Rubin et al., 2002). The results from the other visits (V2 and V52) for Slit 1 are close to those for V72. Our results for Slit 2 and all three of the visits show $T_{0,A}$ values in close accord and similar to those for Slit 1. All these averages vary by less than 285 K. By comparing t_A^2 for slits 1 and 2 in all 3 visits, we see that all six numbers are small, ranging from 0.00682 to 0.0129. For slits 4 and 5 the statistics are roughly comparable and differ from those for slits 1 and 2 in the following ways: $T_{0,A}$ is several hundred K smaller and t_A^2 is somewhat higher, although the largest value, 0.0176, is still notably small. A simple visual comparison of the T_e plots in Figures 6.1(a), 6.1(b), 6.2(a), and 6.2(b) leads one to conclude that t_A^2 looks larger for slits 4 and 5, particularly with the larger T_e excursions in the regions SE of the bar. We note however that these data with poorer S/N have a minor effect on the statistics. There is natural biasing against these tiles due to weaker emission in both $\lambda 4363$ and $\lambda 5007$ as can be seen from equation 6.8, which in turn provides a smaller ($\int N_e N_i dl$)–weighting of these tiles in equations 6.10 and 6.11.

All the remaining columns in Table 6.1 pertain to the derivation of $T_{0,A}$ and t_A^2 for [N II]. These are displayed for 5 different electron densities and two different sets of effective collision strengths. As described, for slits 1 and 2 our preferred N_e is 5000 cm^{-3} , while for slits 4 and 5, it is 2000 cm^{-3} . We will now discuss the resulting numbers in these particular density columns and also using the left-side column with the Lennon & Burke (1994) collision strengths, unless stated otherwise. For Slit 1, Visit 72 (see Figure 6.1(c)), $T_{0,A} = 10226$ K and $t_A^2 = 0.00695$. We exclude the high T_e near P159-350 (see §4.2). The value for t_A^2 is even lower than found for this slit/visit in the [O III] analysis; $T_{0,A}$ is nearly 2000 K higher. There is close agreement among the N^+ $T_{0,A}$ and t_A^2 values for all the visits for Slit 1; the above intercomparison between N^+ and O^{++} with the corresponding numbers in the respective visits is also true.

For Slit 2, the $T_{0,A}$ numbers vary by more than 400 K between visits; the respective $T_{0,A}$'s are smaller than for Slit 1 for V52 and V72 but slightly higher for V2. All of the t_A^2 values are larger for Slit 2 than for Slit 1, reaching 0.0146.

For Slits 4 and 5, the N^+ $T_{0,A}$ is several hundred to more than 1000 K smaller than for slits 1 and 2. Compared with the O^{++} $T_{0,A}$, slits 4 and 5 are higher by 1343 and 1749 K, respectively. t_A^2 at 0.0175 is largest for Slit 5 and nearly identical to the corresponding O^{++} value, which is also the highest in the first column. This larger t_A^2 may be attributed to the

Table 6.1. Values of $T_{0,A}$ and t_A^2 for STIS slits

O ⁺⁺	N ⁺									
	0		1000		2000		5000		10000	
N_e (cm ⁻³) ^a										
Slit 1, Visit 2										
8151 ^b	11104	(10605) ^c	10881	(10458)	10670	(10317)	10114	(9929)	9381	(9386)
1.04 ^b	0.860	(0.795)	0.844	(0.785)	0.831	(0.777)	0.791	(0.752)	0.730	(0.712)
Slit 1, Visit 52										
8232	11236	(10727)	11010	(10578)	10796	(10435)	10232	(10042)	9488	(9491)
0.887	0.647	(0.592)	0.633	(0.584)	0.620	(0.576)	0.584	(0.553)	0.531	(0.517)
Slit 1, Visit 72										
8258	11232	(10723)	11005	(10573)	10791	(10429)	10226	(10036)	9481	(9485)
0.925	0.765	(0.703)	0.750	(0.694)	0.736	(0.685)	0.695	(0.659)	0.636	(0.620)
Slit 2, Visit 2										
8142	11171	(10665)	10945	(10517)	10732	(10373)	10170	(9982)	9429	(9433)
1.15	1.05	(0.956)	1.02	(0.942)	1.00	(0.929)	0.941	(0.890)	0.853	(0.831)
Slit 2, Visit 52										
8074	10675	(10208)	10463	(10068)	10262	(9933)	9733	(9564)	9038	(9046)
1.29	1.60	(1.48)	1.57	(1.46)	1.54	(1.44)	1.46	(1.39)	1.33	(1.30)
Slit 2, Visit 72										
8358	10909	(10424)	10691	(10280)	10484	(10141)	9938	(9760)	9221	(9227)
0.682	1.43	(1.31)	1.40	(1.30)	1.37	(1.28)	1.30	(1.23)	1.18	(1.15)
Slit 4, Visit 5										
7790	9473	(9107)	9298	(8991)	9133	(8879)	8698	(8572)	8125	(8143)
1.57	0.985	(0.918)	0.968	(0.906)	0.952	(0.896)	0.906	(0.867)	0.837	(0.821)
Slit 5, Visit 5										
7678	9789	(9394)	9603	(9271)	9427	(9151)	8962	(8825)	8353	(8369)
1.76	1.82	(1.69)	1.79	(1.66)	1.75	(1.64)	1.66	(1.58)	1.52	(1.49)

^aelectron density assumed for N⁺ emission-line region; 0 denotes the low density limit

^bupper row $T_{0,A}$ (K); lower 100 t_A^2

^cusing effective collision strengths from Lennon & Burke, 1994 (Stafford et al., 1994)

larger excursions in T_e in those tiles SE of the bar, where the S/N in the $\lambda 5755$ line is poorer. A comparison of Figure 6.2(c) and 6.2(d) clearly indicates a much lower $\lambda 6583$ surface brightness SE of the bar for Slit 5 than for Slit 4. Again we emphasize that these data with poorer S/N play only a minor role in contributing to the integrals in equations 6.10 and 6.11. When there is weaker emission in both $\lambda 5755$ and $\lambda 6583$, as can be seen from equation 6.9, there is a smaller ($\int N_e N_i dl$)-weighting of these tiles in equations 6.10 and 6.11.

The effect of substituting the Stafford et al. (1994) collision strengths is small for both Slit 1 and Slit 2 for all 3 visits: $T_{0,A}$ decreases by less than 200 K; t_A^2 decreases by roughly 5–6 percent. The $T_{0,A}$ drop for slits 4 and 5 is slightly more, up to a 276 K difference; t_A^2 decreases by ~ 6 –7 percent.

On the whole, the results presented in Table 6.1 allow us to reach two robust conclusions. First, t_A^2 is always very small (≤ 0.0182) for either the O^{++} or N^+ analyses. Second, the $T_{0,A}$ derived from the [O III] lines is always significantly less than $T_{0,A}$ derived from the [N II] lines. These hold even when we consider for the N^+ analysis a wide range in N_e that should amply bracket the great bulk of the plasma in Orion and also examine the influence of using alternative collision strengths.

In § 6.4, we present an analysis of the uncertainties in the derived T_e values as well as the t_A^2 values.

6.4 Error analysis

The values found for t_A^2 are very small. It is important to determine whether even these small fluctuations in T_e from tile to tile are a real signal or the result of measurement uncertainty.

From equation 6.5 for O^{++} , it can be shown that the mean square uncertainty in temperature, expressed as t_e^2 , has the following dependence on the uncertainties δI_n and δI_a of the nebular (I_n) and auroral (I_a) line fluxes, respectively:

$$t_e^2 = (\delta T_e / T_e)^2 = \frac{T_e^2}{c_1^2} \left[\left(\frac{\delta I_a}{I_a} \right)^2 + \left(\frac{\delta I_n}{I_n} \right)^2 \right], \quad (6.12)$$

where $c_1 = 32966$. We use this as an approximation for N^+ too, with $c_1 = 24933$.

The uncertainty δI is principally the measurement error in the line flux for a tile. The S/N for the flux of the auroral lines ([O III] $\lambda 4363$ and [N II] $\lambda 5755$ here) is much lower than that for the nebular lines ([O III] $\lambda 5007$ and [N II] $\lambda 6583$ here), and so the uncertainty of the weaker auroral line will dominate the uncertainty δT_e . The uncertainty δI also depends on the (differential) extinction correction, but in the present case this is a small effect compared to the uncertainty in the observed auroral line fluxes (hence, $I/\delta I \sim F/\delta F = S/N$).

The three independent methods used to calculate the S/N of the auroral lines are discussed in the following sections. We use $T_e \sim T_{0,A}$ to calculate the corresponding t_e^2 . Method 2 is the method used to determine the errors of the lines from the $13'' \times 0''.5$ tiles in Chapters 3 and 4.

6.4.1 Method 1 – Continuum approximation

The flux integrated over the line profile as found using the “blkavg sum” technique in IRAF is

$$F^{line} = \sum_{i=1}^m D F_i^{line+cont} - \frac{m}{n} \sum_{j=1}^n D F_j^{cont}, \quad (6.13)$$

where F_i is the monochromatic flux for the tile ($\text{erg cm}^{-2} \text{s}^{-1} \text{\AA}^{-1}$), D is the dispersion conversion ($\text{\AA}/\text{pixel}$), n is the number of pixels in the spectrum used to define the *continuum* and m is the number of pixels used for the *line + cont*. Since the auroral line is weak, the rms fluctuation in the *line + cont* can be assumed to be the same as in the *continuum*, δF_j^{cont} . Thus, the rms of the line flux is

$$\delta F^{line} = D \sqrt{m} (\delta F_j^{cont}) \sqrt{1 + m/n}. \quad (6.14)$$

In our measurements we used $m = n$. The above three equations are used to create the entries for method 1 (M1) in Table 6.2. Values are given for both the [O III] $\lambda 4363$ and [N II] $\lambda 5755$ lines for all slits (for slits with multiple visits, a representative case is given).

6.4.2 Method 2 – Line profile

In this method, the line profiles from the STIS spectra are fit with a template (a Gaussian convolved with a slit of width $0''.5$) using a combined Gauss-Newton and modified Newton algorithm (Numerical Algorithms Group (NAG) - E04FDF) to find the minimum least-squares solution and the corresponding variances of the variables used in the fit (NAG-E04YCF). The slit width is held constant, but due to anamorphic magnification in the dispersion direction, the plate scale differs from line to line which results in different slit widths expressed as pixels (see Bowers & Baum, 1998).

The variables used in the template fitting are the flux F^{line} , the FWHM and central wavelength of the Gaussian, and the slope and mean brightness of the continuum. The variances reflect how well the model fits the data. Keeping all of these as variables gives one a conservative estimate of the variance of each. Note that a poor template would lead to an overestimate of the error. The templates were tested on the strong nebular lines and generally fit very well. However, there are instances where the surface brightness changes across the slit (in the dispersion direction), so that the implicit assumption of uniform illumination is not perfect. Therefore, the estimated uncertainty from method 2 is an upper limit. As is seen in Table 6.2 it agrees well with the error estimated using method 1.

Table 6.2. Weak line uncertainties and the associated fractional mean-square temperature variation, t_e^2

Line	Slit	Visit	Method ^a	$(\delta F_a/F_a)_{median}$	$T_{0,A}$	δT_e	$100t_e^2$	$100t_A^2$				
4363	1	V72	M1	0.1434	8258	297	0.129	0.925				
			M2	0.1132		234	0.080					
			^b M3a	0.1826		378	0.209					
			^b M3b			388	0.221					
4363	2	V72	M1	0.2003	8358	424	0.258	0.682				
			M2	0.2577		546	0.427					
			^b M3a	0.2593		550	0.432					
			^b M3b			513	0.377					
4363	4	V5	M1	0.3129	7790	576	0.547	1.57				
			M2	0.5350		985	1.60					
4363	4NW	V5	M1	0.2435	7665	434	0.320	0.973				
			M2	0.1550		276	0.130					
4363	5	V5	M1	0.4274	7678	764	0.991	1.76				
			M2	0.4527		810	1.11					
4363	5NW	V5	M1	0.3235	7683	579	0.568	1.42				
			M2	0.3310		593	0.595					
			5755	1		V72	M1	0.0499	10226 ^c	209	0.042	0.695 ^c
			M2				0.0616	258	0.064			
	^b M3a	0.0937	393	0.148								
	^b M3b		388	0.144								
5755	2	V72	M1	0.1188	9938 ^c	471	0.224	1.30 ^c				
			M2	0.1090		432	0.189					
			^b M3a	0.1879		744	0.561					
			^b M3b			729	0.538					
5755	4	V5	M1	0.1491	9133 ^d	499	0.298	0.952 ^d				
			M2	0.1226		410	0.202					
5755	5	V5	M1	0.1459	9427 ^d	520	0.304	1.75 ^d				
			M2	0.1284		458	0.236					
5755	5	V5	M1	0.1459	9427 ^d	520	0.304	1.75 ^d				
			M2	0.1284		458	0.236					

^aMethods 1-3 (M1-M3) are discussed in § 6.4.

^bV2,V52 and V72 are used for Method 3.

^c $N_e = 5000 \text{ cm}^{-3}$ using effective collision strengths from Lennon & Burke 1994

^d $N_e = 2000 \text{ cm}^{-3}$ using effective collision strengths from Lennon & Burke 1994

6.4.3 Method 3 – Multiple measurements

This method utilizes the multiple sets of observations for Slit 1 and Slit 2 in the three visits V2, V52 and V72 and examines the reproducibility of the line fluxes and T_e . There are adequate fiducial sources visible in all three visits so that the spectra may be shifted in the spatial direction to achieve alignment to ~ 1 pixel. The proplyd P159-350 in Slit 1 is particularly useful for this and serves for Slit 2 as well because the relative positional HST offsets between Slit 1 and Slit 2 are not subject to the acquisition uncertainty. There is also positional alignment uncertainty in the dispersion direction which is more difficult to estimate. For all three visits, P159-350 was seen in the $0''.5$ wide slit; although it was blocked for the most part by the East fiducial bar in V52, some of the emission still peeks out both ends. We noted at the end of § 6.1 that P159-350 has a higher peak surface brightness in V2 than in V72. We estimate that the positional alignment of the tiles perpendicular to the spatial direction between the three visits is within $0''.2$ so that there is substantial area overlap (perhaps 60%) of our tiles between the three visits. Comparison of the nebular line strengths from visit to visit shows excellent reproducibility ($< 3\%$ per tile for the O^{++} line). This is much smaller than the auroral line differences found among successive visits. The measurement error of the weaker auroral lines is of course higher. Furthermore lack of registration is a more serious issue for the auroral lines (from a much higher energy level) if there are real T_e fluctuations on this spatial scale; in the limit of no overlap, one would expect $t_e^2 \sim t_A^2$ even if there were no measurement errors. Therefore, having t_e^2 from method 3 larger than from M1 and M2 is not unexpected.

For each tile in common between V2, V52 and V72, both an average value (F_a) and the standard deviation (δF_a) of any single determination of F_a were calculated. The representative value entered as M3a in Table 6.2 is the median $\delta F_a/F_a$ for each of the slits; as in methods 1 and 2, the δT_e listed is what is implied by this S/N, through equation 6.12.

For each in-common tile, we also calculated T_e for each visit, then the average T_e and the actual standard deviation (δT_e) of any single determination of T_e . The median δT_e for each slit is included in Table 6.2 as M3b. From these median values we calculated the tabulated t_e^2 . Methods 3a and 3b agree closely, as they should given the good reproducibility of the nebular lines (i.e., the effect of δF_n in equation 6.12 is negligible).

The analysis summarized in Table 6.2 shows that the measured t_A^2 is a real signal not dominated by the noise and/or measurement errors. The two exceptions are for the O^{++} measurements for slits 4 and 5 which include tiles beyond the Orion bar (SE part of the slit) where the surface brightness for lines of that ion, and hence the S/N, is low. Accordingly, we repeated the entire analysis for only the NW half of these slits. The results recorded in Table 6.2 show a lower t_A^2 , as anticipated, and a lower t_e^2 as well which is a smaller fraction of t_A^2 .

Where there is a contribution of measurement error to the apparent t_A^2 , the actual t_A^2 is smaller, by about t_e^2 . This reinforces our conclusion that t_A^2 is very small.

6.5 Discussion and conclusions

The observations here do not address T_e fluctuation along the line of sight through the specific O^{++} region or, likewise, through the N^+ region. We analyse both the [O III] and [N II] data sets to derive the average T_e and fractional mean-square T_e variations in the plane of the sky, which we call $T_{0,A}$ and t_A^2 . We assume for each square column (projection of 1 STIS tile $0'.5$ square on the plane of the sky) that the plasma along the line of sight is isothermal at the $T(4363/5007)$ in the case of O^{++} or $T(5755/6583)$ in the case of N^+ . For the latter case, we consider a large range of N_e values, which should be sufficient for Orion, in order to produce Table 6.1. The analysis for each N_e assumes that it is constant for the entire STIS slit length and throughout the sheet projected through the nebula along the line of sight.

Fluctuations in T_e (and N_e) along the line of sight are inevitable. We can make some comments about how our results for t_A^2 might be adjusted by T_e variations along the line of sight. The relationship between $T(4363/5007)$ and T_0 for the O^{++} region is

$$T(4363/5007) = T_0 [1 + 0.5(91200/T_0 - 3)t^2], \quad (6.15)$$

and between $T(5755/6583)$ and T_0 for the N^+ region is

$$T(5755/6583) = T_0 [1 + 0.5(69000/T_0 - 3)t^2], \quad (6.16)$$

(e.g., Peimbert, 1967; Rubin, 1969). With the $T(4363/5007)$ – or $T(5755/6583)$ –values for Orion (see Figures 6.1 and 6.2) or indeed for H II regions in general, T_0 will be smaller than these temperatures inferred from the forbidden line flux ratios here.

We do not have the data here to characterize T_e variations in 3-dimensions (3-D). It is useful to define an *overall* 3-D average T_e ($T_{0,V}$) and fractional mean-square T_e variation (t_V^2). These single values apply for the *entire source*. Equations 6.6 and 6.7 define these specific values when the integration is over the entire volume. We note that for a spatially unresolved object (total integrated fluxes observed in the aperture), *not* the case for Orion, $t_V^2 = t^2$ and a calculation of t_A^2 is meaningless.

Our measurements of T_e reported here are an average along each line of sight. Because each element of area treated in the plane of the sky represents a column that has already created a spatially averaged temperature along the line of sight (e.g., see Fig. 1 in Rubin, 1969), it is likely that the value for t_V^2 is substantially higher than t_A^2 . Measurements of t^2 along various sight lines appear to be the most direct way to reliably gauge t_V^2 . Therefore, despite finding remarkably

low t_A^2 , we cannot completely rule out much larger temperature fluctuations along the line of sight. Further work is underway that will use modeling as well as additional observational data in an effort to better determine the relationship between t^2 , t_A^2 , and t_V^2 .

Finding [N II] temperatures that are higher than [O III] temperatures is not a new result. For Orion, this has been known for years (e.g., Baldwin et al., 1991). What is new/significant here is that we have results from many more sight lines, more than 700 represented by the individual tiles, with improved spatial resolution (0.5 arcsec squares) and excellent spatial registration between the [N II] and [O III] data sets that HST affords. Of the roughly 700 tiles, about half represent independent sight lines, with the other half having spatial overlap due to the repeated visits for slits 1 and 2.

The fact that the [N II] temperatures are higher is also expected on theoretical grounds and again, not something novel that we have uncovered. We enumerate three factors that contribute to the predicted inequality. First, the cooling of the [O III] $\lambda\lambda 5007, 4959$ lines in the O^{++} region is uniquely efficient for nebular conditions and elemental abundances that prevail in Galactic H II regions, including Orion. On the other hand, in the “singly ionized” region (where the dominant O and N ions are O^+ , N^+) there is no coolant that is nearly as efficient as [O III] $\lambda\lambda 5007, 4959$ is in the O^{++} zone. Additionally for Orion, the blister geometry likely results in higher average electron densities in the singly ionized region compared with the O^{++} region because the former is closer to the PDR. The higher N_e in the N^+ region would also contribute to less efficient cooling.

Second, there is the predicted hardening of the stellar ionizing photons at progressively larger distances from the exciting star. This is due to the functional form of the H photoionization (predominantly) cross section, which diminishes steeply with higher frequency from its value near threshold. At larger distances from the exciting source, the average energy per photoionization will increase and thus the heating rate will also increase. This causes a rise in T_e with an increase in distance (other factors being equal). This has been known for many years (e.g., Rubin et al., 1998).

Third, there is a possibility that there is a contribution to the production of [N II] $\lambda 5755$ emission (and to a lesser extent $\lambda 6583$) by recombination and cascading. Under some conditions, this may provide significant routes into the upper energy level of the $\lambda 5755$ transition that are not negligible compared with collisional processes. This was examined by Rubin (1986). If there was a significant “recombination” contribution to the observed emission, we would have overestimated the T_e derived from the [N II] $\lambda 5755/\lambda 6583$ flux ratio. With our two independent, detailed models for the Orion Nebula (Baldwin et al., 1991; Rubin et al., 1991), the recombination contribution appears to be small.

All three of the above effects are included in the photoionization, plasma simulation models

of Rubin et al. (1991) and Baldwin et al. (1991) (and our CLOUDY models in Chapters 4 and 7). The predicted [N II] and [O III] temperatures for the entire volume are 8721 K and 7704 K in the Rubin et al. (1991) model and 8649 K and 7692 K in the retrofit (Rubin et al., 1998) using Stafford et al. cross sections. When the Lennon & Burke (1994) N^+ collision strengths are used instead of the Stafford et al. set, the respective temperatures become 8706 K and 7701 K.

Finally, we encapsulate the findings here for the proplyd P159-350. We find large local extinction as evidenced by the dramatic increase in the observed $F_{H\alpha}/F_{H\beta}$ ratio along slit 1. For V2, this ratio peaks at 8.27 which implies a $C_{H\beta}$ of 2.08 from the Balmer decrement. Similar values are found for our V72 observations: $F_{H\alpha}/F_{H\beta}$ peaks sharply at the proplyd position reaching a ratio of 7.99, where the derived $C_{H\beta} = 2.01$. Because the adjacent nebular values for $C_{H\beta}$ are much lower, the extinction must be associated with the P159-350 environs.

A comparison of the [O III] $\lambda 5007$ and [N II] $\lambda 6583$ surface brightnesses in the vicinity of P159-350 (see Figures 6.1(a) and 6.1(c)) shows for both lines that the SB on the NW side of the proplyd exceeds that on the SE side. However, the $\lambda 6583$ emission is much narrower than is the $\lambda 5007$ emission which provides evidence of ionization stratification consistent with the N^+ region being more tightly confined than is the O^{++} region to the low-mass star of P159-350. This “inverse H II region” behavior is precisely what is expected due to the external ionization source θ^1 Ori C.

The derived T_e distributions were all notably flat except at the position of the proplyd observed in slit 1. The very high derived T_e ’s at the location of P159-350 are no doubt due more to high N_e values associated with the proplyd than high temperatures. As stated, the calculations used here to assess T_e have not accounted for N_e values likely to exceed 10^6 cm^{-3} in P159-350. Because both the $\lambda 5007$ line and even more so the $\lambda 6583$ line emission will suffer substantial collisional deexcitation at such high densities, the derived T_e for both [O III] and [N II] would be much lower.

Each of the above mentioned facets of P159-350 deserves further study. The smallest spatial resolution element was 1 pixel ($0''.05$) in the spatial direction by 10 pixels ($0''.5$) in the dispersion direction. It would be highly desirable to obtain higher spatial resolution of P159-350, which can be readily achieved by observing with a narrower STIS slit. The narrower slit would enable better spectral resolution as well and permit a detailed mapping of P159-350 in the C III] $\lambda\lambda 1907, 1909$ lines. The ratio of their fluxes is an excellent diagnostic of N_e even at the high N_e values expected in proplyds. Improved spectral resolution in the optical lines will also help sort out kinematics from spatial structure, which was a difficulty with the $0''.5$ slit width we used.

Chapter 7

A photoionized Herbig-Haro object in the Orion Nebula

Star-forming regions – such as the Orion Nebula – are home to various phenomena associated with the early stages of stellar evolution. Some of the more prominent features in the visible part of the spectrum are the arcs associated with gas flows known as Herbig-Haro (HH) flows (Reipurth & Bally, 2001). Many of these flows have been identified in the Orion Nebula and have had both their radial (Doi et al., 2004) and tangential (Doi et al., 2002) velocities measured. The origins of these flows have in a few cases been associated with IR sources embedded within the Orion Molecular Cloud 1 South (OMC-1S) (Doi et al., 2002). However, there are many flows that have not been paired with any source (X-ray, radio, or near-IR) – including HH 529 (O’Dell & Doi, 2003). This flow contains at least three curved shocks which appear in [O III] WFPC2 images (O’Dell & Wong, 1996) and extend approximately $36''$ from the centre of the inferred source of the optical outflow (OOS) at α, δ (J2000) = $5^{\text{h}}35^{\text{m}}14^{\text{s}}.56, -5^{\circ}23'54''$ (O’Dell & Doi, 2003; Doi et al., 2004).¹ This is 0.08 pc in the plane of sky given a distance to the nebula of 460 pc (Bally et al. (2000), hereafter BOM).

The radial (line-of-sight) velocity is -44 km s^{-1} (Doi et al., 2004). This radial velocity is quoted as “systemic” – relative to the [O III] nebular component, which itself has a heliocentric velocity of $+18 \pm 2 \text{ km s}^{-1}$ (Doi et al., 2004). Coupling this with the heliocentric radial velocity

¹ In addition to HH 529, many other HH flows (HH 269, HH 202 and HH 203/204) appear to originate in the OOS region – supplying ample evidence for OOS housing HH flow driver(s). Smith et al. (2004) have detected an infrared source (IR source 2 in their Table 2; $\alpha, \delta = 5^{\text{h}}35^{\text{m}}14^{\text{s}}.40, -5^{\circ}23'51''.0$) which lies within $3''$ of the predicted location of the OOS. Zapata et al. (2004) have also observed this source at 1.3cm. Within the OOS region, Bally et al. (2000) have identified another near-IR source (‘s’ in their Fig. 20) which was concurrently labelled HC209 (Hillenbrand & Carpenter, 2000): $\alpha, \delta = 5^{\text{h}}35^{\text{m}}14^{\text{s}}.57, -5^{\circ}23'50''.8$. Recently, an X-ray source (F421, Feigelson et al., 2002) has been found to be coincident with this near IR source. However, there is still not definitive proof as to the particular driving source as neither of these sources lies directly in line with the flow of HH 529.

of the PDR (+28 km s⁻¹, Goudis, 1982), we obtain a radial velocity relative to the source embedded within OMC-1: -54 km s⁻¹. The average proper motion velocity is 54 km s⁻¹ (Doi et al., 2004) which leads to a total velocity of 76 km s⁻¹ (with respect to OMC-1S) at an angle of 45° out of the plane of the sky.

Using this geometry, a distance from the embedded source to the leading edge of the eastern-most shock can be calculated: 0.12 pc (36'' × √2). Assuming that the source lies within OMC-1S and that θ¹ Ori C is itself ∼ 0.25 pc from the main ionization front (Wen & O'Dell, 1995; O'Dell, 2001a), this would place the HH 529 system on the far side (i.e., further from the observer) of θ¹ Ori C. It is remarkable that the flow has emerged from the cloud into the ionized zone.

The dynamical age of the HH 529 system can be calculated from the average proper motion (25 mas yr⁻¹). Assuming that the proper motion has remained constant over the 36'' from its point of origin, we find the dynamical age of the eastern-most visible feature of HH 529 to be roughly 1500 years. All shock model timescales will need to be consistent with this dynamical age in order for the model to be valid (§ 7.4).

As was recognized by O'Dell et al. (1997a), the fact that this and other Orion nebula HH flows appear strongly in [O III] (atypical of most HH flows which show much lower ionization) suggests that these shocks are photoionized. We examine the physical conditions of HH 529 by comparing our high-resolution echelle spectra with (matter-bounded) photoionization models of this feature. Other studies of non-photoionized HH flows show evidence for a decrease in the amount of Fe depletion in some of the shocks, as determined from [Fe II] lines (Böhm & Matt, 2001; Beck-Winchatz et al., 1996). This has been linked to grain destruction as matter originating from the molecular cloud passes through the shocks. In this chapter, we assess the Fe depletion using a set of [Fe III] lines in the eastern-most feature of HH 529.

7.1 Observations

One of the CTIO echelle spectra slits, x2, was chosen to align with the Herbig-Haro object, HH 529 (see Fig. 7.1). Wavelength and flux calibrations of the spectra were performed as in Chapter 2. We also used archival flux-calibrated (O'Dell & Doi [1999] using Baldwin et al. [1991]) Hubble Space Telescope (HST) WFPC2 associations (F487N, F502N, F547N, F631N, F656N, F658N, and F673N) and Bally mosaics of these associations (less F487N). As there were a series of discrepant exposure times in the image headers of the Bally mosaics, the flux calibration had to be redone – again using the ground-based spectroscopic results of Baldwin et al. (1991) – to determine the relevant exposure times. With these exposure times in hand, all WFPC2 pixel brightnesses (from both Bally mosaics and archival WFPC2 associations) have been accurately converted to absolute fluxes/surface brightnesses, matching the ground-based

flux calibration of Baldwin et al. (1991).

Looking at the spatially resolved x2 echelle spectra, we have noticed two distinguishing features associated with the shock feature: a wide ($5''$) velocity-shifted component and a narrow ($2''.5$) velocity bridge seemingly connecting the nebula and the shock. Such a bridge feature – which can also be seen in Figure 6 of Bally et al. (2000) (hereafter, BOM00) – appears only to be associated with the leading optically visible shock. As this feature is intrinsically narrow ($1''.5$ from WFPC2 images), we have been able to determine the effective seeing for the red and blue spectra by measuring the width (along the slit) of the He I $\lambda 5876$ bridge feature – a line that is found in both the red and blue spectra (see Fig. 7.2). The seeing was slightly different on each of the two observing nights: $2''$ for the red observations and $2''.5$ for the blue. We can also see from this figure that the blue and red slits are aligned along their lengths to an accuracy of $\sim 0''.2$. However, there are small differences in the absolute observed flux, most probably as a result of a position difference in the transverse direction, along the shock feature. These deviations are addressed in § 7.1.1.

A direct comparison of spatial variation in ground-based and space-based observations over the same wavelength range was made to confirm that the flux calibration of the echelle spectra is robust and that the slit alignment and orientation are correct. The echelle spectra were extracted over the same wavelength bandpass as the F656N WFPC2 filter. With knowledge of the approximate slit position (from a Polaroid of the slit against the nebular background), the F656N flux-calibrated image was used to re-create the expected spatial variation along the slit. This re-created profile was convolved with an appropriate-width ($2''$) Gaussian to simulate the seeing of the ground-based observations (see Fig. 7.3). This processing allows for direct comparison between ground- and space-based observations. (Note that there has been no continuum [or line contamination] subtraction from either the echelle spectrum or the WFPC2 reproduction, so the surface brightnesses (SBs) in Fig. 7.3 are not those of H α .) The slit's position on the F656N WFPC2 image was adjusted – while maintaining the slit orientation, $PA = 116^\circ$ – so as to emulate more accurately the ground-based echelle slit spatial variation. This required only a slight adjustment ($< 1''$) of the slit from its original position on the WFPC2 image. Using the slit position determined from this analysis, we compared all WFPC2 filters with their respective portions of the ground-based spectra, resulting in accurate reproductions of both the spatial variation and absolute flux.



Figure 7.1 Red $\times 2$ slit position as determined from a Polaroid of the slit taken during observations, and the surface brightness variation across the slit as compared with the underlying F656N ($H\alpha$) WFPC2 image (O'Dell & Wong, 1996). The extracted section ($12''.5 \times 1''$) of the slit is shown.

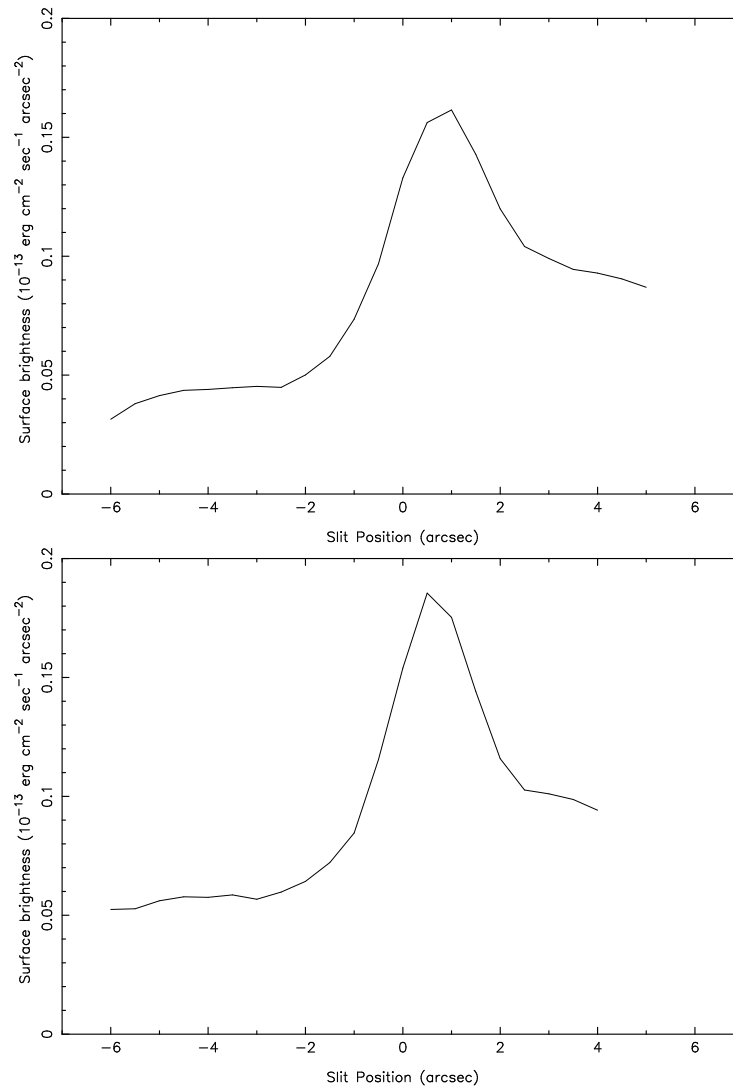


Figure 7.2 Flux variation of the He I 5876 spatially-narrow velocity-bridge component (+ continuum) along the slit in the blue spectrum (top) and in the red spectrum (bottom).

The high-resolution echelle spectra allow us to analyse the spatial variation of the nebula and shock separately – offering insight not possible from the WFPC2 photometry. For example, the slit variation of the [O III] $\lambda 5007$ and [O II] $\lambda 3726$ shock fluxes are shown in Figure 7.4. Differences in variation across the slit between these two ions may be indicative of a higher density at the eastern-most edge of the shock: a higher density would lead to more recombinations and a slightly higher ionization fraction for O^+ .

These WFPC2 and shock component analyses suggest that 10 pixels ($-0''.5$ to $+4''.0$) along the slit should be extracted in order to obtain the best contrast between the background nebular component and the velocity-shifted shock component (referred to hereafter as simply the “nebular” and “shock” components). Following this extraction, and with the nebular line identifications from Baldwin et al. (2000) as a guide,² the x2 spectral features were fit with two Gaussian components representing the nebular and shock components, as was done by Doi et al. (2004). Eight parameters were used in the fit: FWHM, peak wavelength and area for both components, and two parameters to fit the continuum baseline level and slope. The result of such a fit is shown in Figure 7.5.

For cases in which the shock component had a low signal-to-noise ratio ($S/N < 5.2$), the lines were re-fit with a constrained double Gaussian. The strong nebular component of the constrained fit had no constraints while the weaker shock component’s FWHM was fixed using the weighted average of the stronger lines’ FWHM (28.3 km s^{-1}). The constrained velocity of the shock component was set using the weighted mean of the H I shock components (-42.1 km s^{-1}) and was maintained as a constant relative to the H I gas. Because of the ionization/velocity structure along the line of sight (Baldwin et al., 2000), the actual velocity differences between the weak shock component and the strong nebular component depend on the ion. If the S/N of the shock component improved and remained above 2.6, the constrained fit was used. Otherwise the double-Gaussian fit was used for all lines with $S/N_{shock} > 2.6$.

If the double- and constrained Gaussian fits resulted in an undetectable shock component ($S/N < 2.6$), a five-component (FWHM, peak wavelength, area, continuum baseline, and slope) single-Gaussian fit was used for the nebular line. The results of the line-fitting models are shown in Table 7.1 with nebular (neb) and shock (sh) components included in separate consecutive rows for each identification (ID) wavelength. Column descriptions are included in the table.

²All ID wavelengths are from Atomic Line List v2.04 (<http://www.pa.uky.edu/~peter/atomic/>, maintained by P. A. M. van Hoof), except [O II] (Chapter 5).

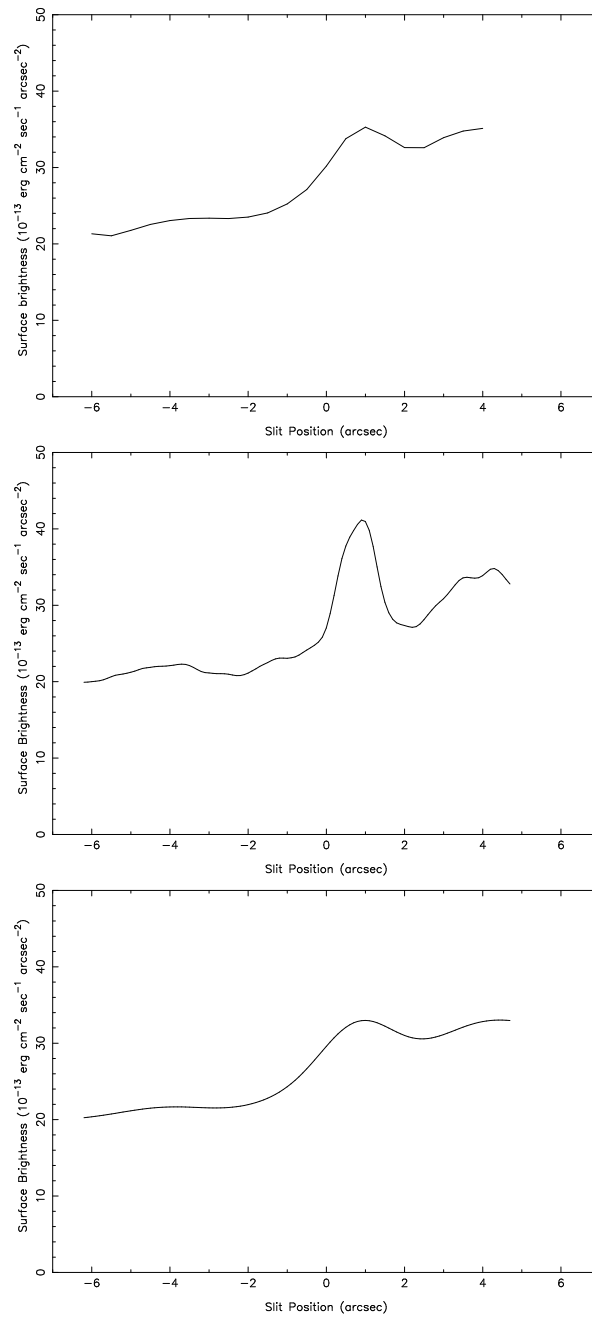


Figure 7.3 $\text{H}\alpha$ region comparison between ground-based echelle spectroscopy (top) and WFPC2 photometry (F656N) (middle, bottom) as a function of slit position. The bottom panel is the result of a $2''$ Gaussian convolution of the WFPC2 slit extraction (middle) to simulate the $2''$ seeing. These include $\text{H}\alpha$, continuum and line contamination from neighbouring lines (namely, $[\text{N II}]$).

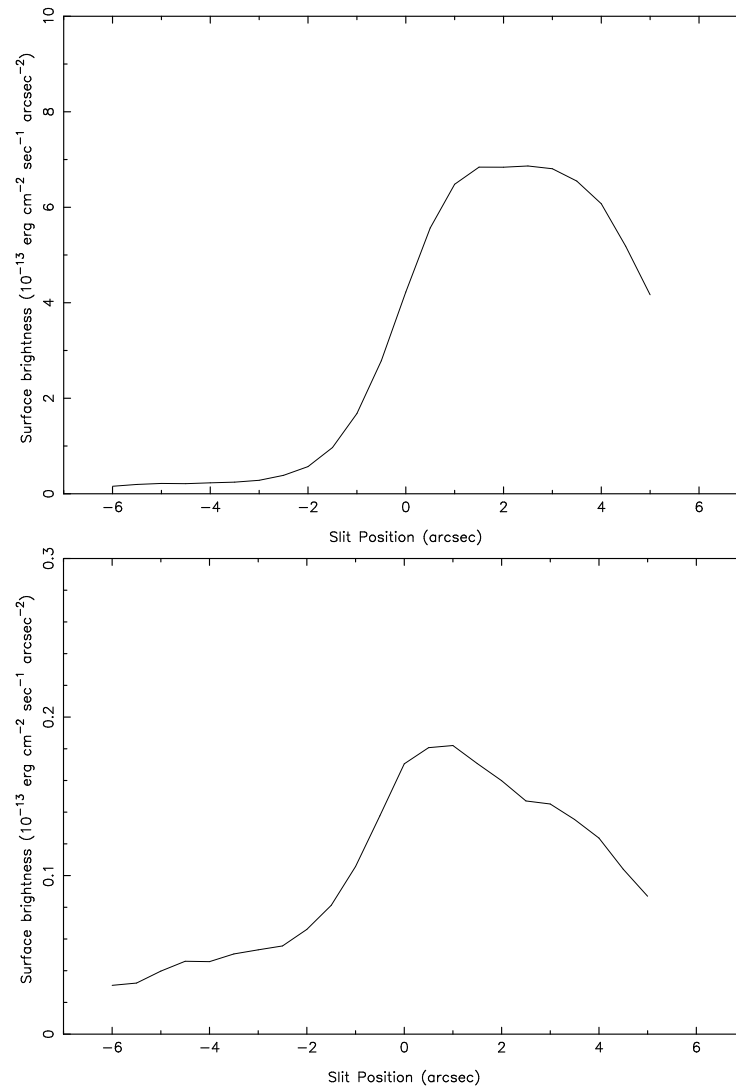


Figure 7.4 Variation of the [O III] $\lambda 5007$ (top) and [O II] $\lambda 3726$ (bottom) velocity-shifted shock component line flux across the $12''.5$ slit (25 pixels). The greater O^+/O^{++} ratio near the eastern, leading edge, indicates a somewhat higher density there.

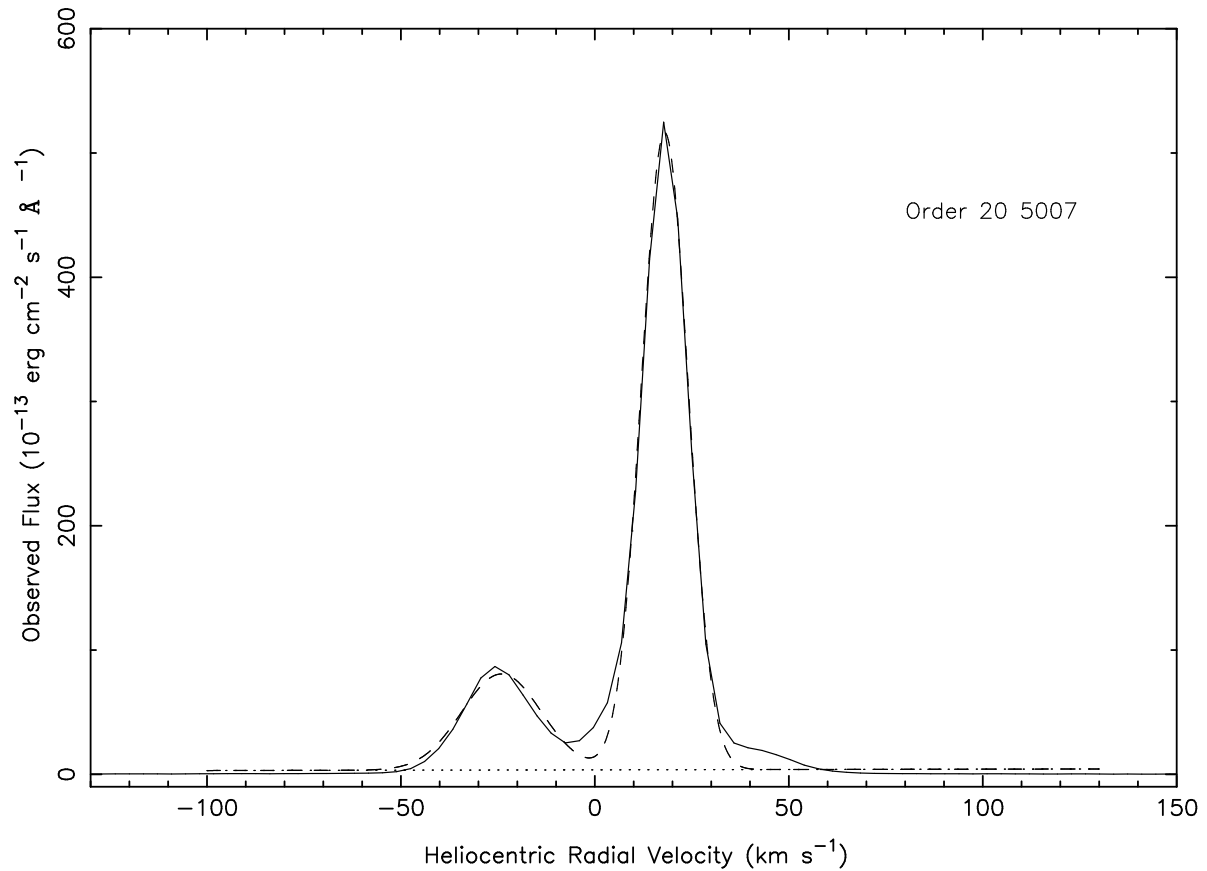


Figure 7.5 Double Gaussian fit of the nebular and velocity-shifted shock components. Eight parameters were used in the fit: FWHM, peak wavelength and area for both components, and two parameters to fit the continuum baseline level and slope. There is a third scattered light (redshifted) component which was not fit, explaining the poor fit redward of the nebular component. The uncertainties quoted in Table 7.2 reflect this poor fit. The systemic (nebular) heliocentric velocity is $+18 \pm 2 \text{ km s}^{-1}$ for [O III] (O’Dell, 2001b).

Table 7.1. Summary of double Gaussian fits to observed echelle spectra

ID	Wave ^{a,b}	ID	? ^c	Wavel ^d	Velocity ^e	FWHM ^{e,f}	I_{corr} ^{g,h}	S/N ⁱ	$I_{\text{sh}}/I_{\text{neb}}$ ^j	Notes ^k
(1)	(2)	(3)	(4)	(5)	(6)	(7)	(8)	(9)	(10)	
3512.505	He I	?	3512.526	1.8 ± 1.7	19.1 ± 4.4	0.0718 ± 0.0167	4.3	0.6992 ± 0.2724	C	
		?	3512.023	-41.1 ± 1.7	28.3 ± 0.0	0.0502 ± 0.0157	3.2			
...		?	3530.556	...	33.0 ± 9.9	0.1582 ± 0.0546	2.9	...	S	
					
3554.389	He I		3554.424	3.0 ± 0.8	13.9 ± 1.8	0.1042 ± 0.0129	8.1	...	S	
					
3587.253	He I		3587.281	2.3 ± 1.6	23.9 ± 4.1	0.2617 ± 0.0467	5.6	0.5319 ± 0.1723	C	
		?	3586.767	-40.6 ± 1.6	28.3 ± 0.0	0.1392 ± 0.0376	3.7			
...		?	3599.206	...	31.3 ± 10.1	0.0523 ± 0.0174	3.0	0.9484 ± 0.3826	C	
		?	3598.700	...	28.3 ± 0.0	0.0496 ± 0.0113	4.4			
3613.642	He I		3613.636	-0.5 ± 0.3	16.9 ± 0.9	0.2252 ± 0.0115	19.6	0.2091 ± 0.0561	C	
		?	3613.135	-42.1 ± 0.3	28.3 ± 0.0	0.0471 ± 0.0124	3.8			
3634.241	He I		3634.231	-0.8 ± 0.5	19.4 ± 1.3	0.2391 ± 0.0158	15.1	0.1765 ± 0.0664	C	
		?	3633.729	-42.2 ± 0.5	28.3 ± 0.0	0.0422 ± 0.0156	2.7			
3655.593	H I	?	3655.611	1.5 ± 1.8	25.5 ± 6.2	0.1160 ± 0.0446	2.6	...	S	
					
3656.106	H I	?	3656.175	5.7 ± 1.3	13.6 ± 3.7	0.0409 ± 0.0124	3.3	...	S	
					
3656.663	H I		3656.662	-0.1 ± 0.8	23.7 ± 2.4	0.0775 ± 0.0099	7.8	...	S	
					
3657.267	H I	?	3657.302	2.9 ± 1.6	22.9 ± 4.7	0.0917 ± 0.0224	4.1	...	S	
					
3657.923	H I	?	3657.920	-0.3 ± 2.4	22.6 ± 6.7	0.0809 ± 0.0289	2.8	...	S	
					
3658.639	H I		3658.648	0.7 ± 1.6	28.9 ± 4.5	0.1088 ± 0.0205	5.3	...	S	
					
3659.421	H I		3659.423	0.2 ± 1.1	19.6 ± 3.0	0.0752 ± 0.0121	6.2	...	S	
					
3660.277	H I		3660.267	-0.8 ± 1.6	26.7 ± 4.2	0.1014 ± 0.0188	5.4	...	S	
					
3661.218	H I		3661.237	1.5 ± 0.7	21.0 ± 2.0	0.1151 ± 0.0111	10.4	...	S	
					
3662.256	H I		3662.235	-1.8 ± 1.0	27.7 ± 2.6	0.1287 ± 0.0130	9.9	...	S	
					
3663.404	H I		3663.390	-1.1 ± 0.8	26.5 ± 2.2	0.1624 ± 0.0146	11.1	...	S	
					
3664.676	H I		3664.677	0.1 ± 0.6	27.9 ± 1.5	0.1975 ± 0.0110	17.9	...	S	
					
3666.095	H I		3666.085	-0.8 ± 0.5	24.9 ± 1.1	0.2409 ± 0.0117	20.6	0.1669 ± 0.0425	C	
		?	3665.583	-41.9 ± 0.5	28.3 ± 0.0	0.0402 ± 0.0100	4.0			
3667.681	H I		3667.681	0.0 ± 0.6	30.2 ± 1.4	0.2748 ± 0.0139	19.8	0.1885 ± 0.0344	C	
			3667.161	-42.5 ± 0.6	28.3 ± 0.0	0.0518 ± 0.0091	5.7			
3669.464	H I		3669.454	-0.8 ± 0.4	24.4 ± 1.0	0.2962 ± 0.0125	23.7	0.1286 ± 0.0352	C	
		?	3668.949	-42.1 ± 0.4	28.3 ± 0.0	0.0381 ± 0.0103	3.7			
3671.475	H I		3671.472	-0.3 ± 0.4	27.1 ± 1.0	0.3229 ± 0.0118	27.4	0.1796 ± 0.0339		
			3670.958	-42.3 ± 2.0	25.2 ± 5.0	0.0580 ± 0.0107	5.4			
3673.758	H I		3673.755	-0.2 ± 0.3	26.2 ± 0.8	0.3341 ± 0.0111	30.0	0.1140 ± 0.0256	C	
		?	3673.242	-42.1 ± 0.3	28.3 ± 0.0	0.0381 ± 0.0085	4.5			
3676.362	H I		3676.359	-0.2 ± 0.3	27.1 ± 0.9	0.3908 ± 0.0129	30.3	0.1592 ± 0.0254	C	
			3675.845	-42.2 ± 0.3	28.3 ± 0.0	0.0622 ± 0.0097	6.4			
3679.352	H I		3679.345	-0.6 ± 0.2	28.7 ± 0.6	0.4524 ± 0.0094	48.2	0.1645 ± 0.0192		
			3678.808	-44.3 ± 1.1	25.2 ± 3.0	0.0744 ± 0.0086	8.7			
3682.808	H I		3682.797	-0.9 ± 0.2	25.3 ± 0.7	0.4455 ± 0.0124	35.8	0.1320 ± 0.0219	C	
			3682.292	-42.0 ± 0.2	28.3 ± 0.0	0.0588 ± 0.0096	6.1			
3686.830	H I		3686.825	-0.4 ± 0.2	27.1 ± 0.7	0.5463 ± 0.0144	37.9	0.1353 ± 0.0205	C	
			3686.310	-42.3 ± 0.2	28.3 ± 0.0	0.0739 ± 0.0110	6.7			
3691.554	H I		3691.544	-0.8 ± 0.2	26.2 ± 0.6	0.6167 ± 0.0128	48.3	0.1795 ± 0.0233		
			3690.964	-47.9 ± 1.4	27.8 ± 3.5	0.1107 ± 0.0142	7.8			

Table 7.1—Continued

ID Wave ^{a,b}	ID	? ^c	Wavel ^d	Velocity ^e	FWHM ^{e,f}	$I_{\text{corr}}^{\text{g,h}}$	S/N^i	$I_{\text{sh}}/I_{\text{neb}}^j$	Notes ^k
(1)	(2)	(3)	(4)	(5)	(6)	(7)	(8)	(9)	(10)
3694.212	Ne II	?	3694.151	-4.9 ± 1.0	5.1 ± 1.5	0.0173 ± 0.0060	2.9	...	S small FWHM
			
3697.152	H I		3697.156	0.3 ± 0.6	28.6 ± 1.4	0.6467 ± 0.0337	19.2	0.2013 ± 0.0381	C
			3696.637	-41.8 ± 0.6	28.3 ± 0.0	0.1302 ± 0.0237	5.5		
3703.852	H I		3703.850	-0.1 ± 0.2	25.6 ± 0.7	0.6863 ± 0.0198	34.7	0.1652 ± 0.0231	C
			3703.345	-41.0 ± 0.2	28.3 ± 0.0	0.1134 ± 0.0155	7.3		
3705.006	He I		3705.000	-0.5 ± 0.3	18.6 ± 0.7	0.3635 ± 0.0153	23.8	...	S avg
			
3711.971	H I		3711.960	-0.9 ± 0.6	26.3 ± 1.4	1.0106 ± 0.0558	18.1	0.1941 ± 0.0435	C
		?	3711.437	-43.2 ± 0.6	28.3 ± 0.0	0.1962 ± 0.0427	4.6		
3713.080	Ne II	?	3713.057	-1.8 ± 0.7	7.6 ± 1.7	0.0206 ± 0.0044	4.7	...	S small FWHM
			
3721.938	H I		3721.824	-9.1 ± 0.7	38.4 ± 2.0	1.5474 ± 0.0949	16.3	...	S, [S III] line blend
			
3726.032	[O II]		3726.087	4.4 ± 0.1	18.8 ± 0.2	27.4591 ± 0.2373	115.7	0.0455 ± 0.0087	C
		?	3725.511	-41.9 ± 0.1	28.3 ± 0.0	1.2481 ± 0.2400	5.2		
3728.784	[O II]		3728.837	4.3 ± 0.1	20.1 ± 0.2	13.9488 ± 0.1260	110.7	0.0390 ± 0.0091	C
		?	3728.261	-42.1 ± 0.1	28.3 ± 0.0	0.5447 ± 0.1267	4.3		
3734.368	H I		3734.360	-0.6 ± 0.2	26.0 ± 0.4	1.0729 ± 0.0153	69.9	0.1621 ± 0.0170	
			3733.842	-42.2 ± 1.3	34.1 ± 3.6	0.1739 ± 0.0181	9.6		
3750.151	H I		3750.142	-0.7 ± 0.2	26.7 ± 0.3	1.3333 ± 0.0179	74.4	0.1452 ± 0.0104	C
			3749.620	-42.5 ± 0.2	28.3 ± 0.0	0.1936 ± 0.0136	14.2		
3770.630	H I		3770.625	-0.4 ± 0.1	26.5 ± 0.2	2.3596 ± 0.0252	93.6	0.1216 ± 0.0110	avg
			3770.095	-42.5 ± 0.8	28.0 ± 2.3	0.2869 ± 0.0258	11.1		
3781.942	Fe I	?	3781.933	-0.7 ± 2.0	13.8 ± 4.9	0.0114 ± 0.0039	2.9	...	S
			
3784.895	He I		3784.841	-4.3 ± 1.1	14.3 ± 2.8	0.0211 ± 0.0038	5.5	0.2986 ± 0.1197	small FWHM
		?	3784.513	-30.2 ± 1.0	5.7 ± 2.1	0.0063 ± 0.0023	2.8		
3797.898	H I		3797.891	-0.6 ± 0.1	26.6 ± 0.2	2.2831 ± 0.0177	129.1	0.1532 ± 0.0081	
			3797.349	-43.3 ± 0.6	29.2 ± 1.5	0.3498 ± 0.0183	19.1		
3805.777	He I	?	3805.694	-6.5 ± 1.6	15.1 ± 4.0	0.0151 ± 0.0040	3.8	...	S
			
3806.526	Si III	?	3806.482	-3.4 ± 0.9	6.8 ± 1.9	0.0062 ± 0.0017	3.6	...	S small FWHM
			
3819.614	He I		3819.617	0.2 ± 0.2	21.9 ± 0.7	0.4219 ± 0.0132	32.0	0.1714 ± 0.0286	C
			3819.081	-41.9 ± 0.2	28.3 ± 0.0	0.0723 ± 0.0119	6.1		
3833.584	He I	?	3833.532	-4.0 ± 1.2	15.2 ± 3.0	0.0302 ± 0.0063	4.8	...	S
			
3835.384	H I		3835.379	-0.4 ± 0.1	27.2 ± 0.1	4.7665 ± 0.0289	164.7	0.1374 ± 0.0065	avg
			3834.830	-43.3 ± 0.5	28.4 ± 1.3	0.6550 ± 0.0309	21.2		
3837.726	S III	?	3837.787	4.7 ± 0.5	6.7 ± 1.3	0.0102 ± 0.0020	5.0	...	S small FWHM
			
3838.374	N II	?	3838.256	-9.2 ± 2.3	23.7 ± 6.9	0.0251 ± 0.0087	2.9	...	S
			
3856.018	Si II		3856.043	1.9 ± 0.5	20.4 ± 1.2	0.0791 ± 0.0048	16.6	0.2023 ± 0.0575	C
		?	3855.477	-42.1 ± 0.5	28.3 ± 0.0	0.0160 ± 0.0044	3.6		
3862.595	Si II		3862.621	2.0 ± 0.7	18.1 ± 1.7	0.0443 ± 0.0041	10.8	...	S
			
3867.472	He I		3867.495	1.8 ± 0.5	14.5 ± 1.4	0.0313 ± 0.0033	9.5	...	S
			
3868.750	[Ne III]		3868.740	-0.8 ± 0.1	14.0 ± 0.2	8.0485 ± 0.1063	75.7	0.2602 ± 0.0202	
			3868.204	-42.3 ± 0.8	25.4 ± 1.9	2.0946 ± 0.1599	13.1		
3871.790	He I		3871.781	-0.7 ± 0.5	15.4 ± 1.1	0.0370 ± 0.0027	13.8	0.3297 ± 0.0839	C
		?	3871.246	-42.2 ± 0.5	28.3 ± 0.0	0.0122 ± 0.0030	4.1		
3889.049	H I		3889.009	-3.1 ± 0.7	32.8 ± 1.8	6.9463 ± 0.4236	16.4	0.1773 ± 0.0392	C, He I line blend
		?	3888.517	-41.0 ± 0.7	28.3 ± 0.0	1.2317 ± 0.2621	4.7		
3918.968	C II		3918.934	-2.6 ± 0.8	15.3 ± 1.9	0.0243 ± 0.0028	8.6	0.4362 ± 0.1416	C
		?	3918.417	-42.2 ± 0.8	28.3 ± 0.0	0.0106 ± 0.0032	3.3		

Table 7.1—Continued

ID Wave ^{a,b}	ID	? ^c	Wavel ^d	Velocity ^e	FWHM ^{e,f}	$I_{\text{corr}}^{\text{g,h}}$	S/N^i	$I_{\text{sh}}/I_{\text{neb}}^j$	Notes ^k
(1)	(2)	(3)	(4)	(5)	(6)	(7)	(8)	(9)	(10)
3920.681	C II		3920.627	-4.1 ± 0.3	14.4 ± 0.8	0.0490 ± 0.0026	18.5	...	S
				
3926.544	He I		3926.537	-0.5 ± 0.4	18.1 ± 0.9	0.0641 ± 0.0031	20.6	0.2699 ± 0.0508	C
			3925.991	-42.2 ± 0.4	28.3 ± 0.0	0.0173 ± 0.0031	5.5		
3928.556	S III	?	3928.567	0.8 ± 1.8	10.8 ± 4.4	0.0070 ± 0.0027	2.6	...	S
				
3935.945	He I	?	3935.945	0.0 ± 0.8	5.5 ± 2.7	0.0043 ± 0.0014	3.1	...	S small FWHM
				
...		?	3952.737	...	13.7 ± 5.2	0.0075 ± 0.0028	2.7	...	S
				
3964.728	He I		3964.726	-0.2 ± 0.1	17.4 ± 0.3	0.5317 ± 0.0079	67.4	0.1332 ± 0.0158	C avg
			3964.171	-42.1 ± 0.1	28.3 ± 0.0	0.0708 ± 0.0083	8.5		
3967.460	[Ne III]		3967.442	-1.4 ± 0.1	14.5 ± 0.1	3.9684 ± 0.0354	112.0	0.2311 ± 0.0134	avg
			3966.891	-43.0 ± 0.5	24.2 ± 1.2	0.9172 ± 0.0527	17.4		
3970.072	H I		3970.067	-0.4 ± 0.1	26.4 ± 0.1	11.8942 ± 0.0700	170.0	0.1372 ± 0.0069	avg
			3969.510	-42.5 ± 0.4	28.7 ± 1.2	1.6322 ± 0.0816	20.0		
3993.059	[Ni II]	?	3993.258	15.0 ± 1.6	9.9 ± 3.8	0.0069 ± 0.0025	2.8	...	S small FWHM
				
4008.350	[Fe III]		4008.332	-1.4 ± 0.7	9.5 ± 1.6	0.0115 ± 0.0019	6.2	...	S small FWHM
				
4009.256	He I		4009.256	-0.0 ± 0.2	15.7 ± 0.6	0.0684 ± 0.0025	27.4	...	S
				
4023.980	He I	?	4023.934	-3.4 ± 1.5	12.7 ± 3.6	0.0086 ± 0.0023	3.7	...	S
				
4026.184	He I		4026.201	1.3 ± 0.2	19.0 ± 0.6	1.0062 ± 0.0303	33.2	0.2282 ± 0.0308	C
			4025.622	-41.9 ± 0.2	28.3 ± 0.0	0.2296 ± 0.0302	7.6		
4068.600	[S II]		4068.700	7.3 ± 0.1	18.6 ± 0.2	0.7661 ± 0.0076	101.1	0.0470 ± 0.0094	C
		?	4068.031	-41.9 ± 0.1	28.3 ± 0.0	0.0360 ± 0.0072	5.0		
4069.882	O II	?	4069.805	-5.7 ± 1.9	28.7 ± 5.4	0.0306 ± 0.0067	4.6	...	S
				
4072.153	O II		4072.148	-0.3 ± 0.4	13.1 ± 1.1	0.0269 ± 0.0022	12.1	0.2937 ± 0.1077	C
		?	4071.582	-42.1 ± 0.4	28.3 ± 0.0	0.0079 ± 0.0028	2.8		
4075.862	O II		4075.851	-0.8 ± 0.3	14.8 ± 0.9	0.0407 ± 0.0033	12.2	0.2211 ± 0.0640	
		?	4075.292	-41.9 ± 1.4	15.7 ± 4.0	0.0090 ± 0.0025	3.6		
4076.350	[S II]		4076.454	7.7 ± 0.1	17.7 ± 0.3	0.2393 ± 0.0045	53.6	...	S
				
4079.700	[Fe III]	?	4079.659	-3.0 ± 1.0	8.1 ± 2.5	0.0051 ± 0.0015	3.5	...	S small FWHM
				
4083.899	O II	?	4083.854	-3.3 ± 1.5	9.8 ± 3.5	0.0052 ± 0.0017	3.0	...	S small FWHM
				
4085.112	O II	?	4085.105	-0.5 ± 2.2	20.5 ± 5.7	0.0097 ± 0.0027	3.6	...	S
				
4089.288	O II	?	4089.285	-0.2 ± 1.6	11.6 ± 4.0	0.0085 ± 0.0027	3.1	...	S
				
4092.929	O II	?	4092.915	-1.0 ± 0.8	6.8 ± 2.3	0.0060 ± 0.0017	3.6	...	S small FWHM
				
4097.225	O II	?	4097.184	-3.0 ± 3.4	30.7 ± 9.7	0.0243 ± 0.0093	2.6	...	S , O II line blend
				
4101.734	H I		4101.734	0.0 ± 0.1	27.2 ± 0.2	15.5127 ± 0.1098	141.3	0.1306 ± 0.0066	avg
			4101.188	-39.9 ± 0.5	24.2 ± 1.3	2.0266 ± 0.1008	20.1		
4110.786	O II	?	4110.750	-2.7 ± 1.5	9.1 ± 3.6	0.0071 ± 0.0025	2.8	...	S small FWHM
				
4116.104	Si IV	?	4116.225	8.8 ± 0.9	7.2 ± 2.0	0.0038 ± 0.0011	3.6	...	S small FWHM
				
4119.217	O II		4119.198	-1.4 ± 0.9	11.7 ± 2.1	0.0122 ± 0.0020	6.0	0.7377 ± 0.2825	
		?	4118.714	-36.6 ± 3.2	23.2 ± 8.0	0.0090 ± 0.0031	2.9		
4120.811	He I		4120.817	0.5 ± 0.3	19.7 ± 0.8	0.0854 ± 0.0033	25.9	0.2927 ± 0.0387	C
			4120.231	-42.1 ± 0.3	28.3 ± 0.0	0.0250 ± 0.0032	7.9		

Table 7.1—Continued

ID Wave ^{a,b}	ID	? ^c	Wavel ^d	Velocity ^e	FWHM ^{e,f}	$I_{\text{corr}}^{\text{g,h}}$	S/N^i	$I_{\text{sh}}/I_{\text{neb}}^j$	Notes ^k
(1)	(2)	(3)	(4)	(5)	(6)	(7)	(8)	(9)	(10)
4387.929	He I		4387.925	-0.3 ± 0.1	19.2 ± 0.2	0.2463 ± 0.0026	93.1	0.1750 ± 0.0134	
			4387.323	-41.4 ± 0.9	27.7 ± 2.3	0.0431 ± 0.0033	13.2		
4391.995	Ne II	?	4391.896	-6.7 ± 1.6	20.3 ± 4.2	0.0083 ± 0.0017	4.9	...	S
				
4413.781	[Fe II]		4413.963	12.4 ± 0.5	15.9 ± 1.3	0.0241 ± 0.0020	11.9	...	S
				
4414.899	O II		4414.895	-0.3 ± 0.5	12.1 ± 1.3	0.0125 ± 0.0013	9.8	...	S
				
4416.266	[Fe II]		4416.441	11.9 ± 0.3	13.5 ± 1.0	0.0284 ± 0.0025	11.4	...	S
				
4425.437	Ca I	?	4425.578	9.6 ± 2.0	12.9 ± 5.0	0.0040 ± 0.0015	2.7	...	S
				
4437.554	He I		4437.568	0.9 ± 0.6	20.4 ± 1.5	0.0373 ± 0.0031	11.9	...	S avg
				
4452.378	O II		4452.293	-5.7 ± 0.5	13.8 ± 1.1	0.0169 ± 0.0013	12.6	0.2189 ± 0.0667	
		?	4451.910	-31.5 ± 1.4	10.7 ± 3.5	0.0037 ± 0.0011	3.4		
4457.945	[Fe II]		4458.151	13.9 ± 1.4	23.4 ± 3.7	0.0140 ± 0.0023	6.1	...	S
				
4465.407	O II	?	4465.357	-3.3 ± 1.7	18.9 ± 4.4	0.0074 ± 0.0017	4.4	...	S
				
4471.489	He I		4471.492	0.2 ± 0.1	20.7 ± 0.4	1.9679 ± 0.0359	54.8	0.1637 ± 0.0229	
			4470.874	-41.3 ± 1.4	26.8 ± 3.7	0.3221 ± 0.0447	7.2		
4474.904	[Fe II]	?	4475.097	13.0 ± 1.1	10.4 ± 3.0	0.0053 ± 0.0017	3.1	...	S
				
4514.900	[Fe II]	?	4515.015	7.6 ± 2.1	17.1 ± 5.3	0.0058 ± 0.0018	3.3	...	S
				
4571.096	Mg I]	?	4571.182	5.6 ± 2.9	19.0 ± 7.3	0.0038 ± 0.0015	2.6	...	S
				
4590.974	O II		4590.960	-0.9 ± 1.0	17.4 ± 2.5	0.0104 ± 0.0014	7.2	0.4423 ± 0.1597	C
		?	4590.325	-42.4 ± 1.0	28.3 ± 0.0	0.0046 ± 0.0015	3.0		
4596.177	O II	?	4596.120	-3.7 ± 0.8	10.0 ± 2.5	0.0055 ± 0.0015	3.6	...	S
				
4596.840	[Ni III]	?	4597.071	15.1 ± 1.2	7.5 ± 3.1	0.0028 ± 0.0011	2.6	...	S small FWHM
				
4607.030	[Fe III]		4607.102	4.7 ± 0.5	17.7 ± 1.3	0.0303 ± 0.0021	14.3	0.2508 ± 0.0780	C
		?	4606.383	-42.1 ± 0.5	28.3 ± 0.0	0.0076 ± 0.0023	3.3		
4609.436	O II	?	4609.386	-3.3 ± 1.2	7.6 ± 2.8	0.0056 ± 0.0019	2.9	...	S small FWHM
				
4621.418	Si II	?	4621.186	-15.1 ± 2.4	23.1 ± 6.1	0.0087 ± 0.0022	3.9	...	S
				
4630.539	N II		4630.539	-0.0 ± 0.8	17.7 ± 2.0	0.0197 ± 0.0022	9.0	0.5685 ± 0.1321	C
		?	4629.893	-41.9 ± 0.8	28.3 ± 0.0	0.0112 ± 0.0023	4.9		
4634.130	N III	?	4634.073	-3.7 ± 1.1	7.6 ± 2.6	0.0032 ± 0.0011	3.0	...	S small FWHM
				
4638.856	O II		4638.830	-1.7 ± 0.7	16.0 ± 1.7	0.0184 ± 0.0019	9.8	0.4620 ± 0.1247	C
		?	4638.200	-42.4 ± 0.7	28.3 ± 0.0	0.0085 ± 0.0021	4.0		
4641.810	O II		4641.803	-0.5 ± 0.3	13.8 ± 0.6	0.0320 ± 0.0012	25.7	0.2625 ± 0.0480	C
			4641.159	-42.1 ± 0.3	28.3 ± 0.0	0.0084 ± 0.0015	5.6		
4643.086	N II	?	4643.102	1.1 ± 0.9	10.3 ± 2.2	0.0049 ± 0.0010	5.1	...	S
				
4649.135	O II		4649.126	-0.5 ± 0.2	15.1 ± 0.5	0.0524 ± 0.0016	32.2	0.4046 ± 0.0554	
			4648.520	-39.7 ± 1.6	33.4 ± 4.4	0.0212 ± 0.0028	7.5		
4650.838	O II		4650.828	-0.7 ± 0.4	14.9 ± 1.0	0.0186 ± 0.0011	16.5	0.4516 ± 0.0825	C
			4650.184	-42.2 ± 0.4	28.3 ± 0.0	0.0084 ± 0.0014	5.8		
4658.050	[Fe III]		4658.156	6.8 ± 0.1	16.9 ± 0.3	0.3503 ± 0.0062	56.9	0.1818 ± 0.0211	
			4657.476	-36.9 ± 1.0	21.6 ± 2.5	0.0637 ± 0.0073	8.7		
4661.632	O II		4661.629	-0.2 ± 0.3	14.6 ± 0.6	0.0206 ± 0.0009	23.5	0.2087 ± 0.0435	
		?	4660.854	-50.1 ± 1.3	15.1 ± 3.2	0.0043 ± 0.0009	4.9		

Table 7.1—Continued

ID Wave ^{a,b}	ID	? ^c	Wavel ^d	Velocity ^e	FWHM ^{e,f}	$I_{\text{corr}}^{\text{g,h}}$	S/N^i	$I_{\text{sh}}/I_{\text{neb}}^j$	Notes ^k
(1)	(2)	(3)	(4)	(5)	(6)	(7)	(8)	(9)	(10)
5577.339	[O I]		5577.607	14.4 ± 0.8	16.3 ± 2.2	0.0046 ± 0.0007	6.7	...	B S
				
5577.339	[O I]	?	5577.611	14.6 ± 0.7	8.8 ± 1.7	0.0039 ± 0.0008	4.7	...	R S avg small FWHM
				
5606.151	S II	?	5606.186	1.9 ± 1.5	9.7 ± 3.6	0.0015 ± 0.0005	2.9	...	B S small FWHM
				
5666.630	N II		5666.613	-0.9 ± 0.9	21.4 ± 2.2	0.0115 ± 0.0011	10.2	0.2957 ± 0.0850	R C
		?	5665.827	-42.5 ± 0.9	28.3 ± 0.0	0.0034 ± 0.0009	3.7		
5676.020	N II	?	5676.053	1.7 ± 1.4	15.1 ± 3.3	0.0063 ± 0.0015	4.1	...	R S avg
				
5679.560	N II		5679.578	0.9 ± 1.2	24.9 ± 3.0	0.0177 ± 0.0022	8.0	...	B S
				
5679.560	N II		5679.551	-0.5 ± 0.4	17.2 ± 0.9	0.0171 ± 0.0009	20.0	0.1342 ± 0.0468	R C
		?	5678.749	-42.8 ± 0.4	28.3 ± 0.0	0.0023 ± 0.0008	2.9		
5686.210	N II	?	5686.020	-10.0 ± 2.3	28.0 ± 6.3	0.0051 ± 0.0012	4.4	0.5333 ± 0.1827	R C
		?	5685.222	-52.1 ± 2.3	28.3 ± 0.0	0.0027 ± 0.0007	3.9		
5710.770	N II	?	5710.778	0.4 ± 0.8	5.7 ± 1.5	0.0014 ± 0.0004	3.6	...	B S small FWHM
				
5710.770	N II		5710.775	0.3 ± 0.6	11.6 ± 1.5	0.0047 ± 0.0006	8.1	0.4160 ± 0.1572	R C
		?	5709.956	-42.7 ± 0.6	28.3 ± 0.0	0.0020 ± 0.0007	2.8		
5739.730	Si III		5739.687	-2.3 ± 0.7	14.4 ± 1.8	0.0056 ± 0.0007	8.4	0.5536 ± 0.1565	B C
		?	5738.923	-42.2 ± 0.7	28.3 ± 0.0	0.0031 ± 0.0008	3.9		
5739.730	Si III		5739.731	0.1 ± 0.7	9.7 ± 1.8	0.0036 ± 0.0006	5.7	0.8736 ± 0.2625	R C small FWHM
		?	5738.907	-43.0 ± 0.7	28.3 ± 0.0	0.0031 ± 0.0008	4.1		
5754.590	[N II]		5754.724	7.0 ± 0.1	19.9 ± 0.2	0.3248 ± 0.0028	117.1	0.0443 ± 0.0084	B C
			5753.784	-42.0 ± 0.1	28.3 ± 0.0	0.0144 ± 0.0027	5.3		
5754.590	[N II]		5754.735	7.6 ± 0.1	20.1 ± 0.2	0.3225 ± 0.0034	95.1	0.0448 ± 0.0090	R C
		?	5753.769	-42.8 ± 0.1	28.3 ± 0.0	0.0145 ± 0.0029	5.0		
5867.600	Al II	?	5867.875	14.0 ± 1.4	11.4 ± 3.3	0.0027 ± 0.0007	3.8	0.8148 ± 0.3534	B
		?	5866.962	-32.6 ± 1.9	12.5 ± 4.7	0.0022 ± 0.0008	2.9		
5875.640	He I		5875.652	0.6 ± 0.2	23.7 ± 0.3	5.7619 ± 0.0713	80.8	0.1604 ± 0.0130	B
			5874.831	-41.3 ± 0.9	25.3 ± 2.3	0.9243 ± 0.0739	12.5		
5875.640	He I		5875.648	0.4 ± 0.2	21.6 ± 0.3	5.7021 ± 0.0735	77.6	0.1686 ± 0.0124	R
			5874.833	-41.2 ± 0.9	26.7 ± 2.2	0.9616 ± 0.0697	13.8		
...			5887.613	...	14.2 ± 2.4	0.0048 ± 0.0008	6.2	...	B S
				
5889.280	C II		5889.334	2.8 ± 0.3	13.1 ± 0.7	0.0160 ± 0.0011	15.2	...	B S
				
...		?	5906.023	...	28.3 ± 6.1	0.0054 ± 0.0012	4.6	0.2593 ± 0.1113	B small FWHM
		?	5905.154	...	8.1 ± 3.2	0.0014 ± 0.0005	2.7		
5927.810	N II	?	5927.791	-1.0 ± 1.6	12.3 ± 3.8	0.0021 ± 0.0006	3.5	...	R S
				
5931.780	N II	?	5931.848	3.5 ± 1.1	7.1 ± 2.5	0.0028 ± 0.0009	3.0	...	B S small FWHM
				
5931.780	N II		5931.942	8.2 ± 1.7	29.2 ± 4.6	0.0102 ± 0.0016	6.2	...	R S
				
5952.390	N II	?	5952.523	6.7 ± 1.4	15.2 ± 3.3	0.0050 ± 0.0011	4.7	...	R S
				
5957.560	Si II		5957.739	9.0 ± 0.5	23.0 ± 1.8	0.0187 ± 0.0020	9.3	...	R S avg
				
5958.386	O I		5958.831	22.4 ± 0.3	18.4 ± 0.9	0.0146 ± 0.0007	19.6	...	R S avg , O I line blend
				
5978.930	Si II		5979.095	8.3 ± 0.5	24.6 ± 1.1	0.0464 ± 0.0021	22.4	...	S avg
				
6046.438	O I		6046.681	12.1 ± 0.2	18.5 ± 0.5	0.0406 ± 0.0010	39.0	...	S , O I line blend
				
6300.304	[O I]		6300.578	13.0 ± 0.1	15.1 ± 0.1	0.3954 ± 0.0035	112.1	0.0413 ± 0.0098	C avg
		?	6299.405	-42.8 ± 0.1	28.3 ± 0.0	0.0163 ± 0.0039	4.2		sky line

Table 7.1—Continued

ID Wave ^{a,b}	ID	? ^c	Wavel ^d	Velocity ^e	FWHM ^{e,f}	I_{corr} ^{g,h}	S/N ⁱ	I_{sh}/I_{neb} ^j	Notes ^k
(1)	(2)	(3)	(4)	(5)	(6)	(7)	(8)	(9)	(10)
7377.830	[Ni II]		7378.183	14.3 ± 0.1	17.2 ± 0.3	0.0402 ± 0.0007	54.8	...	S avg
			
7388.180	[Fe II]		7388.446	10.8 ± 1.1	24.4 ± 3.0	0.0061 ± 0.0008	8.1	...	S
			
7411.610	[Ni II]	?	7411.910	12.1 ± 1.3	12.4 ± 3.6	0.0141 ± 0.0043	3.3	...	S
			
7423.641	N I		7424.035	15.9 ± 0.4	13.3 ± 0.9	0.0067 ± 0.0004	15.9	...	S
			
7468.312	N I		7468.687	15.0 ± 0.2	11.9 ± 0.4	0.0183 ± 0.0006	32.5	...	S
			

^aID wavelength of line, in air. Wavelengths are from the Atomic Line List v2.04 (<http://www.pa.uky.edu/~peter/atomic/>, maintained by P. A. M. van Hoof), except O II (Chapter 5).

^bNebular (neb) and shock (sh) components are included in separate, consecutive rows for each ID wavelength. If there is no shock component, the second row is left blank. Lines with no identification are included, but columns (1), (2) and (5) are left blank.

^cA low S/N ($2.6 < S/N < 5.2$) is flagged with a ‘?’

^dObserved wavelength of line peak adjusted to rest frame of nebular H^+ as defined by median of first six unblended H I Balmer lines
^ekm s⁻¹

^fA quoted FWHM of 28.3 ± 0.0 is the result of a constrained double Gaussian fit.

^gReddening-corrected surface brightness (I_{corr} , 10^{-13} ergs cm⁻² s⁻¹ arcsec⁻²) and its uncertainty calculated from the best-fit Gaussian area and its 68.3% confidence interval.

^hThe red shock lines have been adjusted by a factor of 0.85 to correct for slit coverage differences between the red and blue spectra. The nebular lines are not adjusted.

ⁱSignal-to-noise from surface brightness and 68.3% confidence interval.

^jThe shock-to-nebula ratio is entered within the ‘nebula’ row and the ‘shock’ row is left blank.

^kConstrained double Gaussian fit (C), constrained triple Gaussian fit (T), single Gaussian fit (S), red echelle spectrum (R), blue echelle spectrum (B), average of two orders (avg).

The shock component can be seen most prominently in the medium-ionization forbidden lines (e.g., [O III]), as well as in the He I and H I permitted lines. Although the shock component can also be seen in the low-ionization lines ([O II] and [N II]), its strength relative to the nebular line is much weaker (see col. (9) of Table 7.1). Of lines normally associated with the ionization front (IF) of photoionized gas, some ([S II]) can be seen very weakly in the shock component, whereas others ([N I]) are too weak to be detected. As will be discussed, the presence of [S II] does not imply an IF in the shock.

Unfortunately, the [O I] sky lines³ lie close to the wavelength where the shock component would be. Using a triple-Gaussian fit for the nebula, shock and sky components, we can determine if there is a detectable shock component for the [O I] $\lambda 6300$ line. The sky line FWHM, wavelength, and area constraints are set by the sky line in the 1SW echelle spectrum taken on the same evening; the shock is constrained as in the constrained double-Gaussian case. Following the fit of the three components in [O I] $\lambda 6300$, the shock component has a null detection ($S/N \ll 2.6$) lying well below our detection limit. Neither is there a detectable bridge

³These lines are identified as such from sky spectra and other nebular spectra (at positions which did not have a velocity-shifted feature) that were taken on the same evening.

component as seen with the other shock lines. It can be safely said that [O I] (as with [N I]) line emission in the shock lies below the detection limit for these spectra (i.e., $S/N < 2.6$).

At first sight this seemed at odds with the BOM00 HH 529 [O I] observations depicted in their Figure 6 (WFPC2 631N image and Keck HIRES spectrum). However, their detection of [O I] with the 631N filter is not definitive due to contamination from the [S III] line ($\lambda 6312$) (O’Dell & Doi, 1999). BOM00’s original HIRES spectrum shows a strong [S III] velocity-shifted feature ($v \sim -39 \text{ km s}^{-1}$) associated with the eastern-most shock of HH 529 (C. R. O’Dell 2005, private communication). We also detect this in our spectrum and have determined quantitatively that [S III] would explain the presence of the shock in the WFPC2 631N image. Furthermore, the [O I] velocity contour plot displayed in BOM00 Figure 6 is actually an inadvertent copy of the [O III] plot (C. R. O’Dell 2005, private communication). The correct [O I] contours are similar to the [S II] contours in the west but have no velocity-shifted feature in the east.

7.1.1 Blue/red line strengths

Since the red and the blue spectra were taken on different nights, there is a slight pointing uncertainty (see Fig. 7.2) which makes comparison between the red and blue spectra more difficult. To study the uncertainties involved in inter-spectral comparison, we identified lines that are found in both the red and blue spectra. Six such lines had both a nebular and a measurable shock component ([Fe III] $\lambda 5270$, [Cl III] $\lambda 5518$, [Cl III] $\lambda 5538$, Si III $\lambda 5740$, [N II] $\lambda 5755$, and He I $\lambda 5876$). Table 7.2 summarizes the results from the (constrained) double-Gaussian line-fitting for these seven lines prior to applying the reddening correction. The blue/red ratios for the nebular and shock components are each shown separately in column (8) of Table 7.2, in the same rows as the blue results.

The nebular lines measured from the blue spectrum are not any stronger than the red on average ($B/R_{avg}^{weighted} \sim 1.02 \pm 0.04$). However, the average blue/red ratio ($B/R_{avg}^{weighted} \sim 0.85 \pm 0.04$) indicates otherwise for the shock. This difference in blue/red ratios is not unexpected, as there is no reason to expect a correlation between surface brightnesses in the nebula and shock. Using these results, we make an across-the-board adjustment to all the red shock lines such that the shock line strengths match between the red and blue (0.85 adjustment) – allowing for a complete (blue/red) analysis of the shock. No such correction is made to the nebular feature, whose blue/red ratio is consistent with 1.0.

7.1.2 Reddening

It is expected that the reddening of both the nebular and shock components is the same, being dominated by foreground material. However, prior to making the correction discussed in

Table 7.2. Blue/red echelle spectra comparison.

ID Wave (1)	ID (2)	Wavel (3)	Velocity (4)	FWHM (5)	I_{obs}^a (6)	S/N (7)	B/R^b (8)	Notes (9)
5270.400	[Fe III]	5270.550	8.5 ± 0.1	17.0 ± 0.3	0.0248	57.5	1.051 ± 0.026	B avg
		5269.821	-32.9 ± 1.1	25.6 ± 2.9	0.0055	9.7	0.846 ± 0.115	
5270.400	[Fe III]	5270.555	8.8 ± 0.1	16.1 ± 0.3	0.0236	56.6	...	R
		5269.840	-31.9 ± 1.1	27.6 ± 2.7	0.0065	11.2	...	
5517.720	[Cl III]	5517.686	-1.9 ± 0.2	15.6 ± 0.4	0.0250	39.4	1.232 ± 0.048	B C
		5516.948	-42.0 ± 0.2	28.3 ± 0.0	0.0030	4.2	0.789 ± 0.237	
5517.720	[Cl III]	5517.697	-1.3 ± 0.2	14.9 ± 0.5	0.0203	33.8	...	R C
		5516.925	-43.2 ± 0.2	28.3 ± 0.0	0.0038	5.5	...	
5537.890	[Cl III]	5537.863	-1.5 ± 0.1	18.8 ± 0.2	0.0345	95.9	1.015 ± 0.015	B
		5537.118	-41.8 ± 0.7	26.0 ± 1.8	0.0069	15.8	0.896 ± 0.085	
5537.890	[Cl III]	5537.849	-2.2 ± 0.1	16.0 ± 0.2	0.0340	90.6	...	R avg
		5537.071	-44.4 ± 0.8	27.8 ± 2.1	0.0077	14.3	...	
5739.730	Si III	5739.687	-2.3 ± 0.7	14.4 ± 1.8	0.0009	8.4	1.500 ± 0.318	B C
		5738.923	-42.2 ± 0.7	28.3 ± 0.0	0.0005	3.9	0.833 ± 0.295	
5739.730	Si III	5739.731	0.1 ± 0.7	9.7 ± 1.8	0.0006	5.7	...	R C
		5738.907	-43.0 ± 0.7	28.3 ± 0.0	0.0006	4.1	...	
5754.590	[N II]	5754.724	7.0 ± 0.1	19.9 ± 0.2	0.0545	117.1	1.006 ± 0.014	B C
		5753.784	-42.0 ± 0.1	28.3 ± 0.0	0.0024	5.3	0.828 ± 0.228	
5754.590	[N II]	5754.735	7.6 ± 0.1	20.1 ± 0.2	0.0542	95.1	...	R C
		5753.769	-42.8 ± 0.1	28.3 ± 0.0	0.0029	5.0	...	
5875.640	He I	5875.652	0.6 ± 0.2	23.7 ± 0.3	0.9977	80.8	1.010 ± 0.018	B
		5874.831	-41.3 ± 0.9	25.3 ± 2.3	0.1600	12.5	0.817 ± 0.088	
5875.640	He I	5875.648	0.4 ± 0.2	21.6 ± 0.3	0.9874	77.6	...	R
		5874.833	-41.2 ± 0.9	26.7 ± 2.2	0.1959	13.8	...	

^a 10^{-13} ergs cm⁻² s⁻¹ arcsec⁻², before reddening correction

^bThe blue/red ratio (B/R) is entered in the ‘blue’ rows for the nebula (1st row) and the shock (2nd row). The ‘red’ rows are left blank.

§ 7.1.1, the nebula and shock had drastically different $H\alpha/H\beta$ Balmer decrements: 4.99 ± 0.04 and 6.72 ± 0.32 , respectively. After adjusting the line strengths so there is congruity between the red and blue lines (§ 7.1.1) in the red and blue spectra and accounting for that uncertainty, these values become 5.1 ± 0.1 and 5.7 ± 0.4 for the nebula and shock, respectively. This justifies the use of the blue/red correction in § 7.1.1 and the use of the same reddening correction for both nebula and shock: $C_{H\beta} = 0.8847$. See Chapter 3 for a discussion on how $C_{H\beta}$ is determined (and how, from this, the data are corrected for reddening.) The dereddened values are included in column (7) of Table 7.1.

7.2 Analysis

7.2.1 Velocity

Figure 7.6 plots all the velocities determined from the shock components of the Gaussian fits. They are quite consistent, as expected, since unlike the expanding nebular gas, there should be no velocity gradient in the shocked gas. The shocked H I lines are shifted by -42.1 ± 1.2 km s⁻¹ relative to the nebular H I lines (see Table 7.1 and Fig. 7.6), or -54.1 ± 1.2 km s⁻¹ relative to the PDR in the molecular cloud, and hence, relative to the outflow source embedded within the cloud. This agrees with the radial velocity measurements made by Doi et al. (2004) for the roughly coincident position 167-359 HH 529: -52 to -54 km s⁻¹ relative to the PDR/OMC-1.

The [Fe III] $\lambda 5270$ shock component (with $S/N \sim 10$) appears to be discrepant in Fig. 7.6, with velocities of -32.9 ± 1.1 (blue) and -31.9 ± 1.1 km s⁻¹ (red). This anomaly has an impact on the apparent nebular velocity gradient of [Fe III] lines (see Fig. 10 in Baldwin et al., 2000) and is taken up in § 7.3.

7.2.2 Temperature and density

Temperatures (in K) and densities (in cm⁻³) are calculated from emission line ratios using the NEBULAR routines included within the IRAF STSDAS package. These are summarized in Table 7.3, with the respective transition probabilities (A) and collision strengths (cs) used in the calculations.

The $T_e([\text{O III}])$ and $T_e([\text{N II}])$ diagnostic lines can be seen in both the nebula and the shock, while the [O I] temperature diagnostic lines can be seen only in the nebula. The nebula temperature from the blue [O III] lines is $T_e^{\text{neb}}([\text{O III}]) \sim 8536_{-33}^{+35}$, whereas for the red [N II] lines, the temperature is higher, $T_e^{\text{neb}}([\text{N II}]) \sim 10672_{-52}^{+53}$. Although these temperatures come from the blue and red spectra respectively and therefore represent two slightly different lines of sight, the temperature rise with depth in the nebula is what is generally seen for other lines

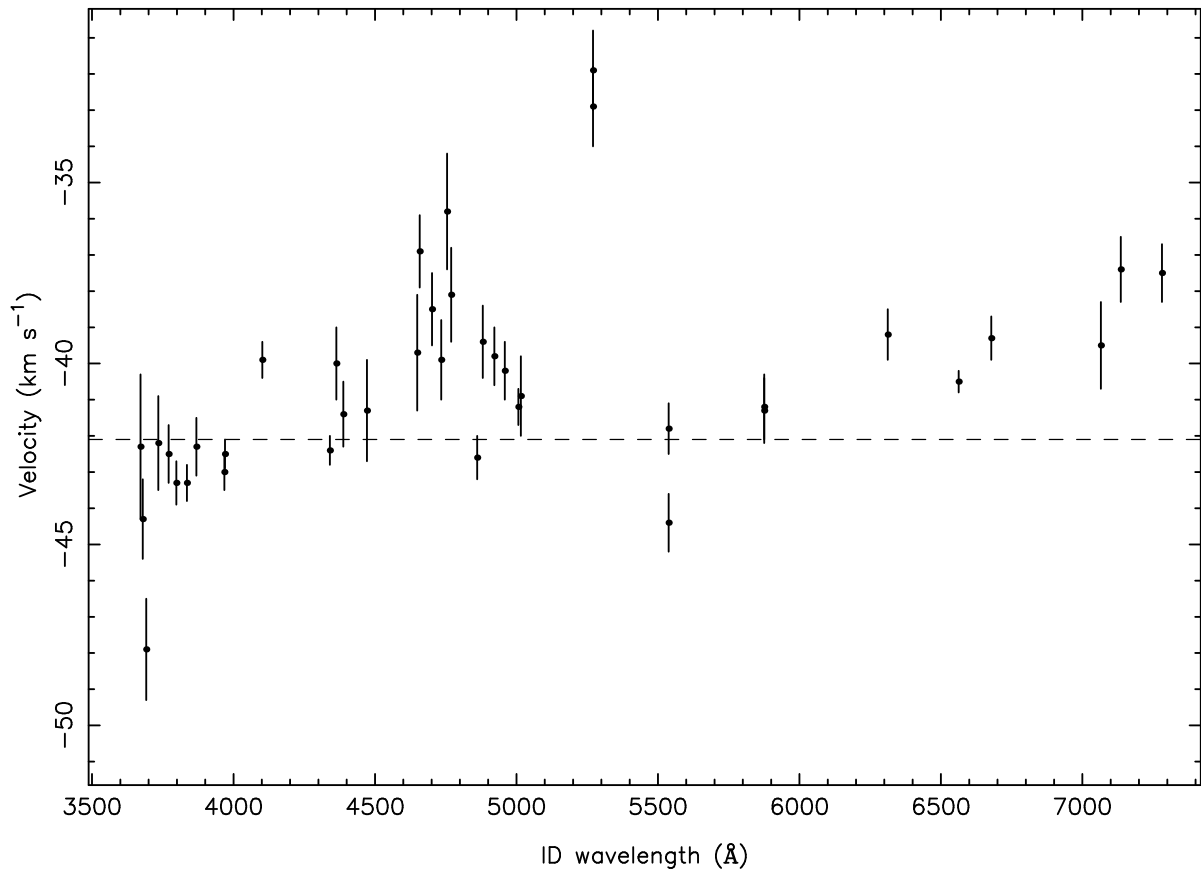


Figure 7.6 Measured velocity of shock component (with respect to nebular H I recombination lines) for high S/N ($S/N > 5.2$) lines from unconstrained double Gaussian fit with 1σ confidence interval determined from the fit. Constrained double Gaussian velocities (-42.1 km s^{-1}) are not plotted individually, but are represented by the horizontal dashed line. The anomalous [Fe III] 5270.4 velocity is discussed in § 7.2.1.

Table 7.3. Physical conditions within the nebula and the shock

Parameter	Line	Nebula	Shock
N_e (cm^{-3})	[S II] ^a	5896^{+404}_{-366}	13183^{+10000}_{-11183}
	[O II] ^b	1939^{+50}_{-50}	2898^{+8429}_{-1997}
	[O II] ^c	3811^{+50}_{-50}	7304^{+8429}_{-1997}
	[Fe III] ^d	4700^{+800}_{-800}	7300^{+8000}_{-4100}
	[Cl III] ^e	12074^{+1300}_{-1118}	21715^{+39170}_{-9641}
	[Cl III] ^f	7247^{+575}_{-519}	10911^{+7515}_{-3665}
	O II ^g	6700^{+100}_{-100}	...
T_e (K)	[O I] ^h	8005^{+580}_{-408}	...
	[N II] ⁱ	10672^{+53}_{-52}	8784^{+1184}_{-729}
	[O III] ^j	8536^{+35}_{-33}	8366^{+252}_{-214}

^aA: Keenan et al. (1993) cs: Ramsbottom et al. (1996)

^bA: Wiese et al. (1996) cs: McLaughlin & Bell (1993)

^cA: Zeppen (1982) cs: McLaughlin & Bell (1993)

^dWeighted average from 11 [Fe III] lines, following Keenan et al. (2001)

^eA: Kaufman & Sugar (1986) cs: Ramsbottom et al. (1999)

^fA: Mendoza & Zeppen (1982) cs: Ramsbottom et al. (1999)

^gFollowing Peimbert & Peimbert (2005)

^hA: Wiese et al. (1996) cs: Bhatia & Kastner (1995)

ⁱA: Wiese et al. (1996) cs: Lennon & Burke (1994)

^jA: Wiese et al. (1996) cs: Lennon & Burke (1994)

of sight, and is largely the result of a hardening of the radiation field as photons close to the ionization limit are attenuated preferentially. To complete the nebular temperature analysis, we have found $T_e^{\text{neb}}([\text{O I}]) \sim 8005_{-408}^{+580}$.

In the shock, the lines are weaker (in the case of $[\text{N II}]$, much weaker) and therefore the calculated temperatures have much larger uncertainties. The $[\text{O III}]$ temperature is 8366_{-214}^{+252} , and that found from the $[\text{N II}]$ temperature diagnostic lines is consistent (within 1σ): 8784_{-729}^{+1184} . Since the shock is matter-bounded (see § 7.2.3), O^{++} ($[\text{O III}]$) and N^+ ($[\text{N II}]$) are not distinct zones and the attenuation seen in the nebula is not possible.

The electron density can be calculated from the diagnostic lines ($[\text{O II}] \lambda\lambda 3726, 3729$; $[\text{S II}] \lambda\lambda 6716, 6731$; $[\text{Cl III}] \lambda\lambda 5517, 5537$), which are seen in the nebula and weakly in the shock. In the nebula these three sets of density diagnostic lines cover different ionization zones along a particular line of sight, but in the shock – because of the lack of distinct ionization zones – the densities are expected to characterize the same zone. However, because of the disparity between red and blue slit positions, the calculated densities are also being defined along slightly different lines of sight.

For the nebula, we get $N_e^{\text{neb}}([\text{O II}]) \sim 1939_{-50}^{+50}$ ($N_e^{\text{neb}}([\text{O II}]) \sim 2164$ using entire slit) from the blue $[\text{O II}]$ lines. The red $[\text{S II}]$ lines yield a much higher density, $N_e^{\text{neb}}([\text{S II}]) \sim 5896_{-366}^{+404}$ ($N_e^{\text{neb}}([\text{S II}]) \sim 5638$ using entire slit), and the $[\text{Cl III}]$ lines yield an even higher density, $N_e^{\text{neb}}([\text{Cl III}]) \sim 12074_{-1118}^{+1300}$.

It has been noted in Esteban et al. (2004) and Wang et al. (2004) that the use of Zeippen (1982) transition probabilities and Pradhan (1976) collisions strengths drastically increases the calculated $N_e([\text{O II}])$. On further investigation, we find that a change in the transition probabilities alone will bring about the same result. Using these older atomic data, we almost double the measured density: $N_e^{\text{neb}}([\text{O II}]) \sim 3811$, bringing it more in line with the densities as measured from other indicators. Another reason for questioning the atomic data comes from the $[\text{O II}]$ temperature – which we overestimate slightly due to the shocked component impinging on the nebular component in the line pairs at 7320 and 7330 Å. Using the density as calculated from $[\text{O II}] \lambda 3726/\lambda 3729$ (2000 cm^{-3}), $T_e^{\text{neb}}([\text{O II}]) \sim 20000 \text{ K}$. However, with the larger density (4000 cm^{-3}) and the old atomic data, $T_e^{\text{neb}}([\text{O II}]) \sim 15000 \text{ K}$. An even larger density is required to reduce the temperature to 10000 K. Note that these densities from $[\text{O II}]$ and $[\text{S II}]$ are probably larger than in the more relevant $[\text{O III}]$ zone, because of a falloff of density in the expanding gas. A similar result appears when we use older transition probability data for the $N_e([\text{Cl III}])$ calculation. The density is reduced to a more consistent value: $N_e^{\text{neb}}([\text{Cl III}]) \sim 7247_{-519}^{+575}$. To round out our discussion of density, we have looked at the density dependence of $[\text{Fe III}]$ (following Keenan et al., 2001) and O II (following Peimbert & Peimbert, 2005) lines. The results are consistent with the densities we see in the rest of the

nebula: $N_e^{\text{neb}}([\text{Fe III}]) \sim 4700_{-800}^{+800}$ and $N_e^{\text{neb}}(\text{O II}) \sim 6700_{-100}^{+100}$.

The density of the shock is also calculated, but as the low-ionization lines are weak, this calculated density is very uncertain. The blue [O II] lines yield $N_e^{\text{sh}}([\text{O II}]) \sim 2898_{-1997}^{+8429}$, the red [S II] lines yield a density near the limits of this diagnostic ratio, $N_e^{\text{sh}}([\text{S II}]) \sim 13183_{-11183}^{+10000}$, [Cl III] lines yield $N_e^{\text{sh}}([\text{Cl III}]) \sim 21715_{-9641}^{+39170}$, and the [Fe III] lines yield⁴ $N_e^{\text{sh}}([\text{Fe III}]) \sim 7300_{-4100}^{+8000}$. (The O II lines are too weak to yield a consistent estimate of the shock density.) Use of the older atomic data again results in a higher [O II] density, $N_e^{\text{sh}}([\text{O II}]) \sim 7304$, and a lower [Cl III] density, $N_e^{\text{sh}}([\text{Cl III}]) \sim 10911$. The shock density appears to be larger (by roughly a factor of 2) than that of the nebula, but given the large uncertainties, a density identical to that of the nebula is also allowed by the line ratios. Density will be revisited in a discussion of shock models in § 7.4.

7.2.3 Relative line strengths and ionization structure

To maximize the shock-to-nebula ratio, the echelle spectra were extracted over only half the slit. Even then, the echelle spectra maintain a weaker shock component as compared to the nebular component (see col. (9) of Table 7.1), indicative of a lower density, or more probably, a shorter emitting column in the shock. Since the illumination of the shock is roughly the same as that of the nebula, if the shock were optically thick, the shock-to-nebula ratio would be close to one for all lines, barring minor changes due to differences in density (near the critical density) or changes due to abundance (see § 7.5). Here, the shock-to-nebula ratio is clearly lower than one, and so the shock is matter bounded.

The relative strength varies from 0.2 for the medium-ionization lines (e.g., [O III]) to less than 0.03 for the low-ionization lines (e.g., [N II]) to below the detection limit for the lines usually associated with the ionization front (e.g., [N I]) and is plotted as a function of ionization potential in Figure 7.7. In the case of a shortened emitting column, the ionization potential serves as an indicator of ionization fraction (where higher ionization potential indicates higher ionization fraction), while the shock-to-nebula ratio is a measure of the optical thickness of the shock to the relevant ionizing radiation. H I is presented as a standard for shock/nebula ionization comparison as its originating ion (H^+) has an ionization fraction of roughly one throughout both the shock and the nebula. The ratios of the medium-ionization species ([O III], [Ar III], and [Ne III]) all lie above H I as they have a higher net ionization fraction in the shock than in the nebula column. However, none of these ratios is unity either. Thus, for example, in the shock there is not a complete O^{++} zone, preceding a distinct O^+ zone. The ratios of the

⁴The lower limit is set using [Fe III] 4986 which is not observed in the shock. This indicates that I_{4986} is below the detection limit ($I_\lambda/I_{6678} \sim 0.01$, or $I_\lambda/I_{4658} \sim 0.05$), resulting in a minimum density of 3200 (Keenan et al., 2001).

low-ionization species ([O II], [N II], and [S II]) lie below H I as they have a lower ionization fraction in the shock than in the nebula. In fact, they must arise from trace ionization stages in a more highly ionized zone (e.g., trace O^+ in the O^{++} zone). This is in contrast to the nebular column in which lines arise from distinct ionization zones. The lack of an ionization front tracer ([N I]) in the shock component provides further corroboration for a matter-bounded shock.

The critical densities associated with the [O II], [S II] and [Cl III] line transitions need to be considered as these lie within the expected density range of the shock and so collisional de-excitation could contribute to the relative weakness of the shock lines. However, the weak [N II] lines have critical densities of 7.8×10^4 and $1.2 \times 10^7 \text{ cm}^{-3}$, which lie well above the model-predicted density as discussed in § 7.4. The predominant cause of weakness is the lack of parent ions in this highly ionized matter-bounded geometry.

7.2.4 Temperature fluctuations

Temperature fluctuations (t^2), first defined/introduced by Peimbert (1967), have been popular in explaining the differences in abundances found from forbidden lines as compared to those found from permitted lines. Although these fluctuations have been deduced to exist, their deduced size ($t^2 \sim 0.02$) has not been explained. Ferland (2001) has suggested a possible link with additional photoelectric heating from grains. Other suggestions – large scale variations in T_e , or the presence of regions either shielded from direct illumination by θ^1 Ori C or heated by shocks (from SNe mainly) – might explain temperature fluctuations in the nebula, but not in a small-scale shock.

O II permitted and [O III] forbidden lines can be used to infer a value of t^2 as has been done by Esteban et al. (1998) and Esteban et al. (2004) for the nebula. We apply this to the shock too, adjusting our permitted line analysis to allow for deviations from LTE (Peimbert & Peimbert, 2005). First, we must confirm that the nebular and shock O II permitted lines form following recombination (Grandi, 1976). The shock-to-nebula ratios of the O II and [O III] lines are the same, and much larger than the shock-to-nebula ratios of the [O II] lines. In addition, note that the velocities of the O II lines are consistent with the velocities of [O III] in the nebula (Table 7.1). These two observations both confirm that the O II lines are actually a result of recombinations from O^{++} and not a result of direct starlight excitation of O^+ , validating the use of these lines in the determination of the O^{++}/H^+ ratio. We have used O II recombination line multiplet 1 and [O III] collisionally-excited lines $\lambda\lambda 4363, 4959$ and 5007 with the NEBULAR⁵

⁵The collisionally-excited line results were calculated using the three-zone model in IRAF. In this case only the low- and medium-ionization zones (those of O^0/O^+ and O^{++}) are of interest. The adopted densities of the nebula and shock are $N_e = 6000$ and 10000 , respectively. The temperatures are those determined from the [N II] and [O III] temperature diagnostic lines (refer to § 7.2.2) for the low- and medium-ionization zones, respectively.

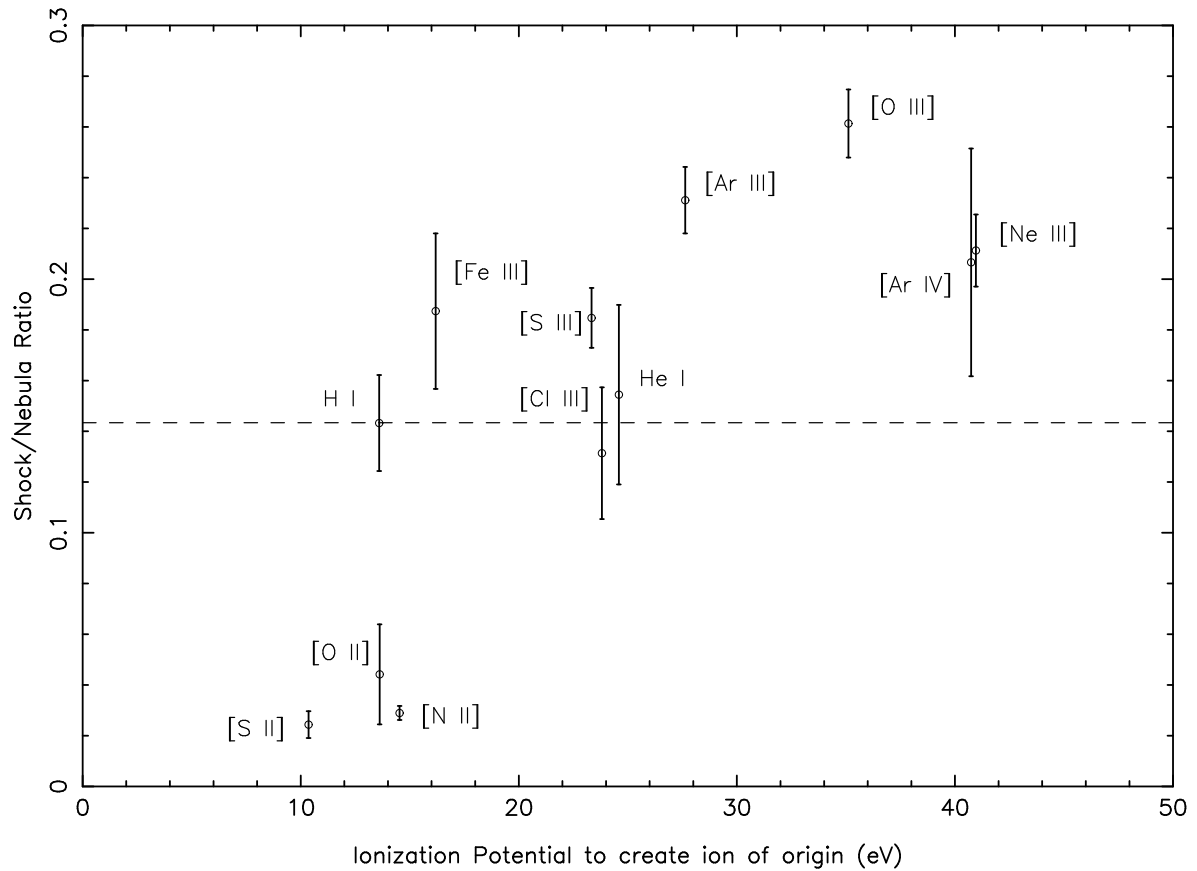


Figure 7.7 Weighted average of shock-to-nebula line ratios (with 1σ error bars) from column (9) of Table 7.1 as a function of the ionization potential needed to create the associated originating ion. The ionization potential serves to differentiate ions with different ionization fractions while the shock-to-nebula ratio is a measure of the optical thickness of the shock to ionizing radiation. If the shock were optically thick, this ratio would be close to one for all lines. H I is presented as a standard for shock/nebula ionization comparison as its originating ion (H^+) has an ionization fraction of roughly one throughout both the shock and the nebula. The ratios of the medium-ionization species ([O III], [Ar III], [Ne III]) all lie above H I as their ionization fractions (averaged through the model) are higher in the shock than in the nebula. Conversely, the ratios of the low-ionization species ([O II], [N II], [S II]) lie below H I.

Table 7.4. O^{++}/H^+ ratios from permitted lines

Transition	Lines (Å)	Nebula			Shock		
		I_{sum}^a ($\times 10^{-2}$)	O^{++}/H^+ ($\times 10^{-5}$) A ^b B ^c		I_{sum}^a ($\times 10^{-2}$)	O^{++}/H^+ ($\times 10^{-5}$) A ^b B ^c	
3s 4P -3p $^4D^0$	4642+76	0.4285 ± 0.0891	27 ± 6	26 ± 6	0.7381 ± 0.1961	47 ± 12	45 ± 12
	4649	0.4355 ± 0.0213	28 ± 1	27 ± 1	1.0491 ± 0.1525	67 ± 10	65 ± 10
	avg	0.4351 ± 0.0250	28 ± 2	27 ± 2	0.9318 ± 0.1689	60 ± 11	57 ± 11

^aDetermined following Peimbert & Peimbert (2005) (their equations 3 and 4) using $N_e(\text{FL})^{neb} \sim 6000$, $N_e(\text{FL})^{shock} \sim 10000 \text{ cm}^{-3}$; $N_e(\text{FL})$ is density determined from forbidden lines (FL).

^bCase A O II recombination coefficients (Storey, 1994)

^cCase B O II recombination coefficients (Storey, 1994)

routines in IRAF (as in Esteban et al., 1998, 2004) to determine t^2 for the nebula and the shock. Not all permitted lines of O II multiplet 1 are observed, so individual (or pairings of) recombination lines are used to predict the complete multiplet’s relative surface brightness (see Table 7.4), following Peimbert & Peimbert (2005; their equations 3 and 4). Using case A and case B O II recombination coefficients from Storey (1994) and case B H I recombination coefficients from Storey & Hummer (1995), O^{++}/H^+ is calculated (see Table 7.4).

The O^{++}/H^+ abundances from recombination and collisionally-excited lines and the inferred t^2 are summarized in Table 7.5 for both the nebula and the shock (along with the O^+/H^+ , O^0/H^+ and total O/H abundances). Our nebular t^2 , 0.009 ± 0.004 , is much lower than what has been deduced from another line of sight (for the same O^{++} ion), $t^2 \sim 0.020 \pm 0.002$ (Esteban et al., 2004) – which did not correct O II lines for deviations from LTE. Despite the presence of detectable O II lines in the shock, the uncertainties are large enough that there is only a 1σ “detection” of t^2 in the shock, $t^2 = 0.010 \pm 0.010$. If the grains are depleted in the shock, a detectable t^2 suggests that the grains may not be the main contributor to t^2 . This will be followed up in § 7.5.2.

7.3 Revisiting [Fe III] energy levels

As there is no velocity gradient in the shock, all shock lines should have the same velocity relative to the H I lines in the nebula. However, a velocity discrepancy associated with the [Fe III] $\lambda 5270$ line appears in Figure 7.6. The most obvious explanation for this is that the ID wavelength for the [Fe III] $\lambda 5270$ is wrong because of an error in the adopted energy of the

Table 7.5. O/H from collisionally excited lines and recombination lines with a derived t^2 parameter

		$12+\log(X^m/H^+)$		
	Feature	CELS ^a	RLs ^{b,c}	t^2
O ⁺⁺	Nebula	8.37 ± 0.01	8.43 ± 0.03	0.009 ± 0.004
	Shock	8.69 ± 0.05	8.76 ± 0.08	0.010 ± 0.010
O ⁺	Nebula	7.78 ± 0.03
	Shock	7.72 ± 0.18
O ⁰	Nebula	6.19 ± 0.03
	Shock
O _{tot}	Nebula	8.47 ± 0.01	8.52 ± 0.03^d	...
	Shock	8.73 ± 0.05	8.80 ± 0.08^d	...

^acollisionally excited lines

^brecombination lines

^cusing case B effective recombination coefficients (Storey, 1994)

^dO⁺⁺ recombination; O⁺, O⁰ collisionally excited lines

upper ${}^3P_2^4$ energy level. The other line originating from the same upper level, [Fe III] $\lambda 5412$, is much weaker and therefore the velocity of the shock component cannot be measured as reliably. However, a constrained Gaussian with a shock velocity that is consistent with that observed in [Fe III] $\lambda 5270$ does appear to fit the data well, albeit with a $S/N \sim 3$ for the shock component. The ${}^3P_2^4$ energy is quoted as $19404.8 \pm 0.5 \text{ cm}^{-1}$ (Sugar & Corliss, 1985). This uncertainty translates to $\pm 0.14 \text{ \AA}$, or $\pm 7.9 \text{ km s}^{-1}$, for both [Fe III] $\lambda 5270.40$ and [Fe III] $\lambda 5411.98$. The red and blue observations were used to constrain the energy of this common upper level, fixing the energies of the lower levels at their NIST values⁶. For these lines to have a velocity consistent with that of the shock (-42.1 km s^{-1}), ${}^3P_2^4$ must be $19404.44 \pm 0.26 \text{ cm}^{-1}$.

This is interesting in the context of the Fe^{++} velocity gradient presented in Baldwin et al. (2000). A velocity gradient of [Fe III] initially observed as a function of wavelength was re-interpreted to be a velocity gradient as a function of the lines' upper level excitation potential above the ground state. The interpretation was presented with scepticism as there was no evidence (or explanation) for velocity gradients associated with any other single ion. The adjustment of the ${}^3P_2^4$ term lowers the nebular velocity of [Fe III] $\lambda 5270$ and [Fe III] $\lambda 5412$ to that of the other [Fe III] lines ($\sim 4 \text{ km s}^{-1}$), removing most of the evidence for a velocity gradient. Note that this nebular velocity is consistent with what is expected from the relationship between velocity and ionization potential (Baldwin et al., 2000).

The only remaining evidence for a sharp velocity gradient in the Fe^{++} zone is from the lines with 3G_4 (24940.9 cm^{-1} ; Sugar & Corliss, 1985) as their common upper level ([Fe III] $\lambda 4008$ and [Fe III] $\lambda 4080$). The same uncertainty ($\pm 0.5 \text{ cm}^{-1}$) exists for this level, translating to uncertainties in the ID wavelengths of [Fe III] $\lambda 4008.35 \pm 0.08$ and [Fe III] $\lambda 4079.70 \pm 0.08$, or equivalently to an uncertainty in the velocity of $\pm 6.1 \text{ km s}^{-1}$. These two lines are too weak to be measured in the shock, but for their line velocities to be consistent with the nebula [Fe III] velocities, 3G_4 would have to be 24941.37 ± 0.23 , $\sim 1\sigma$ above the accepted mean (Sugar & Corliss, 1985).

In summary, if we require the concordance of [Fe III] line velocities in the shock and in the nebula, the ${}^3P_2^4$ energy would be $19404.44 \pm 0.26 \text{ cm}^{-1}$, producing lines with air wavelengths $\lambda 5270.50 \pm 0.07$ and $\lambda 5412.08 \pm 0.07$. The 3G_4 energy would be 24941.37 ± 0.23 producing lines with wavelengths $\lambda 4008.27 \pm 0.04$ and $\lambda 4079.62 \pm 0.04$.

7.4 Models

The HH object has been shown to be photoionized, so we can model the emission using the radiative-collisional equilibrium code, CLOUDY. As the [Fe III] lines figure prominently in our

⁶<http://physics.nist.gov/PhysRefData/ASD/index.html>

discussion, we have improved the description of the Fe^{++} atom in CLOUDY from a 2-level to a 14-level atom, using collision strengths and transition probabilities from Zhang (1996) and Quinet et al. (1996), respectively. This allows all multiplet lines associated with $\lambda 4658$ and $\lambda 5270$ to be included in the determination of Fe abundance. Moreover, as the accuracy of the atomic data for O^+ has been questioned (§ 7.2.2; Esteban et al., 2004) we have replaced the Wiese et al. (1996) transition probabilities with those of Zeippen (1982).

Baldwin et al. (2000) showed that the incident continuum radiation (from the ionizing star, θ^1 Ori C) is best represented by a Mihalas stellar atmosphere model (Mihalas, 1972). However, to test the robustness of our result, we also developed models using a Kurucz stellar atmosphere (Kurucz, 1979). Note that the issues with the Kurucz atmosphere (primarily with its inability to accurately predict the high ionization line $[\text{Ne III}] \lambda 3869$) are not that relevant to our discussion of low- and medium-ionization species.

Since the shock has a small covering factor compared to the nebula, spherical geometry is not assumed and an inner radius is not set. The sound-crossing time for the HH feature ($\sim 10^3$ yr) is roughly the same order as the dynamical timescale of the flow (1500 yr), so instead of assuming a constant pressure (as would be the case in a nebular model), we assume a constant density. Also, as the flow has only been in existence for 1500 yr (5×10^{10} s), it is important to check the validity of a photoionization equilibrium code. The longest timescale from the CLOUDY shock model comes from H recombination: 2×10^8 s – well within the limit of the flow’s age. The incident surface flux of ionizing photons, $\phi(\text{H})$ should be close to the value derived for nebular models ($\log \phi(\text{H}) \sim 13.0$; e.g., Baldwin et al., 1991), as the shock is roughly the same distance from θ^1 Ori C as the nebula (see introduction to this chapter). However, the electron density is probably significantly higher in the shock than in the nebula, as is evident from the observed $\lambda 6731/\lambda 6716$ ratios. Since the shock has been shown to be matter bounded and homogeneous with respect to its ionization structure (§ 7.2.3), the shock model can be developed simply as a finite thickness truncated nebula (i.e., with a pre-defined stopping thickness). This thickness can be predicted from the length ($10''$) and width ($2''$) of the shock in the plane of the sky (from the $[\text{O III}]$ WFPC2 image) and its assumed cylindrically symmetric geometry. Adopting a distance to the nebula of 460 pc (BOM00), the predicted median depth ($3''$) translates to a thickness of 0.007 pc (2×10^{16} cm).

The parameters are varied from these initial values, using observed surface brightness of He I $\lambda 6678$ and line ratios indicating temperature, density and ionization (see Table 7.6) to determine the best-fit models. In the case of an optically thin model, the surface brightness varies as $n_H^2 t$, where n_H is the hydrogen density and t is the model thickness. Adjusting the model thickness does not result in (much of) a change to any of the other constraint ratios, as the ionization fractions of most species are constant through the entire model. Therefore, t is

Table 7.6. Constraints on model parameters for models A and B

Quantity	HH Shock		
	Obs	Mod A ^a	Mod B ^b
F(He I $\lambda 6678$) ^c	0.31 ± 0.01	0.33	0.31
$\lambda 5007/\lambda 6678$ ^d	144.13 ± 8.68	162.62	177.69
$\lambda 5007/\lambda 3726$ ^d	35.35 ± 6.96	40.61	33.76
$\lambda 6312/\lambda 6725$ ^d	1.816 ± 0.270	0.729	1.285
$(\lambda 4959 + \lambda 5007)/\lambda 4363$ ^e	361.02 ± 39.15	492.58	450.55
$(\lambda 6548 + \lambda 6583)/\lambda 5755$ ^e	69.88 ± 17.84	91.29	75.77
$\lambda 6731/\lambda 6716$ ^f	2.01 ± 0.59	2.14	2.14
$\lambda 3726/\lambda 3729$ ^f	2.29 ± 0.69	2.58	2.57
$\lambda 5518/\lambda 5538$ ^f	0.50 ± 0.10	0.45	0.45

^aMihalas stellar atmosphere, CLOUDY H II abundances

^bKurucz stellar atmosphere, Esteban et al. (2004) abundances

^c 10^{-13} ergs cm⁻² s⁻¹ arcsec⁻²

^dIonization indicator

^eTemperature indicator

^fDensity indicator

not completely independent, leaving T_{eff} , $\phi(H)$ and n_H as the three independent parameters.

A series of models were developed, two of which are summarized in Table 7.7: one with a Mihalas stellar atmosphere and CLOUDY Orion abundances (from Baldwin et al., 1991; Rubin et al., 1991; Osterbrock et al., 1992); and one with a Kurucz stellar atmosphere and Esteban et al. (2004) Orion abundances (see Table 7.8). After determining the best-fit parameters for both of these models, the Fe abundance was adjusted to fit the series of [Fe III] lines using the CLOUDY `optimize` routine. Some implications of the derived abundances will be discussed in § 7.5.1.

7.5 Discussion

The echelle observations (from Table 7.1) and the model predictions are summarized in Table 7.9 as I_λ/I_{6678} . If there is no model prediction (i.e., the particulars of the line formation are not

Table 7.7. CLOUDY input parameters

Quantity	Shock Mod A ^a	Shock Mod B ^b
T_{eff} (K)	35200	41200
$\log\phi(\text{H})$	12.700	12.800
radius (pc)	undef	undef
$\log n_{\text{H}}(\text{inner})$ (cm^{-3})	4.20	4.20
Constant	ρ	ρ
Grains	yes	yes
thickness (pc)	0.00396	0.00391

^aMihalas stellar atmosphere, CLOUDY H II abundances

^bKurucz stellar atmosphere, Esteban et al. (2004) abundances

Table 7.8. Model abundances relative to H ($12+\log(X/\text{H})$)

Element, X	Shock Mod A ^a	Shock Mod B ^b
(1)	(2)	(3)
He	10.98	10.98
C	8.48	8.42
N	7.85	7.73
O	8.76	8.76
Ne	7.78	8.05
S	7.00	7.22
Ar	6.48	6.62
Cl	5.00	5.46

^aCLOUDY H II region abundances from Baldwin et al. (1991); Rubin et al. (1991); Osterbrock et al. (1992)

^bEsteban et al. (2004) abundances

included in the model), then the observations are not included in the table.

It is informative to compare the model predictions with the echelle observations for not only the constraint ratios, but all lines predicted by the model. This will further test the robustness of the model. Special note should be taken of lines predicted to be seen in the shock, but not observed. Of such cases, many of them appear around or below the detection limit ($I_\lambda/I_{6678} \sim 0.01$). Many of those lines predicted to be above this limit (He I $\lambda 3705$, [S III] $\lambda 3722$, H I $\lambda 3722$, He I $\lambda 3889$, He I $\lambda 4009$, [S II] $\lambda 4076$, C II $\lambda 4267$, O II $\lambda 4341$, [O II] $\lambda 7320$, [O II] $\lambda 7331$) appear as blended line features in the spectrum and therefore are not included in Table 7.9. There are another three undetected-but-predicted shock lines: O II $\lambda 4093$, O II $\lambda 4111$, O II $\lambda 4277$. Each of these is a complete multiplet prediction requiring a series of multiplet correction factors to predict the observed multiplet component lines. After applying these correction factors to the shock model lines, their predicted flux would lie below the observed detection limit. As discussed in § 7.1, the velocity-shifted [O I] lines are sky lines and not associated with the shock, explaining the disagreement between observation and model at [O I] $\lambda 6300$.

7.5.1 Depletion

The Orion Nebula is thought to have a depleted gas-phase abundance of Fe of roughly a factor of 10 (with respect to solar) due to the presence of grains. From a preliminary analysis, this does not appear to be the case for the shock. The ionization fraction of Fe^{++} remains roughly constant through the slab ($\text{Fe}^{++} \sim 0.2$, Fig. 7.8) with no well-defined Fe^{++} zone, and yet the [Fe III] lines appear quite strong relative to the nebula lines (see Fig. 7.7). This may indicate an “undepletion” of Fe (possibly up to the solar level).

A series of [Fe III] lines ($\lambda\lambda 4658, 5270$, etc.) is predicted using the higher resolution Fe^{++} ion (§ 7.4), and numerous [Fe II] lines are predicted using the 371-level Fe^+ ion. These [Fe II] lines have been shown to have large contributions from continuum pumping (Verner et al., 2000) and therefore cannot be used as indicators of Fe abundance, but the modeled [Fe III] lines scale linearly with the Fe abundance. The iron abundances determined from matching the observed and modeled [Fe III] lines in both shock models appear to be roughly consistent with the nebular gas-phase Fe abundance (see Table 7.10), indicating that the seemingly high shock [Fe III] line strengths can mostly be explained by differences in the models’ parameters, with no need to resort to an order of magnitude change in the abundance. However, if the nebular Fe/H gas-phase abundance is as low as 6.23 (Esteban et al., 2004), the extreme prediction of model B would suggest a three-fold increase in Fe/H gas-phase abundance, indicating a partial destruction of grains in the shock.

Table 7.9. Comparison of model predictions and observations.

Species	ID	HH Shock ^a		
		Obs	Mod A ^b	Mod B ^c
He I	3613.6	0.154 ± 0.041	0.147	0.128
H I	3671.5	0.190 ± 0.035	0.736	0.675
H I	3673.8	0.124 ± 0.028	0.819	0.747
H I	3676.4	0.203 ± 0.032	0.898	0.815
H I	3679.4	0.243 ± 0.028	0.490	0.390
H I	3682.8	0.192 ± 0.032	0.515	0.402
H I	3686.8	0.241 ± 0.036	0.569	0.441
H I	3691.6	0.362 ± 0.046	0.640	0.497
H I	3697.2	0.425 ± 0.077	0.731	0.570
H I	3703.9	0.370 ± 0.051	0.844	0.664
H I	3712.0	0.641 ± 0.139	0.564	0.453
[O II]	3726.0	4.078 ± 0.784	4.005	5.263
[O II]	3728.8	1.780 ± 0.414	1.555	2.046
H I	3734.4	0.568 ± 0.059	0.864	0.712
H I	3750.2	0.632 ± 0.044	1.084	0.911
H I	3770.6	0.937 ± 0.084	1.413	1.202
H I	3797.9	1.143 ± 0.060	1.857	1.604
He I	3819.6	0.236 ± 0.039	0.361	0.365
H I	3835.4	2.140 ± 0.101	2.527	2.225
[Ne III]	3868.8	6.843 ± 0.522	5.524	5.176
H I	3889.0	4.024 ± 0.856^d	3.598	3.216
He I	3964.7	0.231 ± 0.027	0.303	0.273
[Ne III]	3967.5	2.997 ± 0.172	1.665	1.560
H I	3970.1	5.332 ± 0.267	5.350	4.870
He I	4026.2	0.750 ± 0.099	0.667	0.672
[S II]	4068.6	0.118 ± 0.024	0.239	0.274
O II	4075.9	0.029 ± 0.008	0.108	0.108
H I	4101.7	6.621 ± 0.329	8.610	8.005
He I	4120.8	0.082 ± 0.010	0.054	0.056
He I	4143.8	0.059 ± 0.012	0.098	0.099
O II	4153.3	0.037 ± 0.006	0.024	0.024
H I	4340.5	14.460 ± 0.513^d	15.266	14.400
[O III]	4363.2	0.521 ± 0.037	0.440	0.525
He I	4387.9	0.141 ± 0.011	0.177	0.178
He I	4471.5	1.052 ± 0.146	1.415	1.422

Table 7.9—Continued

Species	ID Wavelength	HH Shock ^a		
		Obs	Mod A ^b	Mod B ^c
[Fe III]	4607.0	0.025 ± 0.007	0.015	0.015
O II	4650.8	0.027 ± 0.005	0.176	0.176
[Fe III]	4658.0	0.208 ± 0.024	0.208	0.216
[Fe III]	4667.0	0.007 ± 0.002	0.011	0.011
[Fe III]	4701.5	0.071 ± 0.009	0.086	0.089
He I	4713.1	0.124 ± 0.020	0.180	0.183
[Fe III]	4733.9	0.023 ± 0.004	0.038	0.039
[Ar IV]	4740.2	0.027 ± 0.004	0.091	0.023
[Fe III]	4754.7	0.044 ± 0.007	0.038	0.040
[Fe III]	4769.4	0.040 ± 0.005	0.029	0.030
[Fe III]	4777.7	0.018 ± 0.004	0.018	0.019
H I	4861.3	19.529 ± 0.868	32.202	30.694
[Fe III]	4881.0	0.096 ± 0.014	0.110	0.115
He I	4921.9	0.395 ± 0.028	0.373	0.375
[O III]	4958.9	43.893 ± 3.048	54.013	59.032
[O III]	5006.8	144.127 ± 6.030	162.625	177.685
[Fe III]	5011.3	0.082 ± 0.019	0.040	0.042
He I	5015.7	0.560 ± 0.063	0.759	0.701
He I	5047.7	0.058 ± 0.012	0.051	0.051
[Fe III]	5084.8	0.013 ± 0.003	0.007	0.007
[Fe II]	5158.8	0.016 ± 0.005^e	0.003	0.002
[Fe III]	5270.4	0.121 ± 0.013^e	0.133	0.137
[Fe III]	5270.4	0.121 ± 0.011^f
[Fe III]	5412.0	0.013 ± 0.005^e	0.012	0.012
[Cl III]	5517.7	0.062 ± 0.015^e	0.039	0.133
[Cl III]	5517.7	0.068 ± 0.012^f
[Cl III]	5537.9	0.142 ± 0.009^e	0.086	0.295
[Cl III]	5537.9	0.134 ± 0.009^f
[N II]	5754.6	0.047 ± 0.009^e	0.055	0.023
[N II]	5754.6	0.047 ± 0.009^f
He I	5875.6	3.020 ± 0.242^e	3.779	3.796
He I	5875.6	3.142 ± 0.228^f
[O I]	6300.3	0.053 ± 0.013	0.002	0.002
[S III]	6312.1	0.522 ± 0.029	0.382	0.752
[N II]	6548.0	0.727 ± 0.087	1.278	0.437

Table 7.9—Continued

ID	ID	HH Shock ^a		
		Obs	Mod A ^b	Mod B ^c
Species	Wavelength			
H I	6562.8	71.250 ± 1.222	93.386	89.641
[N II]	6583.5	2.571 ± 0.274	3.771	1.290
He I	6678.2	1.000 ± 0.043	1.000	1.000
[S II]	6716.4	0.096 ± 0.023	0.167	0.187
[S II]	6730.8	0.192 ± 0.032	0.356	0.399
He I	7065.2	1.231 ± 0.124	1.994	2.023
[Ar III]	7135.8	5.397 ± 0.289	4.870	7.963
C II	7231.3	0.024 ± 0.007	0.001	0.001
He I	7281.4	0.178 ± 0.010	0.208	0.207

^aAll fluxes are quoted relative to He I 6678. In the cases where lines were observed in both the red and the blue spectrum, the blue observations are listed first, and the model predictions are not repeated.

^bMihalas stellar atmosphere, CLOUDY H II abundances

^cKurucz stellar atmosphere, Esteban et al. (2004) abundances

^dMeasurement is a blend

^eBlue echelle spectrum

^fRed echelle spectrum

Table 7.10. Iron abundance and depletion in the Orion Nebula and HH shock

Element	Nebula					Shock	
	BFM91 ^a	RDF97 ^b	EPTE98 ^c	EPG04 ^d	CLOUDY ^e	Mod A	Mod B
Gas (Fe/H)	0.042e-4	0.0016e-4	0.026e-4	0.017e-4	0.03e-4	0.034e-4	0.0523e-4
Gas (12+log(Fe/H))	6.62	5.20	6.41	6.23	6.48	6.53	6.72
Depletion ^f (dex)	-0.88	-2.30	-1.08	-1.27	-1.02	-0.97	-0.78

^aBaldwin et al. (1991)

^bRubin et al. (1997), noted to be an anomalously low Fe abundance

^cEsteban et al. (1998)

^dEsteban et al. (2004)

^eCLOUDY H II region abundances from Baldwin et al. (1991), Rubin et al. (1991), and Osterbrock et al. (1992)

^fRelative to solar (7.50, Grevesse & Sauval, 1999)

An analysis of the Fe abundance of Orion B stars (Cunha & Lambert, 1994) and a follow-up analysis of Orion F and G stars (Cunha et al., 1998) imply that the total abundance of Fe is consistent from star to star within the Orion association, but that there may be a slight total Fe depletion with respect to solar (-0.16 dex; Cunha et al., 1998). The Fe depletions obtained from our shock analyses are greater, ranging from -0.8 to -1.0 dex with respect to solar – on the order of the depletions found in the nebula (Baldwin et al., 1991; Rubin et al., 1997; Esteban et al., 1998, 2004). Assuming that the total Orion Fe abundance is on the order of that found from the Orion association stars, the majority of the iron in the shock, as in the nebula, must be locked up in grains.

A number of Si lines are also seen in the shock. Although there is no CLOUDY prediction for these Si lines, the observations can still be analysed using ionization models from CLOUDY and line information from Grandi (1976). The shock-to-nebula ratio is high (~ 0.15) for Si II $\lambda\lambda 3856$, 5056, 6347 (and $\lambda 6371$), but these lines have been shown to form due to starlight excitation (Grandi, 1976) in the Si⁺ gas. The Si⁺ ionization fraction predicted from the CLOUDY models (0.03) is much less than that for Fe⁺⁺ (0.2), but the Si II lines are not linearly dependent on Si abundance, so these lines alone cannot be used to determine Si abundance.

Since $\sim 20\%$ of O atoms are thought to be in dust grains (Esteban et al., 2004), the gas-phase abundance of O can be analysed to determine the extent of dust destruction. The total O/H in

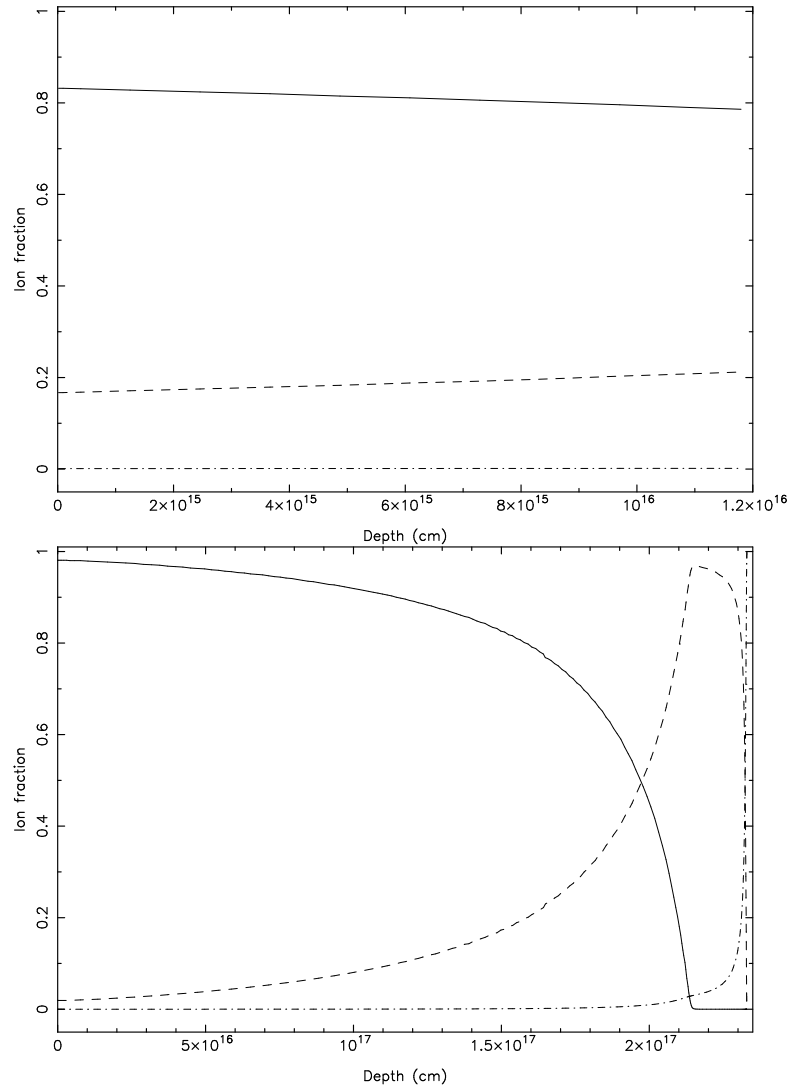


Figure 7.8 Ionization fraction of Fe as a function of depth from the x2shock model (top) and from the nebular model (below) Fe⁺⁺⁺ —; Fe⁺⁺ - - - ; Fe⁺ - · - · - . These structure differences lead to differences between shock-to-nebula ratios for low- and medium-ionization species as shown in Fig 7.7.

the nebula and in the shock is summarized in Table 7.5. Note that O/H for the shock component (8.73 ± 0.05) is an upper limit and the actual value is most likely closer to that of O^{++}/H^+ (8.69 ± 0.05). The shock [O II] and [O III] line profiles across the extracted part of the slit peak at different spatial positions (see Fig. 7.4), indicating that these lines are tracing physically different lines of sight and that a simple addition of O^{++} and O^+ may overestimate the O/H abundance. Our observed nebula O/H abundance (8.48 ± 0.01 or 8.52 ± 0.03 using recombination lines) deviates slightly from other Orion nebula observations, which find $O/H \sim 8.60 - 8.65$ (Baldwin et al., 1991; Rubin et al., 1991; Osterbrock et al., 1992; Esteban et al., 2004). The shock O/H abundance should be compared to an average/typical O/H nebula abundance, as the shock originates in a different region of the nebula. For our observations of the shock, the uncertainty in O/H is large enough that no definitive statement can be made with regards to dust destruction in the shock, except that there may be a small “undepletion” of gas-phase O to parallel the “undepletion” of gas-phase Fe.

Smith et al. (2005) have imaged the bow shocks of HH 529 with T-ReCS at $11.7 \mu\text{m}$, seeing what they refer to as “most likely thermal dust emission” associated with the eastern-most shock. Although supporting the argument of Smith et al. (2005), our evidence for the existence of grains in this one HH object is anomalous when compared with the 21 HH objects studied by Böhm & Matt (2001). For both their high-excitation/fast-moving ($v > 85 \text{ km s}^{-1}$) and low-excitation/slow-moving ($v \leq 50 \text{ km s}^{-1}$) HH objects, the derived Fe depletion is never more than -0.4 dex suggesting that the grains are most likely destroyed in the HH objects regardless of their velocity. It is of interest that for HH 529 – measured to have a velocity of 76 km s^{-1} relative to OMC-1 – the depletion is on the order of that of the nebula (-1.0 dex); there is no evidence for the complete destruction of grains in the eastern-most visible shock of HH 529. This is more along the lines of what one would expect: a slow-moving flow would not be expected to destroy grains, whereas a fast-moving flow would. Böhm & Matt (2001) suggest that the molecular cloud material currently associated with their slow-moving shock may have had its grains destroyed in an earlier pass through a faster-moving shock. Following this argument, the material associated with HH 529 must not have ever passed through a high-excitation/fast-moving shock. This is slightly inconsistent with the set of HH 529 velocities measured by Doi et al. (2002, 2004), many of which suggest the material may have been travelling faster than 85 km s^{-1} . A full Fe abundance analysis of all HH 529 shocks could offer further insight into grain destruction in Herbig-Haro objects.

7.5.2 Temperature fluctuations

The t^2 deduced to exist in the nebula is 0.009 ± 0.004 and in the shock is 0.010 ± 0.010 (§ 7.2.4), which are both within 2σ of zero. Two suggested explanations for the existence of t^2 – large-

scale variations in T_e or the presence of shielded or heated regions – cannot apply for the small column covered by the shock. However, since the grains still appear to be present in the shock a t^2 detection suggests a third explanation: that the grains may be the main contributor to t^2 . Conversely, an “effective” t^2 may be introduced if the effective recombination coefficients, collision strengths, and/or transition probabilities are inaccurate or if there were some other contributions to the line emission besides solely recombination or collisional excitation.

7.6 Conclusions

High-resolution spectroscopy of the Orion Nebula across the Herbig-Haro object HH 529 has allowed for a comparison of that local part of the nebula with the velocity-shifted spectrum of the flow. The radial velocity (as measured from the H I emission lines), $-42.1 \pm 1.2 \text{ km s}^{-1}$ is consistent with the -40 to -42 km s^{-1} range as measured by Doi et al. (2004) for a slightly different line of sight. In addition, there is ample evidence to suggest that this flow has been photoionized. Herbig-Haro objects usually have a strong low-ionization line spectrum. In this case, the fact that we see strong medium-ionization lines and much weaker low-ionization lines indicates that we have a photoionized shock, as first suggested by O’Dell et al. (1997a). The distinguishing shock-to-nebula ratios as a function of ionization fraction, or ionizing potential as in Figure 7.7, further support this hypothesis, leading us to model the shock as a matter-bounded photoionization region.

The shock component was modeled using the photoionization equilibrium code, CLOUDY. Both Mihalas and Kurucz stellar atmosphere models were investigated to ensure the robustness of our conclusions. A series of “best-fit” models covering a range of stellar temperatures, densities, and $\phi(\text{H})$ fluxes has allowed us to determine that the depletion of Fe (relative to solar) in the nebula also exists in the shock. The higher density of the photoionized shock allows for the formation of relatively strong [Fe III] lines without necessitating a reduction of the Fe depletion. The Fe depletion for the shock is roughly the same as for the Orion Nebula, an order of magnitude relative to solar (-1.0 dex). The total Fe abundance of the Orion association stars may be slightly depleted (-0.16 dex; Cunha et al., 1998), but not to the extent of the gas-phase Fe in the nebula and shock. This suggests that if the total Fe abundance in the nebula and shock is of the same order as that found from the Orion association stars, grains must be present in the Herbig-Haro flow to account for the depletion of gas-phase Fe. Böhm & Matt (2001) suggests that grains are destroyed in many HH objects as the material passes through high-excitation/fast-moving shocks. From our results, we infer that the eastern-most shock of HH 529 never reached the velocities necessary to destroy the majority of the grains despite the presence of fast-moving shocks elsewhere in HH 529. This supports the observations of $11.7 \mu\text{m}$

thermal dust emission in the eastern-most shock of HH 529 (Smith et al., 2005). Further information about grain destruction in HH 529 can be obtained from parallel Fe abundance analyses for the remainder of the HH 529 photoionized shocks.

Temperature fluctuations in the Orion Nebula have been used to explain discrepancies in abundances found from recombination lines versus abundances found from collisionally-excited lines. Using solely lines originating from the O^{++} gas, we derive t^2 for the nebula ($t^2 = 0.009 \pm 0.004$) and the shock ($t^2 = 0.010 \pm 0.010$). Esteban et al. (2004) have published a series of t^2 for a number of ions, including O^{++} (0.020 ± 0.002), as well as an average from their series of ions (0.022 ± 0.002). The interesting result is that the shock maintains a t^2 similar to the nebula (albeit with a large uncertainty), despite being much thinner. These observations, if corroborated with higher S/N data, may draw into question some of the theories that have been expounded surrounding an explanation for these inferred t^2 fluctuations. Grains appear to be present in the shock, suggesting that the grains may still somehow be contributing to t^2 . The measurement of a non-zero t^2 in a matter-bounded shock would more likely support the argument for an effective t^2 resulting from uncertainties in the atomic data and/or missing contributions to the line emission. Higher S/N O II spectra of the shock will reduce the uncertainty of the inferred t^2 and allow for more definitive conclusions to be made.

Chapter 8

Summary and future directions

Using both deep optical echelle spectra and HST long-slit spectra, we have analysed much about the Orion Nebula. The ground-based observations are of high enough resolution that we are able to determine such quantities as the velocities of the lines as well as the temperature and density from diagnostic lines.

These echelle spectra offer lines in the hundreds from which we can obtain information about the nature of the nebula and its components – including here the Herbig-Haro object HH 529. We have been able not only to distinguish these high-velocity ($-42.1 \pm 1.2 \text{ km s}^{-1}$ relative to H I) lines from the background nebular lines, but have also been able to decipher key information about the dust content of the Herbig-Haro object, by first showing that it is a photoionized object and modeling it as such. The strong medium-ionization lines and relatively weak low-ionization lines suggest that the eastern-most shock of HH 529 is photoionized. This is supported by the series of shock-to-nebula emission line ratios which indicate that the HH object is indeed matter-bounded (as compared to the radiation-bounded nebula in the background). From CLOUDY photoionization models of this eastern-most shock of HH 529, we find that the Fe depletion is consistent with that in the nebula. Smith et al. (2005) detect $11.7 \mu\text{m}$ emission – which they associate with thermal dust emission – associated with this same shock, supporting the argument that there is still dust present in the eastern-most shock. This complementary evidence suggests that this HH 529 shock has never reached the velocities necessary to destroy the majority of the grains despite the presence of higher velocity shocks elsewhere in HH 529 (Doi et al., 2002, 2004). A full Fe abundance analysis of all of the shocks associated with HH 529 could offer further insight into grain destruction in Herbig-Haro objects.

Variations in temperature within the nebula have been used to explain the different abundances calculated from permitted versus forbidden lines – despite there not being a reasonable theory for their existence. The inferred temperature fluctuations, t^2 , are along the line of sight sampled in the spectrum. With the long-slit spatial coverage across the nebula, we are able to

investigate the existence of these temperature fluctuations, albeit only t_A^2 in the plane of the sky since this analysis depends on emission integrated along the line of sight at different slit positions. Taking into account the uncertainty of the measurements, we have determined that a non-zero temperature fluctuation does exist over the $52''$ (~ 0.11 pc) of the various slits, with a weighted average $t_A^2 = 0.0076 \pm 0.0004$. However, the magnitude of this temperature fluctuation is not as large as that inferred from the comparison between permitted and forbidden line abundance calculations (e.g., $t^2 \sim 0.024$ Esteban et al., 1998). Since the temperature fluctuations are thought to exist along the line of sight, it is not surprising that this temperature fluctuation in the plane of the sky is so small. Its measured non-zero value though does put a lower limit on the temperature fluctuation in three dimensions. Additionally, line of sight temperature fluctuations have been deduced from the ground-based echelle spectra of the background nebula ($t^2 \sim 0.009 \pm 0.004$) and the foreground HH object ($t^2 \sim 0.010 \pm 0.010$). The shock has a t^2 similar to that of the nebula, despite being much thinner. These observations, if corroborated with higher signal-to-noise data, could draw into question the true nature of these temperature fluctuations. It would be interesting if an “effective” t^2 resulting from uncertainties in the atomic data and/or missing contributions to the line emission could explain the difference in calculated abundances when using forbidden as compared to permitted lines.

The high resolution of the spectra has enabled us to determine not only velocities of the observed lines, but in a couple of cases has allowed us to use these velocities to predict more accurate ID line wavelengths. This can be done as it is expected that lines originating from the same ionized species (and especially a common upper level) will have the same measured line velocity. The lines whose energy levels (and wavelengths) are investigated here are those of [O II] and [Fe III]. Planetary nebulae data were required to set the lower energy level of the [O II] ground configuration, but the remainder of the levels were set using the series of Orion Nebula spectra (1SW, x2, 37W), assuming each of these three lines-of-sight has a unique [O II] line velocity. The primary adjustment required to the energy levels is that of $E_{2D_{5/2}-2D_{3/2}} = 19.80 \pm 0.01 \text{ cm}^{-1}$ (was 20.02 cm^{-1} , Martin et al., 1993).

In the case of [Fe III], the energy levels were set by requiring that the [Fe III] velocity-shifted HH object lines had the same velocity as the rest of the HH lines. Baldwin et al. (2000) had observed a [Fe III] velocity gradient in the nebula as a function of excitation potential of the line’s upper level. However, there is no possibility of a velocity/ionization gradient in the thin photoionized shock and so all lines are expected to have the same velocity. Upon adjusting the appropriate energy levels of [Fe III] in order to yield a uniform HH velocity, the unexplained [Fe III] nebular velocity gradient was eliminated – found to be an artifact of incorrect ID wavelengths.

Much of this analysis would not have been possible without a robust calculation of the

extinction in the nebula. To this end, we have developed a novel method of determining the extinction corrections across the spectrum from the UV through the near-IR. We have shown that the wavelength dependence of the nebular extinction curve is well represented by that of the stellar extinction, and we have defined a method to determine the amplitude of the extinction curve using lines whose relative intensities can be predicted, like recombination lines of H I and He I and/or a common upper level line pair, like that of [O II]. The metastability of one of the energy levels of He I has required an additional calculation of the effects of self-absorption (using CLOUDY) to determine deviations from strict case B recombination predictions for a series of He I UV lines. The UV lines are then useful for validating the extinction correction in the ultraviolet. We are able to calculate a consistent extinction correction across the entire UV through near-IR spectrum. One interesting quantitative application was to the many other He I lines that deviate from case B, yet can be accurately predicted by CLOUDY.

Although the spectra have thus far been analysed in great depth, there still remain interesting issues that can be addressed. For example, the line velocities of the echelle spectra's forbidden and permitted lines are being analysed to determine the dominant line formation processes involved. Because the nebular gas is accelerating away from the background cloud, the resultant velocity gradient can be coupled with the ionization gradient (from forbidden lines) to determine the ionization stage from which the permitted lines originate. This allows us to determine whether a permitted line is forming primarily as a result of recombination or as a result of direct starlight continuum pumping (one ionization stage lower). This information is essential when considering determining abundances from permitted lines. Certainly, given accurate recombination data, abundances can be determined from recombination lines. However, permitted lines forming due to direct starlight excitation cannot as simply be converted to abundances because of unknown pumping efficiencies. Some preliminary work on this has already been discussed, and published, in Chapter 7 with respect to the O II permitted (and recombination) lines used in the determination of the inferred t^2 .

Additionally, we are working on a complete abundance analysis of the STIS spectra, which offer a spatially co-incident and well-calibrated UV through near-IR set of spectral lines thanks to the ground work laid within this thesis (namely in Chapters 3 and 4). This work will complement the Orion Nebula abundance analyses of Baldwin et al. (1991), Rubin et al. (1997), Esteban et al. (1998) and Esteban et al. (2004). Our approach will be to determine a robust CLOUDY model that will accurately reproduce the STIS long-slit spectra results. This has the added benefit of revealing the underlying physical conditions which give rise to the observed spectrum.

Many of the limitations involved in analysis of the Orion Nebula (and nebulae in general) lie not in the spectral resolution or signal-to-noise of the spectra, but in the uncertainties of the

atomic data and the models. Consequently, deeper observations will not necessarily permit a more accurate view of the nebula (i.e., its temperature, density, and abundances). Exceptions however do exist. For example, as mentioned in Chapter 7, in order to understand better the link between HH objects and Fe depletion and/or temperature fluctuations, higher signal-to-noise HH spectra are required.

Bibliography

- Abel, N. P., Brogan, C. L., Ferland, G. J., O'Dell, C. R., Shaw, G., & Troland, T. H. 2004, ApJ, 609, 247
- Allende Prieto, C., Lambert, D. L., & Asplund, M. 2001, ApJ, 556, L63
- Aller, L. H. & Hyung, S. 1995, MNRAS, 276, 1101
- Aller, L. H., Hyung, S., & Feibelman, W. A. 1996, PASP, 108, 488
- Böhm, K. & Matt, S. 2001, PASP, 113, 158
- Baker, J. G. & Menzel, D. H. 1938, ApJ, 88, 52
- Baldwin, J. A., Crotts, A., Dufour, R. J., Ferland, G. J., Heathcote, S., Hester, J. J., Korista, K. T., Martin, P. G., O'Dell, C. R., Rubin, R. H., Tielens, A. G. G. M., Verner, D. A., Verner, E. M., Walter, D. K., & Wen, Z. 1996, ApJ, 468, L115
- Baldwin, J. A., Ferland, G. J., Martin, P. G., Corbin, M. R., Cota, S. A., Peterson, B. M., & Slettebak, A. 1991, ApJ, 374, 580
- Baldwin, J. A., Verner, E. M., Verner, D. A., Ferland, G. J., Martin, P. G., Korista, K. T., & Rubin, R. H. 2000, ApJS, 129, 229 (BVV00)
- Balick, B., Gammon, R. H., & Hjellming, R. M. 1974, PASP, 86, 616
- Bally, J., O'Dell, C. R., & McCaughrean, M. J. 2000, AJ, 119, 2919 (BOM00)
- Beck-Winchatz, B., Böhm, K., & Noriega-Crespo, A. 1996, AJ, 111, 346
- Benjamin, R. A., Skillman, E. D., & Smits, D. P. 1999, ApJ, 514, 307
- Bhatia, A. K. & Kastner, S. O. 1995, ApJS, 96, 325
- Blagrove, K. P. M. & Martin, P. G. 2004, ApJ, 610, 813
- Blagrove, K. P. M., Martin, P. G., & Baldwin, J. A. 2006a, ApJ, 644, 1006

- Blagrove, K. P. M., Martin, P. G., Rubin, R. H., & Baldwin, J. A. 2006b, in preparation
- Blagrove, K. P. M., Martin, P. G., Rubin, R. H., Dufour, R. J., Baldwin, J. A., Hester, J. J., & Walter, D. K. 2006c, *ApJ*, in press
- Bohlin, R., Collins, N., & Gonnella, A. 1998, Instrument Science Report, STIS 97-14 (Baltimore: STScI)
- Bohlin, R. & Hartig, G. 1998, Instrument Science Report, STIS 98-20 (Baltimore: STScI)
- Bohlin, R. C. & Savage, B. D. 1981, *ApJ*, 249, 109 (BS81)
- Bowen, I. S. 1955, *ApJ*, 121, 306
- . 1960, *ApJ*, 132, 1
- Bowers, C. & Baum, S. 1998, Instrument Science Report, STIS 98-23 (Baltimore: STScI)
- Burke, V. M., Lennon, D. J., & Seaton, M. J. 1989, *MNRAS*, 236, 353
- Cardelli, J. A. & Clayton, G. C. 1988, *AJ*, 95, 516 (CC88)
- Cardelli, J. A., Clayton, G. C., & Mathis, J. S. 1989, *ApJ*, 345, 245 (CCM89)
- Costero, R. & Peimbert, M. 1970, *Boletín de los Observatorios Tonantzintla y Tacubaya*, 5, 229 (CP70)
- Cunha, K. & Lambert, D. L. 1994, *ApJ*, 426, 170
- Cunha, K., Smith, V. V., & Lambert, D. L. 1998, *ApJ*, 493, 195
- de Robertis, M. M., Osterbrock, D. E., & McKee, C. F. 1985, *ApJ*, 293, 459
- Doi, T., O'Dell, C. R., & Hartigan, P. 2002, *AJ*, 124, 445
- . 2004, *AJ*, 127, 3456
- Dopita, M. A., Evans, I., & Schwartz, R. D. 1982, *ApJ*, 263, L73
- Eriksson, K. B. S. 1987, *J. Opt. Soc. Am. B*, 4, 1369
- Esteban, C., Peimbert, M., García-Rojas, J., Ruiz, M. T., Peimbert, A., & Rodríguez, M. 2004, *MNRAS*, 355, 229 (EPG04)
- Esteban, C., Peimbert, M., Torres-Peimbert, S., & Escalante, V. 1998, *MNRAS*, 295, 401 (EPTE98)

- Feibelman, W. A., Hyung, S., & Aller, L. H. 1994, *ApJ*, 426, 653
- . 1996, *MNRAS*, 278, 625
- Feigelson, E. D., Broos, P., Gaffney, J. A., Garmire, G., Hillenbrand, L. A., Pravdo, S. H., Townsley, L., & Tsuboi, Y. 2002, *ApJ*, 574, 258
- Ferland, G. J. 2001, *PASP*, 113, 41
- Ferland, G. J., Korista, K. T., Verner, D. A., Ferguson, J. W., Kingdon, J. B., & Verner, E. M. 1998, *PASP*, 110, 761
- Froese Fischer, C. & Saha, H. P. 1985, *Phys. Scr*, 32, 181
- Goudis, C. 1982, *The Orion Complex: A Case Study of Interstellar Matter* (Dordrecht, Netherlands: D. Reidel Publishing Co. (Astrophysics and Space Science Library. Volume 90))
- Grandi, S. A. 1976, *ApJ*, 206, 658
- Grevesse, N. & Sauval, A. J. 1999, *A&A*, 347, 348
- Haro, G. 1952, *ApJ*, 115, 572
- Harrington, J. P., Seaton, M. J., Adams, S., & Lutz, J. H. 1982, *MNRAS*, 199, 517
- Henney, W. J. 1998, *ApJ*, 503, 760
- Herbig, G. H. 1950, *ApJ*, 111, 11
- Hillenbrand, L. A. & Carpenter, J. M. 2000, *ApJ*, 540, 236
- Hyung, S. 1994, *ApJS*, 90, 119
- Hyung, S. & Aller, L. H. 1995a, *MNRAS*, 273, 973
- . 1996, *MNRAS*, 278, 551
- . 1997a, *MNRAS*, 292, 71
- . 1997b, *ApJ*, 491, 242
- . 1998, *PASP*, 110, 466
- Hyung, S., Aller, L. H., & Feibelman, W. A. 1993, *PASP*, 105, 1279
- . 1994a, *PASP*, 106, 745
- . 1994b, *MNRAS*, 269, 975

- . 1994c, *ApJS*, 93, 465
- . 1997, *ApJS*, 108, 503
- . 1999a, *ApJ*, 525, 294
- . 1999b, *ApJ*, 514, 878
- Hyung, S., Aller, L. H., Feibelman, W. A., & Lee, S. 2001a, *ApJ*, 563, 889
- Hyung, S., Aller, L. H., Feibelman, W. A., & Lee, W. 2001b, *AJ*, 122, 954
- Hyung, S., Aller, L. H., Feibelman, W. A., Lee, W. B., & de Koter, A. 2000, *MNRAS*, 318, 77
- Hyung, S., Aller, L. H., & Lee, W. 2001c, *PASP*, 113, 1559
- Hyung, S. & Aller, L. H. H. 1995b, *MNRAS*, 273, 958
- Hyung, S., Keyes, C. D., & Aller, L. H. 1995, *MNRAS*, 272, 49
- Kaufman, V. & Sugar, J. 1986, *Journal of Physical and Chemical Reference Data*, 15, 321
- Keenan, F. P., Aller, L. H., Ryans, R. S. I., & Hyung, S. 2001, *Proceedings of the National Academy of Science*, 98, 9476
- Keenan, F. P., Hibbert, A., Ojha, P. C., & Conlon, E. S. 1993, *Phys. Scr*, 48, 129
- Kim, S., Martin, P. G., & Hendry, P. D. 1994, *ApJ*, 422, 164
- Kingdon, J. B. & Ferland, G. J. 1998, *ApJ*, 506, 323
- Kurucz, R. L. 1979, *ApJS*, 40, 1
- Kwitter, K. B. & Henry, R. B. C. 1998, *ApJ*, 493, 247
- Lennon, D. J. & Burke, V. M. 1994, *A&AS*, 103, 273
- Liu, X.-W. 2003, in *IAU Symposium*, 339—+
- Liu, X.-W., Luo, S.-G., Barlow, M. J., Danziger, I. J., & Storey, P. J. 2001, *MNRAS*, 327, 141
- Liu, X.-W., Storey, P. J., Barlow, M. J., & Clegg, R. E. S. 1995, *MNRAS*, 272, 369
- Liu, X.-W., Storey, P. J., Barlow, M. J., Danziger, I. J., Cohen, M., & Bryce, M. 2000, *MNRAS*, 312, 585
- Luo, S.-G., Liu, X.-W., & Barlow, M. J. 2001, *MNRAS*, 326, 1049

- Martin, P. G., Rubin, R. H., Ferland, G. J., Dufour, R. J., O'Dell, C. R., Baldwin, J. A., Hester, J. J., & Walter, D. K. 1996, *Bulletin of the American Astronomical Society*, 28, 1416
- Martin, P. G. & Whittet, D. C. B. 1990, *ApJ*, 357, 113
- Martin, W. C., Kaufman, V., & Musgrove, A. 1993, *J. Phys. Chem. Ref. Data*, 22, 1179
- McLaughlin, B. M. & Bell, K. L. 1993, *ApJ*, 408, 753
- Mendoza, C. & Zeippen, C. J. 1982, *MNRAS*, 198, 127
- Mihalas, D. 1972, *Non-LTE Model Atmospheres for B & O Stars*, Tech. Rep. NCAR-TN/STR-76, National Center for Atmospheric Research, Boulder, Colorado
- O'Dell, C. R. 2001a, *PASP*, 113, 29
- . 2001b, *ARA&A*, 39, 99
- O'Dell, C. R. & Doi, T. 1999, *PASP*, 111, 1316
- . 2003, *AJ*, 125, 277
- O'Dell, C. R., Hartigan, P., Bally, J., & Morse, J. A. 1997a, *AJ*, 114, 2016
- O'Dell, C. R., Hartigan, P., Lane, W. M., Wong, S. K., Burton, M. G., Raymond, J., & Axon, D. J. 1997b, *AJ*, 114, 730
- O'Dell, C. R., Peimbert, M., & Peimbert, A. 2003, *AJ*, 125, 2590
- O'Dell, C. R. & Wen, Z. 1994, *ApJ*, 436, 194
- O'Dell, C. R. & Wong, K. 1996, *AJ*, 111, 846
- Osterbrock, D. E. 1989, *Astrophysics of Gaseous Nebulae and Active Galactic Nuclei* (Mill Valley, CA: University Science Books)
- Osterbrock, D. E., Tran, H. D., & Veilleux, S. 1992, *ApJ*, 389, 305 (OTV92)
- Péquignot, D., Amara, M., Liu, X.-W., Barlow, M. J., Storey, P. J., Morisset, C., Torres-Peimbert, S., & Peimbert, M. 2002, in *Revista Mexicana de Astronomia y Astrofisica Conference Series*, 142–143
- Peimbert, A. & Peimbert, M. 2005, in *Revista Mexicana de Astronomia y Astrofisica Conference Series*, 9–14
- Peimbert, M. 1967, *ApJ*, 150, 825

- Peimbert, M. & Costero, R. 1969, *Boletin de los Observatorios Tonantzintla y Tacubaya*, 5, 3
- Peimbert, M. & Torres-Peimbert, S. 1977, *MNRAS*, 179, 217
- Pogge, R. W., Owen, J. M., & Atwood, B. 1992, *ApJ*, 399, 147
- Porter, R. L., Bauman, R. P., Ferland, G. J., & MacAdam, K. B. 2005, *ApJ*, 622, L73
- Porter, R. L., Ferland, G. J., & MacAdam, K. B. 2006, *ApJ*, submitted
- Pottasch, S. R., Hyung, S., Aller, L. H., Beintema, D. A., Bernard-Salas, J., Feibelman, W. A., & Klöckner, H.-R. 2003, *A&A*, 401, 205
- Pradhan, A. K. 1976, *MNRAS*, 177, 31
- Pradhan, A. K., Montenegro, M., Nahar, S. N., & Eissner, W. 2006, *MNRAS*, 366, L6
- Quinet, P., Le Dourneuf, M., & Zeippen, C. J. 1996, *A&AS*, 120, 361
- Ramsbottom, C. A., Bell, K. L., & Keenan, F. P. 1999, *MNRAS*, 307, 669
- Ramsbottom, C. A., Bell, K. L., & Stafford, R. P. 1996, *Atomic Data and Nuclear Data Tables*, 63, 57
- Reipurth, B. & Bally, J. 2001, *ARA&A*, 39, 403
- Robbins, R. R. 1968, *ApJ*, 151, 511
- Rubin, R. H. 1969, *ApJ*, 155, 841
- . 1986, *ApJ*, 309, 334
- Rubin, R. H., Bhatt, N. J., Dufour, R. J., Buckalew, B. A., Barlow, M. J., Liu, X.-W., Storey, P. J., Balick, B., Ferland, G. J., Harrington, J. P., & Martin, P. G. 2002, *MNRAS*, 334, 777
- Rubin, R. H., Dufour, R. J., Ferland, G. J., Martin, P. G., O'Dell, C. R., Baldwin, J. A., Hester, J. J., Walter, D. K., & Wen, Z. 1997, *ApJ*, 474, L131
- Rubin, R. H., Dufour, R. J., & Walter, D. K. 1993, *ApJ*, 413, 242
- Rubin, R. H., Martin, P. G., Dufour, R. J., Ferland, G. J., Baldwin, J. A., Hester, J. J., & Walter, D. K. 1998, *ApJ*, 495, 891
- Rubin, R. H., Martin, P. G., Dufour, R. J., Ferland, G. J., Blagrove, K. P. M., Liu, X.-W., Nguyen, J. F., & Baldwin, J. A. 2003, *MNRAS*, 340, 362

- Rubin, R. H., Simpson, J. P., Haas, M. R., & Erickson, E. F. 1991, *ApJ*, 374, 564
- Savage, B. D. & Mathis, J. S. 1979, *ARA&A*, 17, 73
- Schraml, J. & Mezger, P. G. 1969, *ApJ*, 156, 269
- Seaton, M. J. 1960, *Reports of Progress in Physics*, 23, 313
- Sharpee, B., Williams, R., Baldwin, J. A., & van Hoof, P. A. M. 2003, *ApJS*, 149, 157
- Sharpee, B. D., Slanger, T. G., Huestis, D. L., & Cosby, P. C. 2004, *ApJ*, 606, 605
- Sharpless, S. 1952, *ApJ*, 116, 251
- Smith, N., Bally, J., Shuping, R. Y., Morris, M., & Hayward, T. L. 2004, *ApJ*, 610, L117
- Smith, N., Bally, J., Shuping, R. Y., Morris, M., & Kassis, M. 2005, *AJ*, 130, 1763
- Smits, D. P. 1996, *MNRAS*, 278, 683
- Stafford, R. P., Bell, K. L., Hibbert, A., & Wijesundera, W. P. 1994, *MNRAS*, 268, 816
- Storey, P. J. 1994, *A&A*, 282, 999
- Storey, P. J. & Hummer, D. G. 1995, *MNRAS*, 272, 41
- Sugar, J. & Corliss, C. 1985, *Atomic Energy Levels of the Iron-Period Elements: Potassium through Nickel* (Washington, DC: American Chemical Society)
- Tenorio-Tagle, G. 1979, *A&A*, 71, 59
- Tsamis, Y. G., Barlow, M. J., Liu, X.-W., Danziger, I. J., & Storey, P. J. 2003, *MNRAS*, 338, 687
- Verner, E. M., Verner, D. A., Baldwin, J. A., Ferland, G. J., & Martin, P. G. 2000, *ApJ*, 543, 831
- Viegas, S. M. & Clegg, R. E. S. 1994, *MNRAS*, 271, 993
- Vogt, S. S. 1987, *PASP*, 99, 1214
- Walsh, J. R. 1998, *ST-ECF Newsletter*
- Walter, D. K. 1993, *Ph.D. Thesis*
- Wang, W., Liu, X.-W., Zhang, Y., & Barlow, M. J. 2004, *A&A*, 427, 873
- Wen, Z. & O'Dell, C. R. 1995, *ApJ*, 438, 784

Wiese, W. L., Fuhr, J. R., & Deters, T. M. 1996, Atomic Transition Probabilities of Carbon, Nitrogen, and Oxygen: A Critical Data Compilation (Washington, DC: American Chemical Society)

Zapata, L. A., Rodríguez, L. F., Kurtz, S. E., O'Dell, C. R., & Ho, P. T. P. 2004, *ApJ*, 610, L121

Zeippen, C. J. 1982, *MNRAS*, 198, 111

—. 1987, *A&A*, 173, 410

Zhang, H. 1996, *A&AS*, 119, 523

Zuckerman, B. 1973, *ApJ*, 183, 863

Appendix A

CLOUDY contributions

In the creation of this thesis, much code was independently developed while others' codes were debugged. Here, I will highlight the few contributions I have made to the photoionization equilibrium code, CLOUDY in the process of investigating nebular models.

1. [O II] statistical weights were reversed. In the process of analysing the [O II] density diagnostic lines, we investigated using different sets of atomic data – transition probabilities and collision strengths. In so doing, I came upon an inadvertent inversion of statistical weights. This inversion was adversely affecting, albeit minimally, the calculation of level populations and line strengths.

2. Recombination contribution to [N II] 5755 line was too large. While investigating the [N II] temperature diagnostic lines, I noticed that the recombination contribution to the [N II] 5755 forbidden line was inexplicably high. On further investigation, I was able to attribute this to a missing factor of $(10^4)^{0.3}$ in the code.

3. Energy levels in wavenumbers instead of in Kelvin. While developing code for the Fe^{++} atom (see number 4 below), I discovered that some energy levels were input as wavenumbers, but were interpreted as being in Kelvin (a difference of a factor of 1.439; i.e., hc/k). This affected the calculation of line wavelengths and the calculation of level populations.

4. Updated Fe^{++} atom from 3-level atom to 14-level atom. We observed a number of [Fe III] lines in our echelle spectra, only two of which were predicted by CLOUDY. By upgrading the code from a 3-level to a 14-level atom, I was able to resolve the complete series of observed optical lines. Additionally, this higher resolution atom resolves IR lines such as 22.93 μm , 33.04 μm which are now being observed using Spitzer.